Final Technical Report (FTR)

***a.** Federal Agency*	Department of Energy	
***b.** Award Number*	DE-EE0008221	
***c.** Project Title*	Design and Manufacturing of High Performance, Reduced Charge Heat Exchangers	
***d.** Recipient Organization*	University of Maryland, College Park	
***e.** Project Period*	*Start*: February 01, 2018	*End*: September 30, 2023
***f.** Principal Investigator (PI)*	Reinhard Radermacher Professor raderm@umd.edu 301-405-5286	
***g.** Business Contact (BC)*	Cassie Moore Senior Contract Administrator cmoore17@umd.edu 301-405-6269	
***h.** Certifying Official (if different from the PI or BC)*	N/A	

Signature of Certifying Official *Date*

By signing this report, I certify to the best of my knowledge and belief that the report is true, complete, and accurate. I am aware that any false, fictitious, or fraudulent information, misrepresentations, half-truths, or the omission of any material fact, may subject me to criminal, civil or administrative penalties for fraud, false statements, false claims or otherwise. (U.S. Code Title 18, Section 1001, Section 287 and Title 31, Sections 3729-3730). I further understand and agree that the information contained in this report are material to Federal agency's funding decisions and I have any ongoing responsibility to promptly update the report within the time frames stated in the terms and conditions of the above referenced Award, to ensure that my responses remain accurate and complete.

Acknowledgement

"This material is based upon work supported by the U.S. Department of Energy's Office of Energy Efficiency and Renewable Energy (EERE) Building Technologies Office (BTO) under the DE-FOA-0001632, BENEFIT 2017 Award Number DE-EE0008221."

Disclaimer

Executive Summary

Air-to-fluid heat exchangers (HXs) play a critical role as the main heat transfer component in Heating, Ventilation, Air-Conditioning, and Refrigeration (HVAC&R) systems. However, their airside thermal resistance significantly inhibits their overall performance. Furthermore, these HXs must be continually more compact to meet the latest refrigerant charge limits to reduce emissions. Recent literature suggests that traditional HX geometries (e.g., round or flat tubes with fins), have reached their limits, and more sophisticated shape- and topology-optimized designs are required to achieve the next jump in performance.

This research sheds light on the next generation of air-to-refrigerant HXs and aims to address several practical issues to commercialization such as novelty challenges (improved performance for significant charge reduction; modeling expertise & time investment), manufacturing challenges (non-round tube manufacturing; tube-header integration; product qualification, e.g., burst pressure testing, extreme operational environment, etc.), and operational challenges (flow maldistribution, fouling & wetting, noise & vibration). For example, a >20% improvement on one (or more) HX-level performance metrics (e.g., envelope volume, airside pressure drop, face area, capacity, refrigerant charge, weight, cost, etc.) must be achieved before a HX design is considered for commercialization.

We present a new, comprehensive and experimentally validated air-to-refrigerant HX optimization framework with simultaneous thermal-hydraulic performance and mechanical strength considerations for novel, non-round, shape- and topology-optimized tubes capable of optimizing single and two-phase HX designs for any refrigerant choice and performance requirement with significant engineering time savings compared to conventional design practices. The framework was exercised for a wide range of applications and refrigerants, resulting in HXs which achieved greater than 20% improved performance, 20% reductions in size, and 25% reductions in refrigerant charge.

To enable non-round tube bundle use in next generation HVAC&R equipment, novel manufacturing techniques were investigated, including the development of conventional manufacturing methods for small diameter, non-round tubes and novel tube-header integration strategies. In total, ten HX prototypes were manufactured, nine using conventional methods directly attributed to this project and one using advanced additive manufacturing methods. The five-year manufacturing feasibility of the proposed HXs was found to have a good outlook.

The non-round tube HX simulated performance was validated through comprehensive experimental testing, including nine in-house component-level tests, one independent component-level test at an industry partner laboratory, and in-house system-level tests of using a commercially-available, residential packaged A/C unit which was retrofitted with a non-round tube prototype HX. It was found that HX designs proposed by the new framework can successfully predict experimental thermal-hydraulic performance within ±10-20% the first time with no manual design changes, eliminating the need for time-consuming and expensive prototyping efforts. This work will accelerate design and time to market for next generation HXs while simultaneously facilitating industry transition to new refrigerants at lower charge.

Table of Contents

Background

Note: The contents of this section have been published in the following citations: Tancabel et al., 2018 [1]*; Klein et al., 2018* [2]*; Tancabel et al., 2022* [3]*; Tancabel, 2022* [4]*; Klein, 2023* [5].

Motivation

The United States Energy Information Administration (EIA) reported that residential and commercial building energy end use in 2021 accounted for 39.2 quadrillion BTUs (QBTUs, quads), or about 40% of total United States energy consumption [6]. Of this energy consumption, Heating, Ventilation, Air-Conditioning, and Refrigeration (HVAC&R) equipment accounts for approximately 50% and 41% of residential and commercial building energy use, respectively. Additionally, recent energy conversion standards from the United States Department of Energy [7] for residential central air conditioners (A/C) and heat pumps (HP) require that all such systems manufactured after 01 January 2015 must have a Seasonal Energy Efficiency Ratio (SEER) exceeding 14.0 in order to avoid about 50 million metric tons of carbon dioxide (CO_2) emissions. Moreover, Kigali Amendment [8] requirements for the phase-out of hydrofluorocarbon (HFC) refrigerants in developed countries increases the demand for HVAC&R systems which utilize low global warming potential (GWP) and ozone depletion potential (ODP) refrigerants such as hydrocarbons (HCs), hydrofluoroolefins (HFOs) and other natural refrigerants such as carbon dioxide (CO_2), ammonia (NH_3), water (H_2O), etc.

As nearly all HVAC&R systems utilize air-to-refrigerant and liquid-to-refrigerant Heat eXchangers (HXs) as the main heat transfer components, improved HX performance is of utmost importance to improving overall HVAC&R system performance. Specifically, compact HXs, i.e., those with large heat transfer area to envelope volume ratio [9], have the potential to increase energy efficiency while reducing environmental impact. Specifically, finless HXs with small diameter tubes (e.g., <5.0 mm) have been shown to be more compact, utilize less refrigerant and material, and potentially outperform finned HXs [10]–[17]. Moreover, Westphalen et al. [18] noted that heat transfer enhancement in the form of doubling the condenser airside heat transfer coefficient could reduce cycle energy consumption by 10-15%, which would in turn reduce building energy consumption by 4.6-6.9%.

HX modeling and optimization is a key component of the design process, allowing researchers to investigate novel HX geometries and configurations prior to prototyping and experimentation, thus saving significant resources. Moreover, advancements in computational tools such as Computational Fluid Dynamics (CFD), Finite Element Analysis (FEA), optimization algorithms / techniques such as multi-objective genetic algorithms (MOGA) [19] and Approximation-Assisted Optimization (AAO) [20], along with improvements in advanced manufacturing such as Additive Manufacturing (AM) have led to a paradigm shift in HX design ideology.

This research sheds light on practical issues in HX modeling, design, optimization, and commercialization such as novelty challenges (improved performance for significant charge reduction; significant modeling expertise & time investment), manufacturing challenges (product qualification, e.g., burst pressure testing, operation in extreme environments, etc.), and operational challenges (flow maldistribution, frosting, fouling &

wetting, noise & vibration). For example, a >20% improvement on one (or more) HX-level performance metrics (e.g., envelope volume, airside pressure drop, face area, capacity, refrigerant charge, weight, cost, to name a few) must be achieved before a HX design is considered for commercialization.

Air-to-Refrigerant Heat Exchanger Shape & Topology Optimization

Introduction

As worldwide population continues to grow, researchers have dedicated significant time and effort in developing efficient and environmentally-friendly solutions to combat ever-increasing energy resource demands. In particular, the development of smaller, lighter, and more efficient air-to-refrigerant heat exchangers (HXs) has come to the forefront, as these components are critical to systems such as air-conditioners (condensers/evaporators) and automobiles (radiators), to name a few.

As HXs become more compact, the required thermal resistance can only be achieved through the utilization of extended secondary surfaces, e.g., fins. This is especially so for small characteristic diameter tubes, whose inadequate primary surface area alone cannot achieve the required thermal resistance. However, recent work [16] has suggested the existence of a trade-off between finless and finned surfaces. As tube diameter decreases, finless surfaces realize higher heat transfer coefficients at lower hydraulic resistances compared to finned surfaces. Significant research on the use of small diameter, round, finless tubes in HX design and their potential performance improvements has been conducted [10]–[17]. Advancements in computational tools such as Computational Fluid Dynamics (CFD) and optimization algorithms, coupled with the advent of additive manufacturing (AM) technologies, have allowed engineers to expand upon conventional HX design ideologies to include such concepts as shape and topology optimization, two methodologies which directly lend themselves to primary heat transfer surface optimization and, potentially, the complete removal of finned surfaces altogether.

Literature Survey: Air-to-Refrigerant HX S&T Optimization

A summary of HX shape and topology optimization models in literature is presented in Table 1. The major findings of these studies are presented in Table 2.

Table 1: Summary of air-to-refrigerant HX S&T optimization models.

Author(s)	Model(s)*	Study	Working Fluid(s)	Geometry Info.	Algorithm(s)	Validation
Stanescu et al. [21]	Analytical; Numerical (FEM)	T	Airside only	Round tube; no fin; staggered	Parametric study	Y
Paitoonsurikarn et al. [10]	Numerical (Eqns)	T	Air/Water	Round tube; no fin; staggered	Simulated annealing	Y
Wright [22]	Numerical (Eqns)	T	Air/R410A	Round tube; plain fin	Exhaustive search	N
Matos et al. [23]	Numerical (FEM)	S&T	Airside only	Round, elliptic tube; no fin; staggered	Parametric study	Y
Aspelund [24]	Numerical (Eqns)	T	Air/R410A	Round tube; plain fin; staggered	Simplex method	N

Stewart & Shelton [25]	Numerical (Eqns)	T	Air/Water	Round tube; no fin; staggered	CFD-trained neural network; Simulated annealing	Y
Kasagi et al. [12]	Numerical (FEM)	S&T	Airside only	Round & elliptic tube; plain fin; staggered	Parametric study	Y
Matos et al. [26], [27]	Numerical (CFD)	S	Airside only	NURBS tube; no fin; staggered	MOGA with CFD simulations	N
Hilbert et al. [28]	Numerical (CFD)	T	Air/Water	Webbed fin round tube; inline; staggered	MOGA with metamodels	Y
Abdelaziz [29]	Numerical (CFD)	T	Air/Water	Webbed fin round tube; inline; staggered	MOGA with metamodels	N
Abdelaziz et al. [30]	Numerical (Eqns)	T	Air/Water	Round tube; plain fin; staggered	NSGA-II	N
Saleh et al. [31]	Numerical (Eqns)	T	Air/R32; Air/R134a	Round tube; plain fin; microchannel	MOGA	N
Aute et al. [32]	Numerical (CFD)	T	Air/Water; Air/R410A	Round tube; no fin; inline; staggered	MOGA with metamodels	N
Hajabdollahi et al. [33]	Numerical (CFD)	T	Airside only	Round tube in hexagonal channel	NSGA-II	N
Qian et al. [34]	Numerical (CFD)	S	Airside only	NURBS tube; no fin; staggered	NSGA-II; FMOGA-II	N
Bacellar et al. [13]	Numerical (CFD)	S&T	Air/Water	Four tube geometries	MOGA with metamodels	N
Daroczy et al. [35]	Numerical (CFD)	S	Airside only	Round, elliptic, droplet tube; no fin; staggered	Parametric study	N
Ranut et al. [36]	Numerical (Eqns)	S&T	Air/R134a, Air/R290;	Variable tube and fin shapes	MOGA	N
Aute et al. [37]	Numerical (CFD)	S&T	Air/Water	Finless NURBS tube; webbed NURBS tube; airfoil tube; staggered	MOGA with metamodels	Y
El Gharbi et al. [38]	Numerical (CFD)	S&T	Air/Water	Round tube, webbed NURBS tube; staggered	MOGA with metamodels	N
Huang et al. [39]	Numerical (Eqns)	T	Air/Water	Microchannel; microstructure pin fin	Parametric study	Y
Bacellar et al. [14]	Numerical (Eqns)	T	Air/R410A	Round tube; no fin; staggered	MOGA	N
Bacellar et al. [40]	Numerical (Eqns)	S&T	Air/Water	Manifold microchannel	MOGA with metamodels	Y
Felber et al. [41]	Numerical (CFD)	S&T	Air/Water	NURBS tube; no fin; staggered	MOGA with metamodels	Y
Huang et al. [42]	Numerical (CFD)	S&T	Airside only	Elliptic tube	NSGA-II, neural network models	N
Arie et al. [43], [44]	Numerical (CFD)	T	Air/Water	Microchannel; microstructure pin fin	Method of Moving Asymptotes	N
Bacellar et al. [16], [45]	Numerical (CFD)	S&T	Air/Water	Bifurcated round tube	MOGA with metamodels	Y
Damavadi et al. [46]	Numerical (Eqns)	T	Air/Water	Round tube; plain fin	Heat transfer search	N

Haertel & Nellis [47]	Numerical (CFD)	S	Air/Water	Welded wavy plates	Grey correlation theory	Y
Huang [17]	Numerical (CFD)	T	Airside only	No fin; scaled teardrop shape; staggered	MOGA with metamodels	Y
Raja et al. [48]	Numerical (CFD)	T	Air/sCO_2	Full topology optimization of flow channels	Method of moving asymptotes	Y
Zhicheng et al. [49]	Numerical (CFD)	T	Air/Water	Round tube; no fin; staggered	MOGA with metamodels	Y
Han et al. [50]	Numerical (CFD)	T	Air/Fluid Fluid/Fluid	Full topology optimization of flow channels	Boundary variation method	N
Saviers et al. [51]	Numerical (CFD)	S&T	Air/Water	Ogive tubes; no fin; staggered	MOGA with metamodels	Y
Lim et al. [52]	Numerical (CFD)	T	Air/Fluid	Fixed round tubes; full TO for fins	Method of moving asymptotes	N
Feppon et al. [53]	Numerical (CFD)	T	Air/Fluid	Round tube twisted tube bank; no fin	Parametric study	N
Kang et al. [54]	Numerical (CFD)	T	Air/Fluid	Annular radiator; plane fins	NSGA-II	Y
Liu et al. [55]	Numerical (CFD)	T	Air/Fluid	MCHX with plain fins;	MOGA with metamodels	N

Table 2: Summary of major findings in air-to-refrigerant HX S&T optimization literature.

Author(s)	**Objective Function(s)**	**Major Findings**
Stanescu et al. [21]	• Max q'''	• Opt. spacing (↓) as velocity (↑) and flow depth (↓) • Experimental validation of analytical & numerical models
Paitoonsurikarn et al. [10]	• Min pumping power • Max Q • Min V_{HX}	• Small diameter (0.3 – 0.5 mm) finless round tubes significantly outperform baseline HX • Pumping power 37-56%↓ for same Q, V_{HX} • Q 17-33%↑ for same pumping power and V_{HX} • V_{HX} 57-74%↓ for same Q and pumping power
Wright [22]	• Max seasonal COP	• Small diameter tubes give higher system COP
Matos et al. [23]	• Max q'''	• Model validated with Stanescu *et al.* (1996) experiments • $\Delta P_{a,ellipse} < \Delta P_{a,round}$ $h_{a,ellipse} > h_{a,round}$
Aspelund [24] Stewart & Shelton [25]	• Min pumping power • Max Q • Min V_{HX}	• Updated Paitoonsurikarn et al. [10] model • CFD-trained neural network to predict airside performance • Applications: Automotive HX; Electronics cooling; micro gas turbine recuperator
Kasagi et al. [12]	• Max q'''	• Validaton for both circular and elliptic geometries • $M_{Matl,ellipse} < M_{Matl,round}$
Matos et al. [26], [27]	• Max ΔT_a; Min ΔP_a	• First paper on HX tube shape parametrization with NURBS • Varying airfoil-like tube shapes
Hilbert et al. [28]	• Max Q/A_f, Q/V_{HX}, Q/M_{Matl} • Min ΔP_a	• Novel method (offline AAO) to study heat transfer surfaces • DoE evaluated using Parallel Parameterized CFD (PPCFD) • Significant objective function improvements • Validation with prototyped optimal design (±10% agreement)
Abdelaziz [29] Abdelaziz et al. [30]	• Max h_a; Min ΔP_a	• Extends AAO to Online AAO (OAAO)

		• OAAO opt. designs better or equal to offline AAO opt. designs
Saleh et al. [31] Aute et al. [32]	• Max seasonal COP or Min entropy generation	• Optimize HX as an isolated component or in system context
Hajabdollahi et al. (2011) [57]	• Max thermal effect • Min cost	• Effectiveness and cost increase with tube diameter and decrease with increasing tube pitch
Qian et al. [34]	• Min ΔP_a, V_{HX}	• AAO (Abdelaziz *et al.*, 2010) metamodels produced using novel adaptive Design of Experiments (DoE) technique • Airside ΔP: ~87% (↓); V_{HX}: ~44% (↓)
Bacellar et al. [13]	• Max Q • Min entransy dissipation; entropy generation; cost	• No significant difference between capacity, entransy dissipation and between entransy dissipation and entropy generation
Daroczy et al. [35]	• Min ΔP_a, V_{HX}	• Opt. designs 50% smaller, 2-4 times higher material utilization • ΔP_a: 75% (↓); h_a: 100% (↑)
Ranut et al. [36]	• Min equivalent ΔP, V_{HX}	• Opt. designs symmetric about channel centerline • Potential to include HX size minimization as objective function
Aute et al. [37]	• Max Q; Min ΔP_a, ΔP_r	• Second paper on HX tube shape parameterization with NURBS • Low ΔP_a tubes have low h_a and ΔP_r compared to bluff-body tubes
El Gharbi et al. [38]	• Min ΔP_a, V_{HX}, A_f	• First paper mentioning webbed shape-optimized tubes • Opt. designs have 50% size, material, and ΔP_a reduction • Approach temperature: 20% (↓)
Huang et al. [39]	• Max Nusselt number, Euler number, entropy generation	• Direct comparison of round, elliptic, and droplet shape tubes • Round tubes: best heat transfer; highest pressure drop • Elliptic / droplet tubes: Similar thermal-hydraulic performance
Bacellar et al. [14]	• Min M_{Matl}; Max Q	• First variable geometry HX study in literature • Material usage: 35% (↓); V_{HX}: 43% (↓)
Bacellar et al. [40]	• Min ΔP_a, V_{HX}	• Validation with metal AM prototype • Leverage boundary layer detachment/reattachment mechanism • V_{HX} and pumping power: 50% (↓)
Felber et al. [41]	• Min A_f • Max $h_a/\Delta P_a$, j/f, novel PEC	• New PEC to fairly compare multiple HX geometries • HX decision-making criteria (Multi-Attribute Utility Function) • Significant face area reduction and aspect ratio improvement
Huang et al. [42]	• Min V_{HX}	• Partial validation with polymer 3D-printed prototype • Low polymer thermal conductivity limit model applicability
Arie et al. [43], [44]	• Max Q • Min entransy dissipation; entropy generation; cost	• Low capacity: capacity entransy dissipation largely similar • Higher capacity: entransy dissipation and capacity should be considered as separate objective functions
Bacellar et al. [16], [45]	• Max COP, gravimetric heat transfer density	• Direct laser metal sintering for prototyping and validation • Gravimetric heat transfer density: 60% (↑)
Damavadi et al. [46]	• Min ΔP_a, V_{HX}	• First coupled shape-topology opt. framework in literature • First shape-optimized prototype of NURBS-tube HX • Framework validated for dry condition, tested for wet condition
Haertel & Nellis [47]	• Max j; Min f	• Smaller tubes result in better heat transfer and worse ΔP

Huang [17]	• Max HX conductance	• Airside microstructure optimized to any topology • Prototypes manufacturable using polymer AM • Topology-opt. allows low conductivity material utilization
Raja et al. [48]	• Min pumping power, V_{HX}	• Novel bifurcated HX tubes • ΔP_a: 35%(↓); A_f: 78%(↓); Ref. charge: >40%(↓) • Model framework validated using polymer AM prototype
Zhicheng et al. [49]	• Min coil weight, total annual cost	• Opt. design weight: 16% (↓) • Opt. design annual cost: 9% (↓)
Han et al. [50]	• Max Webb efficiency (Webb, 1981)	• Developed optimized, and prototyped concept wavy plate HX • Opt. design efficiency approx. double the baseline
Saviers et al. [51]	• Max Q, Min ΔP_a	• Application: ABS Polymer HX • HX performance is 92.7% - 162.8% of baseline HX at 300 m^3/hr air flow rate • Optimal polymer HX design Q 141.6%↑ compared to MCHX also using polymer
Lim et al. [52]	• Max Q	• Full topology optimization yields “organic” vascular-type flow channels • Optimal HX ΔP 2-4x↓ with 2.0x↑ Q • 3D-printed polymer prototype for experimental validation
Feppon et al. [53]	• Max Q, Min ΔP_a	• Optimum HX uses 0.6849 mm inner diameter round tubes • Optimized HX ΔP 1.0%↑ vs. baseline aluminum MCHX • Optimized HX Q 7.0%↓ vs. baseline aluminum MCHX
Kang et al. [54]	• Max Q	• Constraints on flow channel thickness and fluid pressure drops • Applications to 2D (cross flow) and 3D (fluid-fluid) HXs
Liu et al. [55]	• Max Q, Min ΔP_a	• Ogive tube cross section with two different length formats: (i) straight tube and (ii) sinusoidal tube • Optimized HX ΔP 34.9%↑ vs. baseline aluminum MCHX • Optimized HX Q 7.0%↓ vs. baseline aluminum MCHX • Sampled ogive sinusoidal HX delivered similar Q with ΔP_a 22%↓ and 7.8% fewer tubes vs. Han et al. optimal teardrop tube HX
Rawa et al. [56]	• Max Q	• Full topology optimization for manufacturable fin geometries • Opt. vs. conventional fin: 22-28%↑ thermal performance; 33-48%↑ pressure drops, ~13% improved total performance
Xu et al. [57]	• Max COP • Max CEP (exergy) • Max second law efficiency	• “Twisted tube bank” geometry: first tube banks reference; subsequent tube banks (depthwise direction) rotated by a fixed “optimal” angle • Optimum twist angles of 43° and 84°
Garcia et al. [58]	• Max Q, Min ΔP_a	• Application: annular radiator for aero-engine oil cooler • Optimized HX Q 34.3%↑ on average vs. baseline HX • Optimized HX ΔP 24%↓ on average vs. baseline HX

Optimal Design Prototyping & Experimental Validation

Optimization aims to develop next generation technologies to replace the current state-of-the-art. However, optimized, especially shape-optimized, HXs face significant tech-to-market barriers due to difficulties which may arise from the inability to use conventional manufacturing to produce the optimal design. Further, non-round, shape-optimized tubes may lack the structural integrity which is inherent to round tubes, requiring additional structural analysis simulations to verify tube structural integrity. Therefore, it is of interest to prototype optimal designs to (i) validate optimization frameworks and (ii) provide the HVAC industry with evidence to further investigate and potentially implement new HX geometries.

Conventional HX prototyping focuses on non-AM prototypes. Stanescu et al. [42] performed experiments on a round tube array to experimentally validate their findings on optimal tube spacing. Matos et al. [23] validated their CFD models using the experiments of Stanescu et al. [21]. Matos et al. [26], [27] also prototyped and conducted experiments on a finned round tube HX and an optimal finned elliptic tube HX for model validation. All studies by Matos et al. [23], [26], [27] resulted in the baseline round tubes being shape- and topology-optimized to more streamline elliptical tubes. Abdelaziz [29] experimentally validated their unified HX design and optimization framework for a single tube row. Zhicheng et al. [49] experimentally validated a wavy plate HX design using a gas-water heat recovery system. Lim et al. [52] developed two finless, aluminum HX prototypes with round tube outer diameters of 1.0 mm and 1.4 mm using aluminum brazing. These HXs were later used to experimentally validate the models proposed by Han et al. [50] and Kang et al. [54].

Most shape-optimized HXs cannot be economically manufactured using conventional methods due small feature sizes and thin material thicknesses. However, AM represents a unique opportunity since complex geometries can be easily produced provided that geometric features fall within prescribed limits. HXs have been prototyped using both polymer and metal AM, which are treated separately:

- Multiple HXs have been prototyped using polymer AM, indicating its viability and future potential. Arie et al. [43], [44] utilized 3D laser welding to fabricate a manifold microchannel HX in polymer, while Felber et al. [41] utilized polymer AM to prototype and validate a microchannel HX which featured topology-optimized airside microstructures. Huang [12] applied polymer AM to validate a novel bifurcated round tube HX concept. Saviers et al. [51] additively manufactured a topology optimized gas cooler using urethane methacrylate (UMA 90) to validate their simulated 2-times improvement in pressure drop and 10% higher temperature change compared to the baseline gas cooler.
- Bacellar et al. [16] experimentally validated their HX multi-scale analysis and shape optimization framework using a metal AM prototype. Their novel, shape-optimized, metal AM HX remains the first of its kind in published literature. As a result, metal AM HX prototyping could represent a significant research opportunity in HX design.

Multi-Physics Modeling of Air-to-Refrigerant HXs

This works examines three additional physics phenomena (beyond airside analysis) which are key contributors to the multi-physics performance of an air-to-refrigerant HXs: (i) tube-level structural strength; (ii) single phase flow in small diameter flow channels; and (iii) tube bundle aeroacoustics.

HX Tube Structural Strength

Comprehensive product acceptance and qualification testing is required prior to a HX being approved for its specific application, whether it be HVAC&R, aircraft, military, or otherwise (Table 3) [59]. Among the most important qualification tests is the burst pressure test, where the HX must not rupture (or "burst") when pressurized to 2.5 times [77], 3.0 times [78], or 5.0 times [79] the operating pressure, depending on the burst pressure testing standard. In the context of this research, we consider the impact of the burst pressure test on the tubes themselves rather than the full HX, which also includes considerations for the tube-header joints, fins, fittings, etc.

Table 3: Summary HX product acceptance & qualification tests (Adapted from Ranganyakulu and Seetharamu [59]).

Test	Test Name	Test	Test Name
1	Visual examination	8	Thermal shock
2	Leakage test	9	Acceleration
3	Pressure drop test (i) Fluid-side (ii) Airside	10	Shock
4	Proof pressure test	11	Humidity
5	Thermal performance	12	Fungus
6	Vibration	13	Salt fog
7	Pressure cycling	14	Burst pressure test

Much of the literature for modeling HX structural strength focuses on plate-fin and shell-and-tube HX geometries and numerical simulations for fluid-structural interaction [60]–[63], which fall beyond the scope of this work. From the tube-level perspective, a large amount of literature focuses on shell-and-tube HXs, which are not the direct focus of this work (i.e., cross flow, air-to-fluid HXs). However, Harhara and Hasan [64] note that tube rupture events in shell-and-tube HXs are more likely for large pressure differences between the shell-side and tube-side, which can be the case for air-to-fluid HXs (P_{air} ~ 0.1 MPa, P_{fluid} ~ 0.2 – 20 MPa). For air-to-refrigerant applications, many studies in literature focus on tubes in both aluminum and copper. A summary of pertinent literature is presented in Table 4.

Table 4: Summary of air-to-refrigerant HX tube structural strength literature.

Author(s)	Tube Geometry	Material(s)	Application	Key Findings
Kraft [65]	Multi-port rectangular channel	Aluminum	Automotive climate control system	• Three tube/port geometries • Burst pressure model built using true stress/strain results
Vamadevan [66]	Multi-port rectangular channel	Aluminum	Automotive climate control system	• Carbon dioxide (CO_2) as refrigerant • Static and cyclic pressure testing • Model to predict maximum tube webbing stresses
Miller [67]	Multi-port rectangular channel	Aluminum	Automotive climate control system	• Carbon dioxide (CO_2) as refrigerant • Model to predict maximum burst pressure at room and elevated temperatures
Huang [68]	Multi-port rectangular channel	Aluminum	Condenser	• Numerical modeling (FEA) of four port shapes • Octagon port reduced burst pressure by 27% vs. rectangular port
Kraft & Jamison [69]	Round tube	Copper	HVAC&R	• Tube OD: 15.87-53.97 mm • Pressures: 4.38-10.34 MPa (or burst)

				Model sufficiently accurate for burst pressure prediction
Qi [70]	Multi-port rectangular channel	Copper	HVAC&R	As-extruded, cold rolled, & rolled-heat treated tubes tested Model to predict burst pressure
Fan et al. [71]	Multi-port rectangular channel	Aluminum	N/A	Microstructure development for porthole die extrusion
Tang et al. [72]	Multi-port rectangular channel	Aluminum	N/A	Microstructure development for extrusion, rolling, & brazing
Qian et al. [73]	Single tube	Stainless steel	N/A	Two tubes: (i) spirally-grooved; (ii) converging-diverging vs. round tube New tubes have higher yield & ultimate strength but lower fatigue resistance
Wu et al. [74]	Single tube	Stainless steel	N/A	Conically-corrugated tube vs. Qian et al. [93] tubes New tube has higher yield & ultimate strength but lower fatigue resistance New tube has 115% higher heat transfer coefficient vs. round tube

Single-Phase Flow in Small Diameter Flow Channels

The accurate prediction of the thermal-hydraulic performance in small diameter tubes is of the utmost importance to ensure that heat transfer components are properly sized. To this end, researchers have placed significant effort into developing correlations for entrance region and fully-developed laminar and turbulent flows for conventional tube sizes and shapes. Such correlations are summarized in multiple comprehensive reviews from open literature on the topic ([75]–[79]). Nevertheless, to the author's knowledge, no comprehensive CFD-based models are available to evaluate tube-side (internal flow) thermal-hydraulic performance for generalized, non-round, tube shapes, and no thermal-hydraulic performance correlations exist for generalized, non-round, flow channels.

Air-to-Refrigerant Heat Exchanger Aeroacoustics Modeling

Another consideration for HVAC&R system engineers beyond thermal-hydraulic performance is potential noise and vibration problems [80]. ASHRAE defines noise as "any unwanted sound", and that "sound" becomes "noise" when it is too loud, unexpected, uncontrollable, untimely, unpleasant, contains unwanted tones and/or information, etc. [81], [82]. The noise levels and disturbances resulting from A/C units has been well studied [80], [83]–[85], with human responses being strongly correlated to the level by which the noise exceeds ambient noise levels [85]. Many references are available for measuring, controlling, and rating noise and vibration in HVAC&R systems [80]–[82], [86], [87], all with the objective of ensuring that (i) the noise is unobtrusive and (ii) noise levels do not exceed the existing ambient background noise. Such standards largely focus on the mechanical system components (e.g., fans, dampers, diffusers, duct / duct junctions, compressors, etc.).

The HX tube bundles themselves can also emit large amounts of noise as a result of acoustic resonance associated with fluid-elastic instabilities linked to turbulent air cross-flow over the tube bundles [88]–[95]. To avoid resonance, Gelbe & Ziada [95] recommend maintaining the maximum air flow velocity to below 80% of the critical velocity associated with acoustic resonance. To this end, outdoor HVAC&R units (e.g., condenser units in split A/C systems operating in cooling mode) are typically designed according to a rule of thumb where inlet air velocity is below 1.0 m/s to avoid aeroacoustics-generated noise [96].

Additively Manufactured Heat Exchangers

Introduction

Compact bare tube heat exchangers with non-circular/uniform cross sections can be designed and optimized within a reasonable amount of computational power, but the manufacturing methods need to exist to build them. Many of these adjoint method optimized designs have unconventional shapes and vary throughout the entire heat exchanger. Additive Manufacturing (AM) has the potential to facilitate great innovation for the next generation of more efficient heat exchangers as it can manufacture many of these unique designs. Heat exchangers have previously, and still do today, rely on traditional manufacturing methods such as milling, die-casting, alignment, brazing/welding, or a combination of processes to mass produce cost efficient products [97]. Typical compact heat exchangers, such as microchannel heat exchangers, use fins to augment heat transfer and are manufactured using stamping or folding techniques [98]. These methods limit the types of geometries and size and thickness of features, such as tube walls, that can be fabricated. AM could mitigate these limitations. AM is the creation of three-dimensional objects by joining materials together, usually layer-by-layer. Typically, a 3D Computer Aided Design (CAD) model is created and then fed to splicing software, which divides the model into thin horizontal slices. These slices act as instructions for the 3D printer which creates each individual layer one at a time. AM is not limited to just using traditional plastics, but also can create parts composed of metal alloys, ceramics, composites, and even biological materials [99]. Manufacturers are beginning to take advantage of the new technology. Since parts are built by adding successive layers, complex internal geometries can be built with one monolithic build. This coupled with the fact that different types of materials can be used, facilitates the production of heat exchangers that use less material, have lower volume, and have increased thermal performance and reliability. Considering AM allows for rapid low-cost prototyping, researchers can design, fabricate, and test novel heat exchangers within a short period of time. One of the earliest examples of researchers taking advantage of metal AM to produce and test a heat exchanger was done in 2006 by Tsopanos et al. [100]. Two micro-scale heat exchangers and three meso-scale heat sinks were rapidly manufactured using Selective Laser Melting (SLM) and the thermal performance experimentally determined. This literature review found the number of researchers using AM to create new cutting-edge heat exchangers and heat sinks has rapidly increased over the past five to ten years.

Minimum Feature Size

As the accuracy of AM increases, the possibility to design and manufacture extremely thin features arises. These extremely thin features facilitate the creation of new geometries, increased complexity at smaller scales, and most importantly the reduction of tube wall thickness. As the wall thickness becomes smaller, the overall thermal resistance decreases and hence the effectiveness of the heat exchanger increases as well. Thus, smaller and more compact heat exchangers can be designed and manufactured. The minimum feature thickness obtainable is dependent on the AM process and material used. Table 5 provides a summary of some of the smallest features manufactured for metal, polymer, and ceramic AM found in the literature. This provides a rough estimate of what the current technological limit is. A study by Arie et al. [98] suggests with current DMLS AM technology, the safe manufacturing limit of metal fin thickness is 0.3 mm, the technological limit is 0.15 mm, and the future technological projection is 0.05 mm. Note that this is for fins, not tube or plate walls which have to hold a certain amount of pressure and separate the two active fluids.

Table 5: Smallest feature thickness attainable using AM for different materials.

Material	Reference	AM Process	Wall Thickness
Metal	[98]	Direct Metal Laser Sintering (DMLS)	~150 μm
Polymer	[101]	Polyjet	~32-100 μm
Ceramic	[102]	Lithography-based Ceramic Manufacturing (LCM)	~100 μm

Additively Manufactured Heat Exchanger Literature Review Summary

Table 6 – Table 8 summarize all studies which used additive manufacturing to produce a heat exchanger in metal, polymer, and ceramic, respectively.

Table 6: Summary of metal AM HX studies.

Reference	AM Process	Summary/Major Findings
Tsopanos et al. [100]	SLM	• Micro scale heat exchangers and meso scale heat sinks were manufactured. • Micro scale heat exchangers demonstrated consistent performance with those considered in previous research. • Meso scale heat sinks did not perform as well as existing pin-fin designs.
Wong et al. [103]	SLM	• Heat transfer and pressure loss characteristics of four heat sinks experimentally studied. • Aluminum 6061 proven to as a viable material to be used with SLM.
Wong et al. [104]	SLM	• Five heat sink geometries manufactured using Aluminum 6061. • Lattice-structure heat sink demonstrates that increasing surface area alone does not necessarily improve the overall heat transfer performance.
Wong et al. [97]	SLM	• Three novel finned structures manufactured using Aluminum 6061 and Stainless Steel 316L. • Heat sinks produced showed superior performance to the conventional heat sinks. • New geometries incurred lower pressure drop.
Yan et al. [105]	DMLS	• Evaluates the manufacturability and performance of AlSi10Mg periodic cellular lattice structures. • DMLS can be used with this new alloy to produce porous lattice structures.
Ventola et al. [106]	DMLS	• When compared to smooth surfaces, rough flat surfaces and finned surfaces produced with DMLS respectively experienced on average 63% and 35% better convective heat transfer.
Pakkanen et al. [107]	SLM	• Cylindrical geometry for internal channels built at different angles using AlSi10Mg and Ti6Al4V and internal surfaces analyzed. • Surface roughness of internal channels evolve depending on building angle.
Arie et al. [98]	DMLS	• Implementation of DMLS was studied on a manifold-microchannel heat exchanger.

		• Manifold-microchannel geometry using DMLS offers significant improvement over state-of-the art advanced fin technologies.
Arie et al. [43]	DMLS	• Fabricated and experimentally tested a high-performance titanium alloy air-water heat exchanger that utilizes manifold-microchannel design. • Demonstrated a 45-100% increase in base conductance and 15-50% increase in heat transfer coefficient for the same pressure drop compared with wavy-fin surfaces.
Stimpson et al. [108]	DMLS	• With decreasing hydraulic diameters, the friction factors increased as a consequence of higher roughness-to-hydraulic diameter ratios. • Channels made with DMLS have relatively comparable thermal performance to channels with grooves.
Kirsch and Thole [109]	DMLS	• Three wavy channel coupons, each containing channels of varying wavelength, were designed and additively manufactured to evaluate pressure loss and heat transfer performance of the channels.
Snyder et al. [110]	DMLS	• Cylindrical-shaped channels built in three different orientations, while teardrop and diamond shaped channels built horizontally. • Vertically built channels had the lowest friction factor, while the diagonally built coupons had the highest friction factor.
Stimpson et al. [111]	DMLS	• Developed correlations that relate the physical roughness measurements to the effect the roughness has on the flow friction and heat transfer. • Heat transfer correlation is presented which predicts Nusselt number of flow through DMLS microchannels using predictions or measurement of friction factor.
Bernardin et al. [112]	DMLS	• Presented a process to improve the thermal performance of a twisted shell-and-tube heat exchanger by leveraging CFD -modeling and expanded fabrication space of AM. • Modeled to have a 40% increase in heat transfer coefficient.
Bacellar et al. [16]	LPBF	• A new bare tube heat exchanger was designed and additively manufactured using laser powder bed fusion. • Achieved ~20%reduction in size, ~20% reduction in air pressure, ~40% reduction in material volume, and ~2% reduction in face area compared to a microchannel heat exchanger.
Ibrahim et al. [113]	LPBF	• L-PBF used to fabricate a multi-layered, Ti-6Al-4V oscillating heat pipe(ML-OHP) • Characterized the ML-OHP thermal performance.
Garde [114]	SLM	• Additively manufactured oil cooler was designed and manufactured using SLM • Design is projected to transfer heat at 15kW at the design conditions
Gerstler and Erno [115]	DMLS	• Novel heat exchanger designed to meet the heat transfer and fluid pressure drop requirements of a turbine engine fuel cooled oil cooler. • Mass and volume of the heat exchanger is 66% and 50% lower than the legacy fuel cooled oil cooler with similar performance.
Korinko et al. [116]	SLM	• Type 316 Stainless Steel printed tubing has a higher mechanical strength and lower ductility than annealed Type 316L Stainless Steel.
Arie et al. [44]	DMLS	• Three prototype heat exchangers were fabricated out of stainless-steel, titanium alloy, and aluminum alloy for power plant air-water heat exchangers. • Improvement in gravimetric heat transfer density compared to wavy fin heat exchanger.
Hathaway et al. [117]	SLM	• Commercial -scale tube bank oil cooler fabricated. • Unique features include, lenticular tubes with offset strip fins, and angled plate-fins.
Jazi et al. [118]	Wire-Arc Spraying	• Dense, alloy 625 deposited on the surface of 10 pores per inch (PPI) and 20 PPI nickel foam sheets to fabricate compact heat exchangers. • 20 PPI foam showed higher resistance to flow and greater heat transfer than the 10 PPI foam because of its smaller pore size and larger internal surface area.
Cormier et al. [119]	CGDS	• Pyramidal fin array produced with CGDS outperformed traditional straight cut fins at the same fin density and hydraulic diameter due to fluid mixing increasing the convective heat transfer coefficient.
Cormier et al. [120]	CGDS	• Investigated the effect of varying the fin height and the fin density of pyramidal pin fins. • Increasing either fin height or fin density also increases the total thermal conductivity at the expense of a higher-pressure loss.
Dupuis et al. [121]	CGDS	• Two new geometric pin fin arrays manufactured; pyramidal and trapezoidal fin arrays.

		• Two new geometries have better heat transfer performance than traditional plain rectangular fins, but larger pressure loss.
Farjam et al. [122]	CGDS	• Pyramidal fin arrays with different volume fractions of aluminum-alumina were produced. • Use of Aluminum-Aluminum feedstock powder as an alternative to pure aluminum prevents the use of costly polymer nozzles that wear out quickly.
Cormier et al. [120]	CGDS	• Near-net-shaped pyramidal fin arrays of various materials were manufactured; including aluminum, nickel, and grade 34 stainless steel. • The aluminum powder outperformed the other materials.
Dupuis et al. [123]	CGDS	• Pyramidal pin fins fabricated using CGDS. • Classic double recirculation structures, and flow bypass structures observed in wake regions of fins.
Dupuis et al. [124]	CGDS	• Pressure losses and the convective coefficients of square base, round base and diamond base tapered pin fins. • Staggered configurations produce higher convective coefficients and higher-pressure losses.

Table 7: Summary of polymer AM HX studies.

Reference	AM Process	Summary/Major Findings
Harris et al. [125]	LIGA	• Cross-flow micro heat exchanger was developed to provide function similar to a car radiator. • Micro heat exchanger demonstrated good heat transfer rate/volume ratio.
Deisenroth et al. [126]	LPW	• Provides a thorough review of polymer heat exchangers. • Case study presented of an air-to-water heat exchanger constructed using Laser Polymer Welding. • Polymer heat exchanger required 85% less mass, but 35% more volume than a metallic wavy fin heat exchanger of the same capacity. COP also increased by 27%.
Rua et al. [101]	Polyjet	• Aimed to quantify the limitations of the AM process when used for printing microfluidic channels in heat exchanger fins. • .032mm-.1mm walls were possible to clean with care, but deformed slightly under pressure.
Arie et al. [43]	LPW	• LPW or layer-by-layer line welding by laser was used to fabricate an air-to-water heat exchanger. • Extremely thin walls (150 μm) reduced the thermal resistance of the wall to only 3% of the total thermal resistance.
Felber et al. [41]	FDM	• Prototype air-to-water heat exchanger designed and printed using FDM. • Improving the thermal conductivity for the printed polymer directly affects the heat exchanger performance, but this is a non-linear relationship.
Cevallos [127]	FDM	• Novel polymer composite heat exchanger, called a webbed-tube heat exchanger. • Design shown to have similar performance to a plate-fin heat exchanger but used less material volume.

Table 8: Summary of ceramic AM HX studies.

Reference	AM Process	Summary/Major Findings
Liu et al. [128]	Mould Shape Deposition	• Fabricated micro heat exchanger with four and 40 channels out of silicon carbide.
Shulman & Ross [129]	LOM	• Demonstrated complex ceramic heat exchangers can be built using LOM processes. • Ceramic heat exchanger could be manufactured at a reasonable cost.
Schwarzer et al. [130]	LCM	• Demonstrated the creation of complex designs using LCM. • Components with densities after sintering higher than 99% were achieved.
Scheithauer et al. [102]	LCM	• LCM allowed the production of alumina and zirconia components. • A heat transfer surface of more than 3500mm^2 and holes with a diameter if 0.2mm can be realized.

Cost Competitiveness

The question posed is whether AM can be as cost effective as traditional manufacturing methods. AM offers many advantages over traditional manufacturing. The absence of tooling takes away a significant cost in the product development process at an early stage and changes to a part geometry may be applied without the need to incur the times and costs of producing new tooling [131]. Also, by fabricating parts on demand using AM, holding stock can be reduced and consequently reduce cost. Raw materials for AM production are the only stock required [132]. Multiple models have been proposed predicting and comparing the cost of AM to traditional manufacturing methods. The first notable model is by Hopkinson and Dickens [131]. Figure 1 shows the cost comparison for a part using SLS and the conventional manufacturing method, high pressure die-casting. The initial start-up cost of traditional manufacturing methods, such as injection molding allows AM to be much more cost effective below a certain production volume. However, the opposite is true as the production volume increases further. A study by Laureijs et al. [133] showed that additively manufacturing a GE engine bracket is cheaper than the traditionally manufactured forged part for a wide range of scenarios at high production volumes. Thomas and Gilbert [134] provides a thorough review of the cost advantages of AM and explains multiple different cost models. Heat exchangers are very complex parts and many of these studies only provide cost analyses for simple parts or assemblies. It would be beneficial to know how the complexity of the part affects the cost competitiveness of using AM versus traditional manufacturing. Fera et al. [135] propose a new model which uses complexity of the part being manufactured as a decision driver for the use of AM and not the number of products to manufacture. Most of the models presented do not take into full account the benefits AM has to offer and models still have progress to be made to better predict the economic competitiveness of AM. From the models discussed, the production volume and part complexity can be used to determine whether manufacturing a heat exchanger with AM methods can be cost competitive to traditional manufacturing methods.

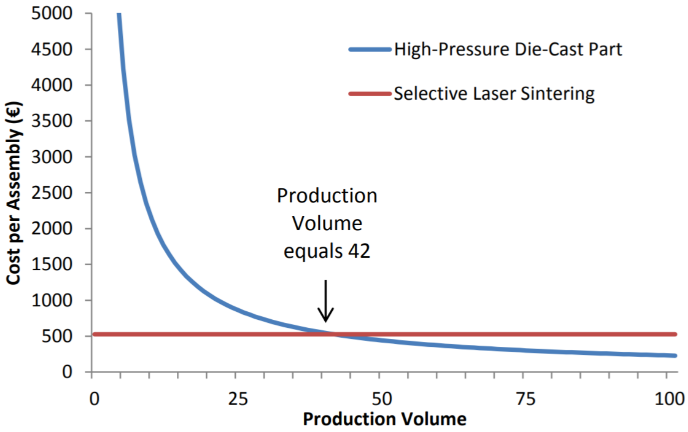

Figure 1: Cost comparison of AM to Conventional manufacturing methods [134].

Research Gaps

Based on the current literature review, the research gaps are as follows:

- Air-to-Refrigerant HX Optimization
    - Two-phase HXs with shape-optimized tubes have not been well-studied;
    - Few studies in literature consider the modeling of tube structural integrity for air-to-refrigerant applications, which may result in HXs that are significantly under-designed for safety, leakage, and product qualification;
    - There is a lack of HX optimization studies considering next generation, e.g., low GWP, refrigerants.
        - Continued interest in transitioning to next generation, low-GWP refrigerants, coupled with the development of novel HXs which can simultaneously reduce charge, weight, and size for the same overall performance presents a unique opportunity in HX design.
- Multi-Physics Modeling of Air-to-Refrigerant Heat Exchangers
    - Mechanical Modeling
        - Burst pressure modeling literature typically focus on conventional geometries such as round tubes or multi-port tubes.
        - Existing work with non-round tube bundles (e.g., Bacellar et al. [16]) utilized conservative tube thicknesses to guarantee tube structural integrity prior to prototyping, resulting in greater material consumption, which increases the overall HX material costs.
            - In their work, tube thickness reductions could only be realized following detailed and oftentimes computationally expensive FEA modeling on each candidate tube geometry to verify whether the required pressure-holding capability was met.
        - No comprehensive fatigue modeling has been conducted for non-round tube bundles and non-round tube-header joints / full HX assemblies.
    - Single-Phase Flow in Small Diameter Flow Channels
        - No tube-side (internal flow) thermal-hydraulic performance correlations exist for generalized, non-round, flow channels;
        - No comprehensive CFD-based models are available to evaluate tube-side thermal-hydraulic performance for generalized, non-round, tube shapes.
    - Air-to-Refrigerant Heat Exchanger Aeroacoustics Modeling
        - No generalized models exist for predicting aeroacoustics noise for tube bundles with non-round, shape and topology-optimized tubes. Existing models are only applicable to round tubes with fixed layouts (45° and 60° configurations) [95].
        - Existing work with non-round tube bundles have reported significantly smaller frontal areas and thus higher inlet air velocities than given rules of thumb (1.0 m/s). It is not well known whether the higher operating inlet air velocities have a detrimental impact on HX aeroacoustics performance.
    - Dehumidification Modeling of Air-to-Refrigerant Heat Exchangers

    - Existing dehumidification models and correlations are only applicable for large diameter (≳ 7 mm OD) round tubes and flat multiport tubes (usually finned) and are tuned specifically to the geometry of interest.
- Additive Manufacturing of HXs
  - The use of additive manufacturing to construct optimal HX geometries has rapidly expanded in the past decade as it is able to realize previously impossible to manufacture HX designs.
    - However, the consequences of using said technology for heat transfer devices are not yet fully understood. There lacks experimental evaluation of additively manufactured HXs.
  - Additionally, additive manufacturing is not yet cost competitive to traditional manufacturing methods, requiring the investigation of novel manufacturing methods which are highly scalable to enable mass-production of novel HXs for all kinds of applications, including HVAC&R.

Project Objectives

The main objective of this project is to design high performance air-to-refrigerant HXs that are 25% lighter and 25% more compact with a HX charge reduction of 30% compared to A/C systems available on the market today. The reduced charge advantage will facilitate the use of A2L and A3 refrigerants for certain applications. In addition to the performance targets, the HXs are also expected to address the challenges of non- round tube production and water bridging on small diameter tubes during dehumidification. The project is expected to deliver HX prototype(s) to US manufacturers for independent tests and validations. The SOPO table is summarized in Table 9.

Table 9: SOPO Table.

Task Number	Task / Subtask Title	Milestone Type	Milestone Number	Milestone Description
1	IPMP Development	-	-	• IPMP signed by all relevant parties & submitted to DOE
2	Finalize non-round tube design & establish mfg. approach	[redacted]	[redacted]	[redacted]
2.1	Determine baseline HXs	Regular	M2.1	• Baseline HX performance defined for project • DOE & UMD agree upon baseline HX specifications
2.2	Structural analysis model development	Regular	M2.2	• FEM / FEA model developed • Model results compared with existing literature measurement
2.3	HX opt. framework development	Regular	M2.3	• HX optimization framework developed • Opt. framework delivered with capability of optimizing non-round tube; results verified against existing data from literature
2.4	Investigate non-round tube mfg. & tube/header integration methods	Regular	M2.4	• Non-round tube mfg. & HX integration methods finalized
2.5	Conduct opt. on small diameter non-round tubes	SMART	M2.5	• Deliver set of optimal non-round tubes • Targets: 20% lighter, 15% better heat transfer, 40% charge reduction on a tube level vs. selected baseline
[redacted]	[redacted]	G/NG	G/NG #1	• Deliver set of optimal non-round tubes (25% lighter, 25% more compact, 30% charge reduction on HX level) vs. the baseline from M2.1 • Report non-round tube mfg. options & HX assembly methods that passed tests on holding pressure & holding original shape
3	Design, fabricate, & test HX prototypes with non-round tubes	[redacted]	[redacted]	[redacted]
3.1	Finalize design of 3-5 kW HXs	Regular	M3.1	• Non-round tube HXs optimized • Design(s) approved by industry partners on manufacturability & heat transfer performance

3.2	Fabricate HXs developed in M3.1	Regular	M3.2	• HX prototype(s) fabricated & delivered
3.3	HX test facility preparation completed	Regular	M3.3	• HX test facility preparation completed / Sensors calibrated / Ready for HX-level testing
		G / NG	G/NG #2	• In-house HX tests (stress / heat transfer / pressure drop / charge reduction) finalized • Deliver set of in-house validated HX prototypes for independent validation
4	Design, fabricate, & test HX prototypes for 3-ton systems & validate systems			
4.1	Industrial review feedback summary	Regular	M4.1	• Summary on industrial comments re: Y2 prototype independent testing on non-round tube HXs
4.2	Finalize design & fabrication of 3-ton HXs	Regular	M4.2	• 3-ton HXs optimized, designed, & fabricated
4.3	System-level perf. Measurement & charge reduction evaluation	Regular	M4.3	• System-level energy efficiency targets met • System charge reduction goals achieved
4.4	Final report	Regular	M4.4	• Report submitted to DOE

Project Results and Discussion

Heat Exchanger Analysis, Modeling, & Optimization (M2.1-2.5, M3.1, M4.2-4.3)

The modeling efforts for this project are listed below. A detailed report on each effort is included in the following section.

- (M2.1-M2.4) Development of an integrated multi-physics optimization framework for novel, non-round, finless, tube bundles. The physics of interest include: (i) Airside thermal-hydraulic performance; (ii) Aeroacoustics; (iii) Tube-level mechanical performance; (iv) Single-phase internal flow thermal-hydraulic performance; (v) Dehumidification; (vi) Fatigue analysis of tubes, headers, and tube-header joints.
- (M2.5, G/NG#1, M3.1, M4.2) Optimization of non-round tube bundles which are 20% lighter, 15% improved performance, & 40% tube-level charge reduction compared to a selected baseline HX (M2.1).
- (M4.3) System-level simulations and validation of system energy efficiency and charge reduction potential (details in the next section).

Integrated Multi-Physics Optimization Framework (M2.2-2.3)

Note: The contents of this section have been published in the following citations: Tancabel [4]*; Tancabel et al.,* [3]*; Tancabel et al.,* [136]*; Tancabel et al.,* [137].

Previous HX optimization frameworks [16], [30] consider only airside thermal-hydraulic performance (i.e., airside heat transfer coefficient and pressure drop) and do not include other important HX design considerations such as HX tube structural strength, tube bundle aeroacoustics noise generation, and tube-side thermal-hydraulic performance.

This work presents the development of an HX framework featuring multi-scale and multi-physics analyses and tube-level shape and topology optimization. This is accomplished through the development and integration of three new multi-physics models and the development of computationally-efficient correlations for accurate predictions thereof:

- aeroacoustics noise generation modeling to ensure that any noise resulting from turbulent cross-flow of air over the HX tube bundles are within acceptable levels;
- tube-level mechanical modeling to predict maximum tube-level stress for generalized non-round tubes; and
- tube-side thermal-hydraulic performance modeling to provide a complete thermal-hydraulic characterization of generalized tube shapes for use in future HX applications.

The optimization framework presented herein represents the novel, non-round tube shapes using fourth-order Non-Uniform Rational B-Splines (NURBS) [138]. In the context of this work, a HX which utilizes such tubes is termed a “NURBS Tube Heat Exchanger”, which is abbreviated “NTHX”.

Heat Exchanger Design & Optimization Methodology

The optimization framework (Figure 2) utilizes Approximation-Assisted Optimization (AAO) [20] involving automated Computational Fluid Dynamics (CFD) [30] and Finite

Element Analysis (FEA) simulations, Kriging metamodeling [139], and optimization with a Multi-Objective Genetic Algorithm (MOGA) [19].

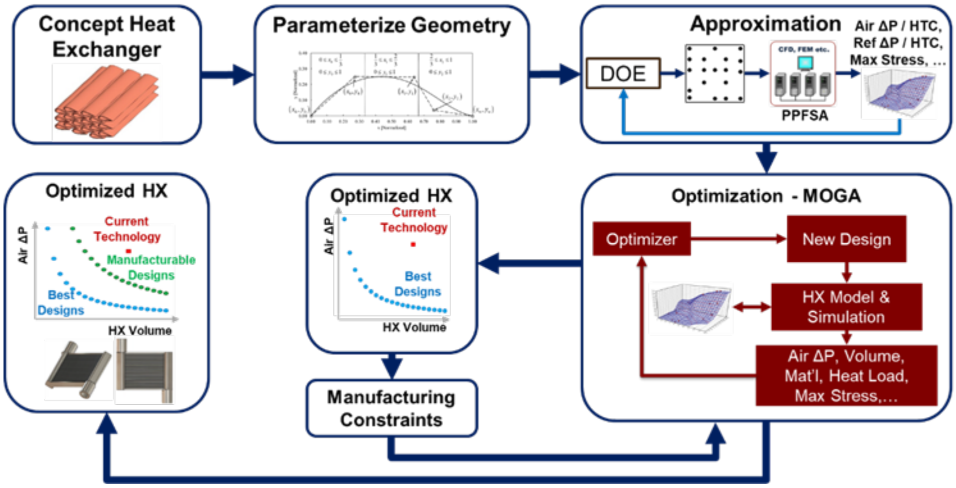

Figure 2: Numerical optimization framework.

Problem Description

This research considers air-to-fluid HXs in cross-flow where all HX models assume: (i) uniform normal inlet air velocity on the HX face and (ii) fully-developed uniform internal fluid (e.g., refrigerant) flow. Airside thermal-hydraulic performance is predicted using CFD, while tube-level mechanical performance can be computed using FEA. Refrigerant-side thermal-hydraulic performance is calculated using existing correlations for single- and two-phase flow in small channels. The framework is sufficiently general and is capable of designing single and two-phase HXs (i.e., radiators, condensers, and evaporators) for any refrigerant choice and/or operating requirements with significant engineering time savings compared to conventional design practices which can outperform the existing state-of-the-art HXs. Generalized schematics for a finless HX with shape-optimized tubes and a representative multi-pass tube-fin HXs are shown in Figure 3.

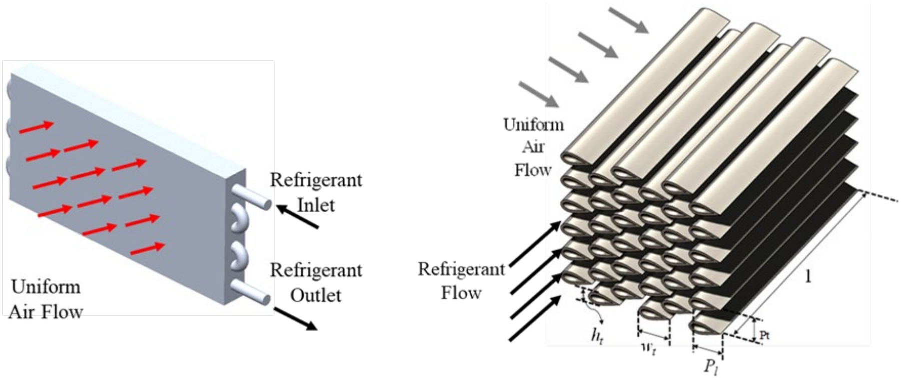

Figure 3: (Left) Generic multi-pass tube-fin HX; (Right) Generic HX with shape-optimized tubes.

The design space consists of 15 design variables which are listed in Table 10. The design variable definitions can be visualized on the sample HX depth-wise cross-section schematic shown in Figure 4. The fluid pass configuration can be visualized as shown in Figure 5.

Table 10: Non-round tube HX design variables.

Variable Type	Design Variable	Description
Scaling	h_t w_t / h_t N_t N_r	Tube height Tube aspect ratio Number of tube banks Number of tubes per bank
Topology	P_t / h_t P_l / w_t	Transverse pitch to tube height ratio Longitudinal pitch to tube width ratio
Shape	x_i (i =1,2,3) y_i (i =1,2,3)	Control point x-coordinate Control point y-coordinate
Fluid	u	Air velocity
Pass Configuration	γ λ	Percentage of tubes in first fluid pass Percentage of remaining tubes in second fluid pass

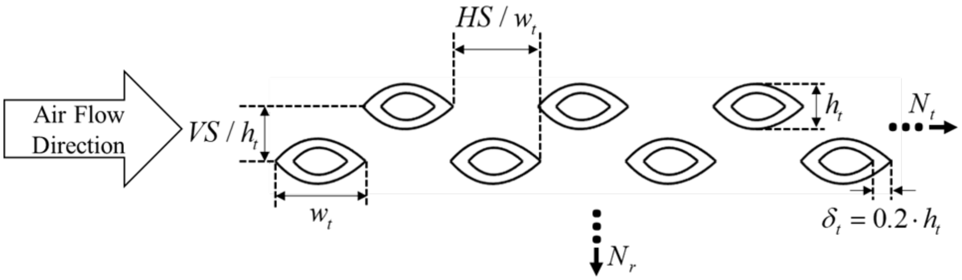

Figure 4: HX depth wise cross-section: Design variable definitions for non-round tubes.

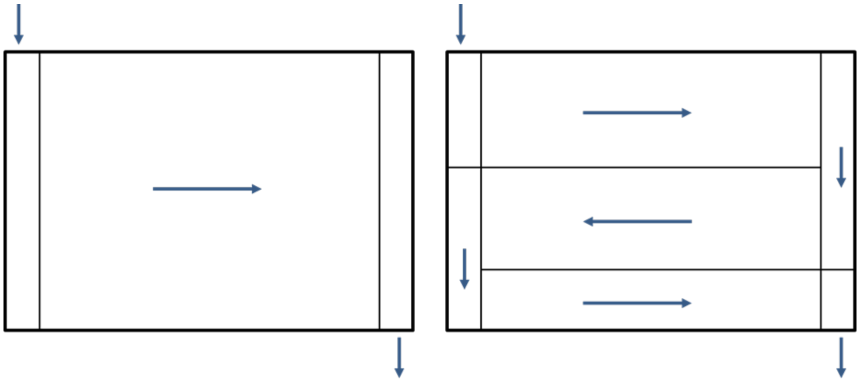

Figure 5: HX pass configuration definition: (left) one fluid pass; (right) three fluid passes.

Tube Shape Parameterization

The HX tube shapes are represented mathematically by fourth-order Non-Uniform Rational B-Splines (NURBS) as defined in Equation (1) [138]. All control point coordinates are normalized between 0 and 1. The leading-edge (le) and trailing-edge (te) points are fixed at (0,0) and (1,0), respectively. The coordinates of the three middle control points serve as the shape design variables. To prevent the curves from self-intersecting, the control point x-coordinates are bounded to equally spaced sections of the domain. A sample tube shape parametrization is presented in Figure 6.

$$C(u_s)=\sum_{i=0}^{4} R_{i,4}\left(u_s\right)\vec{x}_i;\quad R_{i,4}\equiv \text{Basis function};\quad \vec{x}_i\equiv \text{Control Points } (i=1,2,3);\quad 0\le u_s\le 1. \tag{1}$$

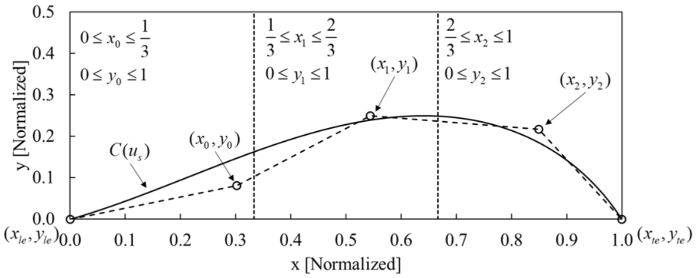

Figure 6: Tube shape parameterization using NURBS.

Parallel Parameterized Fluid & Structural Analysis (PPFSA)

It is not feasible to manually simulate all samples from a full Design of Experiments (DoE) in CFD and FEA. Thus, for rapid evaluation of novel geometries, the processes of geometry generation, meshing, and simulation must be automated. Abdelaziz et al. [30] developed a methodology termed Parallel Parameterized CFD (PPCFD) which carries out CFD analyses automatically in batch mode. Following the same motivation, a new framework termed Parallel Parameterized Fluid & Structural Analysis (PPFSA) was developed in this research, which combines PPCFD with automated static structural FEA simulations, allowing for multi-physics analyses on HXs with any tube shape. The flow chart for the automated structural analysis simulations is presented in Figure 7.

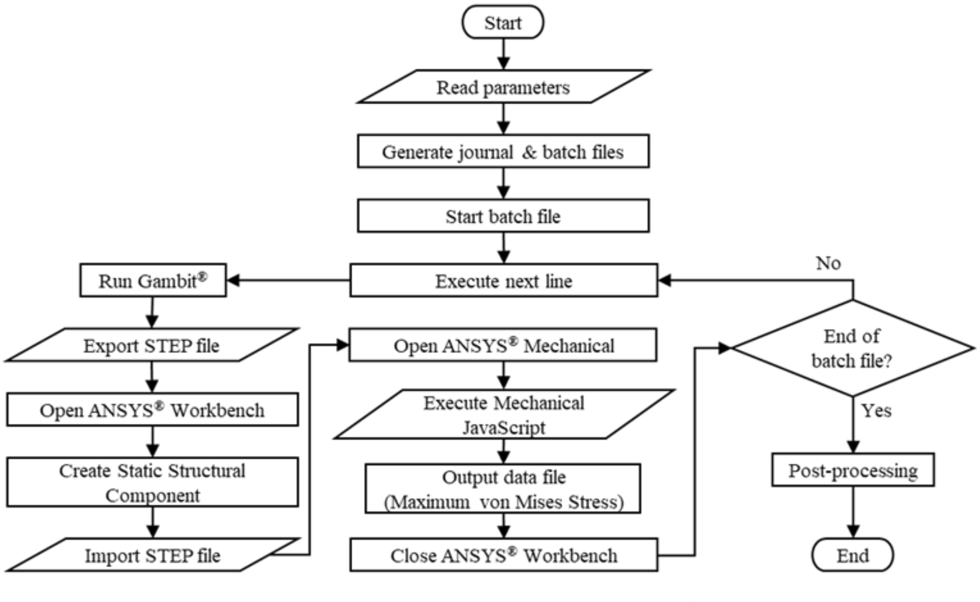

Figure 7: Automated FEA simulation flowchart.

Conventionally, the geometry and mesh generation steps are performed manually and are the most time-consuming steps in the process. In this methodology, these steps are automated by a computer program which reads input geometry parameters and generates batch and journal files for geometry creation, model meshing, running the simulations, and exporting results. The PPFSA tool is free from user intervention and generates the desired output of interest (here, maximum von Mises stress) for a given set of inputs in a computationally efficient manner.

Airside CFD Modeling

In this work, the airside CFD modeling is conducted using the ANSYS® platform. Geometry and meshing are performed using ANSYS® Gambit® 2.4.6 [140] and simulations are conducted using ANSYS® Fluent 19.3 [141]. Gambit® allows for efficient scripting and journaling for geometry and mesh formation, and is thus suitable for the automation method described herein.

Dry Air Thermal-Hydraulic Performance Modeling

Full HX performance simulations require fast and accurate predictions of the airside thermal-hydraulic performance, i.e., heat transfer coefficient (h) and pressure drop (ΔP). In this section, the CFD modeling methodology for dry air thermal-hydraulic performance is presented in detail.

The CFD computational domain (Figure 8) is a two-dimensional cross-section of the HX in the depth-wise direction. All end effects are ignored. An inflation layer mesh with growth ratio of 1.2 is employed in the near-wall region, while the core mesh is a pave scheme with average element size equal to the last row of the inflation layer. The left boundary is a uniform temperature and velocity inlet, while the right boundary is a constant atmospheric pressure outlet. Tube walls are kept at constant temperature higher than the inlet fluid temperature, and the upper and lower domain boundaries are periodic. Fluid properties for dry air are computed as polynomial curve fits of temperature except for density, which is computed using the ideal gas law. Turbulence is computed with the realizable k-ε (RKE) model [142]. The convergence criteria are set to maximum residuals of 1E-05 for continuity and momentum, 1E-06 for energy, and 1E-03 for turbulence. If the above criteria are not met, but the simulation stabilizes, the simulation is considered converged if the standard deviation of the final 100 iterations is less than 0.5% of the average of those 100 iterations.

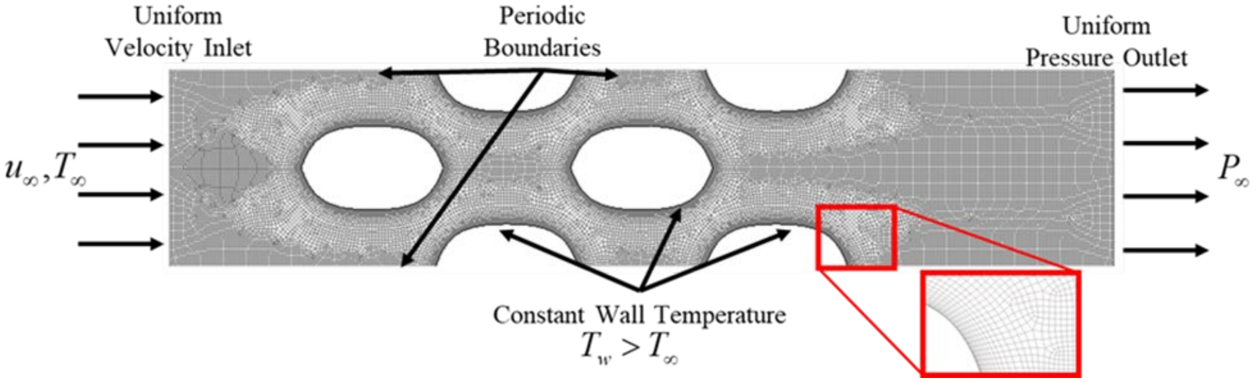

Figure 8: CFD domain, mesh, and boundary conditions.

The objective of the CFD simulations is to determine the airside thermal-hydraulic performance. Thus, it is unnecessary to consider the thermal resistances of the wall or refrigerant. Thus, the UA-Log Mean Temperature Difference (UA-LMTD) method can be used to compute airside heat transfer coefficient (Equation (2)) [143]. The airside pressure drop is taken as the difference in the inlet and outlet static pressure (Equation (3)).

$$h_{air} = \frac{\dot{m}_{air} c_{p,air}}{A_w} \cdot \ln\left[\frac{T_{air,w} - T_{air,in}}{T_{air,w} - T_{air,out}}\right], \tag{2}$$

$$\Delta P_{air} = P_{air,in} - P_{air,out}. \tag{3}$$

CFD modeling uncertainty due to grid resolution is quantified using the Grid Convergence Index (GCI) [144]–[147] for all boundary designs using three grid resolutions with a constant refinement ratio of 1.3. The GCI is computed using the absolute relative difference of a given metric (here, h, ΔP_{air}) between two grid sizes [144]–[147]. The results of the CFD uncertainty quantification are summarized in Table 11.

Table 11: CFD uncertainty quantification.

Metric	h_{air}	ΔP_{air}
Designs with GCI ≤ 10%	96%	91%
Worst-case GCI	16.5%	54.6%
Average	0.9%	1.2%
Median	2.0%	3.3%

Conducting a new CFD simulation for each individual generated by an optimizer during an optimization run would require tens of thousands (or more) of CFD simulations, which, depending on the complexity of the problem and geometry, could be extremely computationally infeasible. To reduce this computational burden, this research employs approximation-assisted optimization [20], wherein a simplified model capable of accurately representing the simulation behavior is utilized during to carry out the optimization. This simplified model is often referred to as a surrogate model or metamodel. In this case, metamodels are utilized to quickly and efficiently compute the airside thermal-hydraulic performance rather than running new CFD simulations for each case. The chosen metamodeling technique was Kriging, which originated from the field of geostatistics [139], [148]–[150] and has been shown to be highly flexible and suitable for predicting the responses from deterministic computer simulations, especially when utilizing fewer than 50 input variables [20].

The design variables of interest for the airside thermal-hydraulic performance include all variables from Table 10 except for number of tubes per bank (N_r) and fluid pass variables (γ, ζ), which are not required for this stage of the analysis. A DoE comprising 5000 samples was obtained using Latin Hypercube Sampling (LHS) [151] and simulated using PPFSA. Metamodels of thermal-hydraulic (airside h, ΔP) performance were developed using Kriging [139] (correlation: Gaussian; regression: 2nd order polynomial) using 2673 converged samples. The metamodels were verified by comparing metamodel responses to the results of CFD simulations for 544 converged random samples. Metamodel accuracy was measured using the Metamodel Acceptance Score (MAS) [152], which gives the percentage of predicted responses whose absolute relative error versus the simulated response which are below an established threshold. The metamodel verification results and summary statistics for the dry air thermal-hydraulic performance metamodels are shown in Figure 9. In general, the outliers are associated with points near the edges of the design space (i.e., extreme values of a combination of design variables), which can result in poor mesh quality and thus poor CFD model predictions.

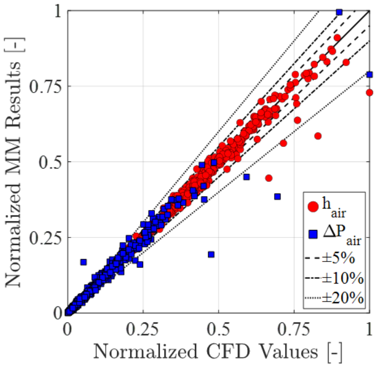

Metric	**h_{air}**	**ΔP_{air}**
[-]	[W/m^2K]	[Pa]
Mean Absolute Error	6.30	14.27
Root Mean Square Error	13.51	41.70
MAS (e_{th} = 10%)	97.97%	70.95%
MAS (e_{th} = 20%)	99.26%	90.99%

Figure 9: Dry air thermal-hydraulic performance metamodel verification & statistics.

Aeroacoustics Performance Modeling

The airside CFD computational domain (Figure 10) is a steady-state, two-dimensional cross-section of the HX in the depth-wise direction where all end effects are ignored and the working fluid is dry air. The left boundary is a uniform velocity and temperature inlet, while the right boundary is a constant atmospheric pressure outlet. The tube wall boundary condition is adiabatic since heat transfer is not the main interest of this study. The upper and lower domain boundaries are also treated as adiabatic walls to mimic the top and bottom mounting plates of the HX package. Each tube bank includes five tubes (e.g., in, each of the three tube banks include five tube rows for a total of 15 tubes) to ensure that the aeroacoustics behavior in the center of the HX height is accurately modeled using as few tubes as possible to improve computational efficiency. The computational domain core mesh utilizes triangular elements (Figure 19) while an inflation layer mesh with a growth ratio of 1.2 is employed in the tube near-wall region to accurately capture the boundary layer physics. The mesh size in the HX core is constant and equal to the size of the last element in the inflation mesh. The dry air thermophysical properties are computed as polynomial curve fits of temperature except for density, which is computed using the ideal gas law. Turbulence is computed with the realizable k-ε (RKE) model [142]. The convergence criteria are set to maximum residuals of 1E-05 for continuity and momentum, 1E-06 for energy, and 1E-03 for turbulence. If these criteria are not met, but the simulation stabilizes, the simulation is considered converged if the standard deviation of the final 100 iterations is less than 0.5% of the average of those 100 iterations. All CFD simulations are conducted in an automated fashion using the newly-developed PPFSA framework.

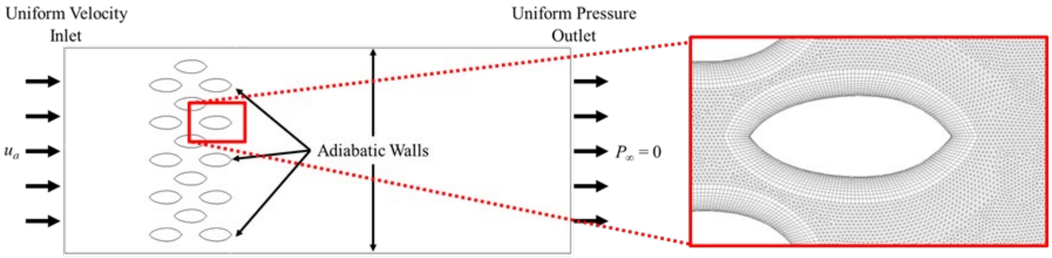

Figure 10: Aeroacoustics simulation CFD domain, boundary conditions, & mesh.

The objective of the CFD simulations is to determine the aeroacoustics-generated noise resulting from the turbulent air flow across the tube bundle. In such applications, it is often assumed that the noise does not have any distinct tones, i.e., the generated sound is broadband noise, which can be readily and inexpensively computed from statistical turbulence quantities such as the mean velocity field ($\bar{u}$), turbulent kinetic energy (k), and turbulent dissipation rate (ε), using the Ansys® Fluent Broadband Noise Source Model [141], [153] and the equations of Proudman [154] and Lilley [155] (Equation (4)). The metric of interest is acoustic power (AP), i.e., the intensity of the aeroacoustics-generated noise, which is measured in decibels (Db). As above, the CFD grid convergence errors were quantified using the GCI methodology [144]–[147], and the results are summarized in Table 12.

$$P_A = 0.1 \cdot \rho_0 \varepsilon \cdot \left(\frac{\sqrt{2k}}{a_0} \right)^5; \quad AP = 10 \cdot \log_{10} \left[\frac{P_A}{P_{reference}} \right]; \quad P_{reference} = 1.0\text{E}-12\ \text{W/m}^3. \tag{4}$$

Table 12: CFD grid uncertainty quantification for aeroacoustics simulations.

Metric	***AP***
Designs with GCI ≤ 10%	94%
GCI (Worst-case)	17.6%
Average	2.0%
Median	0.60%

The design variables of interest for the airside thermal-hydraulic performance include all variables from Table 10 except for number of tubes per bank (N_r) and fluid pass variables (γ, ζ), which are not required for this stage of the analysis. A 1000-sample DoE was generated using Latin Hypercube Sampling (LHS) [308] and simulated using PPFSA. A total of 947 converged samples were utilized to fit a Kriging metamodel [295] using a Gaussian correlation function and second order polynomial regression function. The correlations were verified by comparing metamodel responses to the results of CFD simulations for 237 random samples. The verification results for the dry air aeroacoustics performance metamodels are summarized in Figure 11.

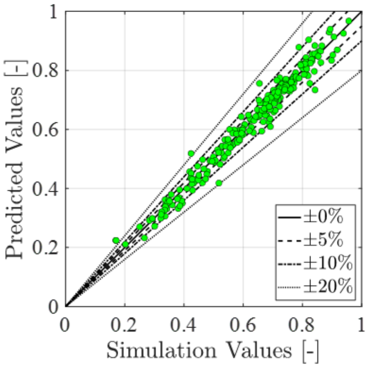

Metric	Value
Mean Absolute Relative Difference	3.6%
Median Absolute Relative Difference	32.3%
Relative RMSE	5.60%
Predicted data (±5%)	76.0%
Predicted data (±10%)	94.1%
Predicted data (±15%)	97.9%
Predicted data (±20%)	98.7%

Figure 11: Aeroacoustics performance correlation verification & statistics.

Mechanical Modeling of HX Tubes

To avoid the large computational effort associated with solving 3D FEA models, the PPFSA framework utilizes 2D FEA models as a representation of the full tube mechanical behavior. This simplification can be made by applying the plane strain assumption since the tube length is orders of magnitude larger than the tube height and width [156], [157]. This assumption will be verified later in this section.

Tube Mechanical Performance FEA Model

A sample 2D model is presented in Figure 12. The model is a plane strain cross-section of a single tube geometry. The mesh is a structured quad mesh with constant element edge length. A uniform static pressure of a user-defined magnitude is applied along the refrigerant flow channel edge. Previous experience with non-round tubes has shown that the critical point is located along the horizontal axis at the refrigerant channel location with minimum tube membrane thickness. Thus, a free x-displacement, fixed y-displacement support is applied at location with smaller membrane thickness (leftmost point in Figure 12). A fixed support is applied at the location with larger membrane thickness (rightmost point in Figure 12). These boundary conditions allow the tube to deform as it would during burst pressure testing. Moreover, the boundary conditions do not prevent the tube from failing elsewhere along the refrigerant channel. However, it should be noted that the critical locations are typically the x-axis points at the extreme of the refrigerant flow channel.

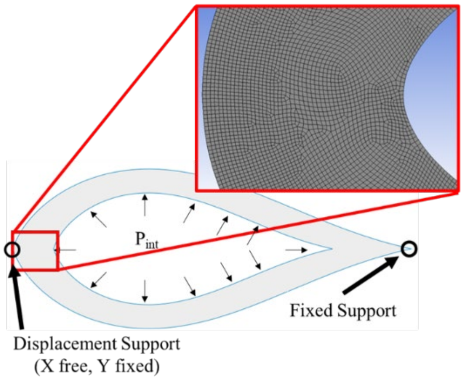

Figure 12: Two-dimensional FEA model, boundary conditions, and mesh.

The objective of the FEA simulations is to evaluate the tube-level mechanical performance. Thus, the metric of interest is the maximum von Mises stress (Equation (5)) [156], [157] occurring in on the tube cross-section, which can be utilized to select an appropriate tube material for the chosen application. A sample contour of maximum von Mises stress for a generic non-round tube is shown in Figure 13.

$$\sigma_{VM} = \sqrt{\frac{1}{2}\left[\left(\sigma_{xx}-\sigma_{yy}\right)^2+\left(\sigma_{yy}-\sigma_{zz}\right)^2+\left(\sigma_{zz}-\sigma_{xx}\right)^2+6\cdot\left(\sigma_{xy}^2+\sigma_{yz}^2+\sigma_{zx}^2\right)\right]}. \tag{5}$$

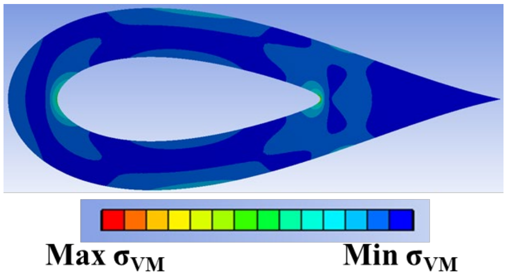

Figure 13: Sample FEA model contours of von Mises stress.

Plain Strain Verification & Modeling Uncertainty

<u>Certain aspects of the technologies or methodologies described in this section may be the subject of one or more patent applications and/or issued patents, including U.S. Patent App. No. 17/196,894, now published as U.S. Patent Pub. No. 2021/0285727.</u>

The plane strain assumption was verified by comparing the results of 2D FEA simulations with 3D FEA simulations of a full tube geometry for four tube shapes [44]. The 2D and 3D FEA models and boundary conditions are shown in Figure 14. The verification results are summarized in Table 13. The maximum error between 2D and 3D FEA models is less than 2.0%, which is well within acceptable ranges given the significant reduction in problem complexity associated with reducing the problem from 3D to 2D. The FEA model grid uncertainty was quantified using GCI for all four tube shapes [96], and the results are summarized in Table 14.

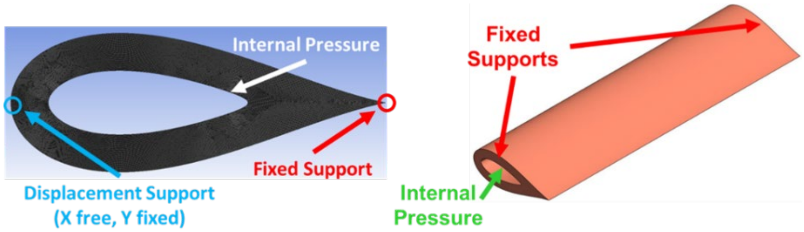

Figure 14: Boundary conditions for FEA simulations: (left) 2D and (right) 3D.

Table 13: Verification of plane strain assumption.

Geometry	Internal Pressure	Maximum σ_{VM} (2D)	Maximum σ_{VM} (3D)	Percent Difference

[-]	[MPa]	[MPa]	[MPa]	[-]
Geom-01	6.00	310.20	310.0	+0.06%
Geom-02	6.00	82.17	81.3	+1.08%
Geom-03	6.00	65.20	65.0	+0.31%
Geom-04	6.00	26.84	27.0	-0.60%

Table 14: FEA uncertainty quantification.

Metric	**σ_{VM}**
Designs with GCI ≤ 10%	100%
GCI (Worst-case)	6.2%
Average	2.8%
Median	2.6%

Metamodel Development & Verification

The eight (8) design variables of interest for tube-level mechanical performance are those listed in Table 10 which control tube size and shape only. Since all tubes in a given bundle are identical, it is only required to consider a single tube. Additionally, the structural strength modeling does not consider any fluid flow aspects. Thus, it is not necessary to consider the number of tubes, tube pitches, or fluid (air velocity, fluid pass configuration) variables from the complete NTHX design space (Table 10) for the mechanical modeling. A DoE comprising 5000 samples was generated using Latin Hypercube Sampling (LHS) [151] and was simulated using PPFSA. Kriging metamodels [139] of tube-level mechanical performance metamodels was developed using 4810 converged samples. The metamodels were verified by comparing metamodel responses to the results of FEA simulations for 956 converged samples for tube-level mechanical performance (i.e., σ_{VM}). Metamodel accuracy was measured using the Metamodel Acceptance Score (MAS) [152], which gives the percentage of predicted responses whose absolute relative error versus the simulated response which are below an established threshold. The metamodel verification results are summarized in Figure 15.

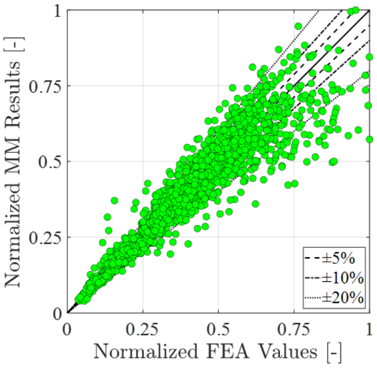

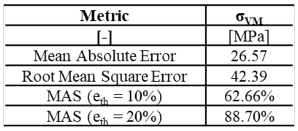

Metric	**σ_{VM}**
[-]	[MPa]
Mean Absolute Error	26.57
Root Mean Square Error	42.39
MAS ($e_{th} = 10\%$)	62.66%
MAS ($e_{th} = 20\%$)	88.70%

Figure 15: Tube-level mechanical performance metamodel verification & statistics.

Internal Flow CFD Modeling

A full assessment of the multi-physics performance of small diameter, non-round tubes would include a determination of the refrigerant-side (i.e., internal flow, pipe flow) thermal-hydraulic performance. Thus, it is of interest to utilize CFD to fully characterize the internal flow for small diameter, non-round, shape-optimized tubes. Single-phase internal flow CFD modeling was implemented into the PPFSA framework to introduce another multi-physics analysis for the design and optimization of HX utilizing non-round, shape-optimized tubes. In this work, the internal flow CFD modeling is conducted using the ANSYS® platform. Geometry and meshing are performed using ANSYS® Gambit® 2.4.6 [140] and simulations are conducted using ANSYS® Fluent 21.2 [158].

CFD Model, Data Reduction, & Modeling Uncertainty

The internal flow CFD model (Figure 16) utilizes a three-dimensional computational domain of the internal channel geometry where the mesh is an all-quadrilateral pave mesh scheme. An inflation layer mesh with a growth ratio of 1.2 is employed in the near-wall region to accurately capture the boundary-layer physics. The core mesh is a pave scheme with average element size equal to the last row of the inflation layer mesh. A uniform velocity inlet condition is applied to the leftmost boundary while the rightmost boundary is an atmospheric pressure outlet. The tube walls are set to a constant surface temperature, a case for which analytical solutions exist for a variety of tube shapes under laminar flow conditions [143]. The convergence criteria are set to maximum residuals of 1E-05 for continuity and momentum, 1E-06 for energy, and 1E-03 for turbulence. If these criteria are not met, but the simulation stabilizes, the simulation is considered converged if the standard deviation of the final 100 iterations is less than 0.5% of the average of those 100 iterations.

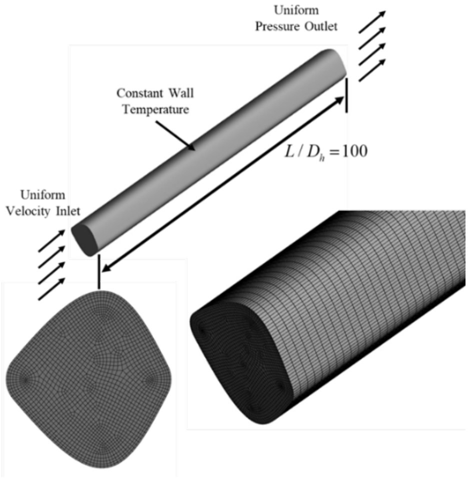

Figure 16: Internal flow computational domain, boundary conditions, & sample mesh.

The heat transfer coefficient is a function of flow regime only, and thus all other thermal resistances (i.e., airside, tube wall, etc.) can be neglected. The Nusselt number (dimensionless heat transfer) can be computed using the UA-LMTD method as in Equation (6) [143]. The friction factor (dimensionless pressure drop) can be computed as in Equation (7). For internal flow simulations, the domain must be long enough to ensure a sufficiently long portion of the tube experiences fully-developed flow. In this analysis, the tube length is set to be 100 times the hydraulic diameter. As above, the internal flow CFD grid uncertainty was quantified using the GCI methodology [144]–[147] for 67 total designs, and the results are summarized in Table 15.

$$Nu = \frac{h \cdot D_{h,in}}{k_{in}} = \frac{D_{h,in}}{k_{in}} \cdot \left[\frac{\dot{m} c_{p,in}}{A_w} \cdot \Delta T_{LMTD} \right], \tag{6}$$

$$f = 8 \cdot \frac{A_{CS}}{A_w} \cdot \frac{\Delta P - \left[\rho_{out} {u_{out}}^2 - \rho_{in} u_{in}^2 \right]}{\frac{1}{2} \rho_{T_{avg}} {u_{avg}}^2}. \tag{7}$$

Table 15: Internal flow thermal-hydraulic performance CFD uncertainty quantification.

Metric	Nu	f
Designs with GCI ≤ 10%	96%	91%
GCI (Worst-case)	16.5%	54.6%
Average	0.9%	1.2%
Median	2.0%	3.3%

Correlation Development Framework

The objective of this analysis is to develop CFD-based correlations for single-phase tube-side thermal-hydraulic performance. The thirteen (13) internal flow CFD modeling design variables utilized for PPFSA are as follows: (i) tube height (see Table 10); (ii) tube aspect ratio (see Table 10); (iii-viii) tube shape variables (see Table 10); (ix) tube thickness; (x) inlet Reynolds number; (xi) inlet fluid temperature; (xii) difference between inlet and wall temperatures; and (xiii) heating/cooling switch (allows for investigating cases where the fluid is being either heated or cooled). For each case, the absolute difference between the wall and the fluid inlet ranges between 5.0 K and 30.0 K. This allows for correlations to be developed considering a variable Prandtl number, which is a key dimensionless number often utilized in conventional internal flow heat transfer correlations. A 175-sample DoE was generated using Latin Hypercube Sampling (LHS) [151] for the twelve (12) continuous variables, and this 175-sample DoE was applied to both the cooling and heating cases, and thus 350 total simulations were conducted using PPFSA. In total, 282 (out of 350) converged samples were utilized for correlation development, while 70 (out of 100) random samples were utilized for correlation verification. The new single phase, CFD-based internal flow thermal-hydraulic performance correlations (forms discussed in the sections below) were built using the post-processed CFD data using Matlab's built-in `fitnlm` function [159] to solve for all unknown coefficients and exponents. A flow chart of the correlation development and verification procedure is shown in Figure 17.

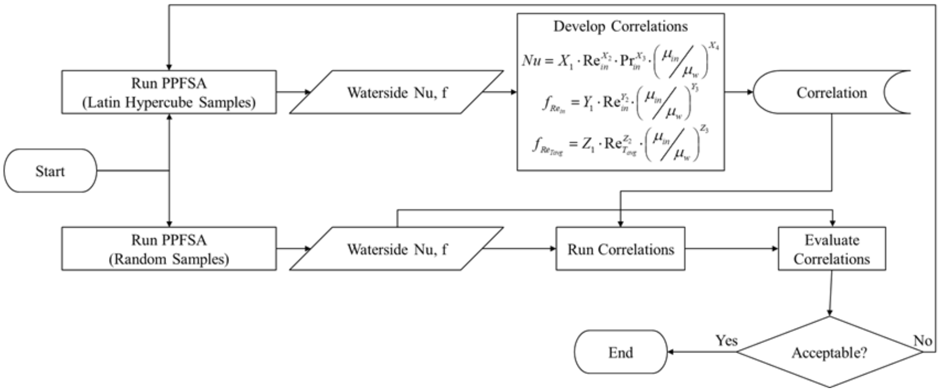

Figure 17: Internal flow correlation development framework.

Nusselt Number Correlation Development & Verification

One of the simplest and most common Nusselt number correlation forms is that of Dittus and Boelter [160] (Equation (8), “DB-form”), where the only indicator variables are the inlet Reynolds number (Re_{in}) and Prandtl number (Pr_{in}). A second common Nusselt number correlation form is that of Sieder and Tate [161] (Equation (9), “ST-form”), which includes a viscosity ratio correlation term to the Dittus-Boelter functional form to account for temperature changes between the bulk fluid and the heat transfer surface. The inlet Reynolds number is defined as Equation (10). The Nusselt number correlations were developed for two (inlet) Reynolds number ranges: (i) $100 \le Re_{in} \le 500$ and (ii) $500 < Re_{in} \le 2300$.

$$Nu_{DB-form} = X_1 \cdot \mathrm{Re}_{in}^{X_2} \cdot \mathrm{Pr}_{in}^{X_3}, \tag{8}$$

$$Nu_{ST-form} = Y_1 \cdot \mathrm{Re}_{in}^{Y_2} \cdot \mathrm{Pr}_{in}^{Y_3} \cdot \left(\frac{\mu_{in}}{\mu_w}\right)^{Y_4}, \tag{9}$$

$$\mathrm{Re}_{in} = \frac{\rho_{in} u_{in} D_{h,in}}{\mu_{in}}. \tag{10}$$

The CFD-based Nusselt number correlation coefficients are listed in Table 16, and the correlation verification with randomly-generated sample CFD data is summarized in Figure 18. It is clear that both correlation forms predict the CFD data very well (>90% of predictions agree within ±10%), but the ST-form correlation predicts a higher percentage of CFD data within ±5% compared to the DB-form (82.86% versus 68.57%). However, the ST-form correlation is implicit in nature since the wall temperature is required to compute the viscosity ratio correction term, and the implementation of such implicit calculations in segmented HX models (e.g., [162]) can lead to an unacceptable increase in total function calls and overall computational cost. Thus, the explicit nature of the DB-form correlation may be more attractive due to the correlation only relying on inlet conditions to compute the Nusselt number. Additionally, since the airside resistance often comprises more than 70-90% of the total resistance [163], [164], the marginal drop in correlation accuracy from the (implicit) ST-form to the (explicit) DB-form is expected to have a minimal impact on the overall HX performance predictions.

Table 16: CFD-based Nusselt number correlation coefficients & exponents.

DB-Form		
Coefficient	**$100 \leq Re_{in} \leq 500$**	**$500 < Re_{in} \leq 2300$**
X_1	1.2704	0.4084
X_2	0.1628	0.3152
X_3	0.2171	0.3477

ST-Form		
Coefficient	**$100 \leq Re_{in} \leq 500$**	**$500 < Re_{in} \leq 2300$**
Y_1	1.4186	0.4478
Y_2	0.1550	0.3128
Y_3	0.1657	0.2858
Y_4	0.1263	0.1444

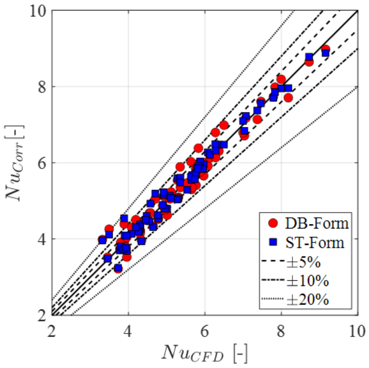

Metric	DB-Form	ST-Form
Mean Absolute Relative Difference	4.37%	3.44%
Maximum Absolute Relative Difference	21.86%	19.52%
% within ±5%	68.57%	82.86%
% within ±10%	91.43%	92.86%
% within ±15%	97.14%	95.71%
% within ±20%	97.14%	100%

Figure 18: CFD-based Nusselt number correlations verification and statistics.

Friction Factor Correlation Development & Verification

The inlet Reynolds number range considered herein corresponds to the classical theory laminar flow region (Re_{in} < 2300), where the friction factor is given as: f = C / Re_{in}. However, it is of interest to consider more generalized functional forms to achieve the highest possible accuracy. Moreover, because the fluid temperature, density, and viscosity change as the fluid flows, the Reynolds number can change along the tube length. To this end, a generalized power law functional form is considered (Equation (11) , "PL-form"), and additionally a power law equation form combined with a Sieder-Tate-like viscosity correction term (Equation (12), "PL-ST form"). Note that the following two equations consider the Reynolds number computer using the inlet conditions as defined as Equation (10). A second set of power law functional forms are considered for friction factor using a Reynolds number computed using the inlet velocity and fluid properties computed using the average fluid temperature (Re_{Tavg}, Equation (13), "average temperature Reynolds number") to account for fluid temperature changes along a given segment. The alternative power law functional forms utilizing the average temperature Reynolds number are listed in Equations (14) and (15). For each of the friction factor functional forms, CFD-based correlations were developed for the full tube, developing flow region, and fully developed flow region, resulting in 12 total correlations for friction factor. As with Nusselt number, two Reynolds number ranges are considered: (i) $100 \leq$ $Re \leq 500$ and (ii) $500 < Re \leq 2300$.

$$f_{in,PL} = C_1 \cdot \mathrm{Re}_{in}^{C_2}, \tag{11}$$

$$f_{in,PL-ST} = D_1 \cdot \mathrm{Re}_{in}^{D_2} \cdot \left(\frac{\mu_{in}}{\mu_w} \right)^{D_3}. \tag{12}$$

$$\mathrm{Re}_{T_{avg}} = \frac{\rho_{T_{avg}} u_{in} D_{h,in}}{\mu_{T_{avg}}}, \tag{13}$$

$$f_{T_{avg},PL} = A_1 \cdot \mathrm{Re}_{T_{avg}}^{A_2}, \tag{14}$$

$$f_{T_{avg},PL-ST} = B_1 \cdot \mathrm{Re}_{T_{avg}}^{B_2} \cdot \left(\frac{\mu_{in}}{\mu_w} \right)^{B_3}. \tag{15}$$

The CFD-based friction factor correlation coefficients are listed in Table 17 (PL-Form) and Table 18 (PLST-Form), and the correlation verification with randomly-generated sample CFD data is summarized in Figure 19 (full tube flow), Figure 20 (developing flow), and Figure 21. (fully developed flow). First, note that the average temperature Reynolds number (Re_{Tavg}) correlations are superior to the inlet Reynolds number (Re_{in}) correlations regardless of functional form. This is due to the Re_{Tavg} accounting for fluid property changes (with temperature) associated with simultaneous heat transfer and fluid flow. Second, the inlet Reynolds number PLST-form correlations are vastly superior to the inlet Reynolds number PL-form correlations, again due to the Sieder-Tate viscosity correction term accounting for fluid property changes that result from heat transfer. Finally, the PLST-form correlations and all correlations using Re_{Tavg} are implicit since the wall and/or outlet temperatures are required to compute the fluid properties, which comes with all potential challenges mentioned in the previous section (additional function calls and related higher computational costs). Nonetheless, the superior prediction accuracy of such correlations to the CFD test data suggests that such iterations might be unavoidable to enable sufficiently accurate thermal-hydraulic performance predictions.

Table 17: CFD-based friction factor PL-Form correlation coefficients & exponents.

Full Tube Flow (Re_{in})			**Full Tube Flow (Re_{Tavg})**		
Coefficient	$100 \leq \mathrm{Re}_{in} \leq 500$	$500 < \mathrm{Re}_{in} \leq 2300$	**Coefficient**	$100 \leq \mathrm{Re}_{Tavg} \leq 500$	$500 < \mathrm{Re}_{Tavg} \leq 2300$
A_1	137.9513	142.2223	A_1	179.7617	165.0870
A_2	-1.0677	-1.0675	A_2	-1.1199	-1.0911
Coefficient	$100 \leq \mathrm{Re}_{in} \leq 500$	$500 < \mathrm{Re}_{in} \leq 2300$	**Coefficient**	$100 \leq \mathrm{Re}_{Tavg} \leq 500$	$500 < \mathrm{Re}_{Tavg} \leq 2300$
Developing Flow Region (Re_{in})			**Developing Flow Region (Re_{Tavg})**		
Coefficient	$100 \leq \mathrm{Re}_{in} \leq 500$	$500 < \mathrm{Re}_{in} \leq 2300$	**Coefficient**	$100 \leq \mathrm{Re}_{Tavg} \leq 500$	$500 < \mathrm{Re}_{Tavg} \leq 2300$
A_1	216.1559	406.5179	A_1	236.0362	477.5477

A_2	-1.1000	-1.1975	A_2	-1.1158	-1.2208
Fully Developed Flow Region (Re$_{in}$)			**Fully Developed Flow Region (Re$_{Tavg}$)**		
Coefficient	$100 \leq \text{Re}_{in} \leq 500$	$500 < \text{Re}_{in} \leq 2300$	**Coefficient**	$100 \leq \text{Re}_{Tavg} \leq 500$	$500 < \text{Re}_{Tavg} \leq 2300$
A_1	163.6712	312.5771	A_1	210.8107	388.0267
A_2	-1.1084	-1.2081	A_2	-1.1597	-1.2406

Table 18: CFD-based friction factor PLST-Form correlation coefficients & exponents.

Full Tube Flow (Re$_{in}$)			**Full Tube Flow (Re$_{Tavg}$)**		
Coefficient	$100 \leq \text{Re}_{in} \leq 500$	$500 < \text{Re}_{in} \leq 2300$	**Coefficient**	$100 \leq \text{Re}_{Tavg} \leq 500$	$500 < \text{Re}_{Tavg} \leq 2300$
B_1	131.3526	116.8163	B_1	122.5628	121.0133
B_2	-1.0684	-1.0407	B_2	-1.0553	-1.0458
B_3	-0.7973	-0.5840	B_3	-0.3817	-0.3514
Coefficient	$100 \leq \text{Re}_{in} \leq 500$	$500 < \text{Re}_{in} \leq 2300$	**Coefficient**	$100 \leq \text{Re}_{Tavg} \leq 500$	$500 < \text{Re}_{Tavg} \leq 2300$
Developing Flow Region (Re$_{in}$)			**Developing Flow Region (Re$_{Tavg}$)**		
Coefficient	$100 \leq \text{Re}_{in} \leq 500$	$500 < \text{Re}_{in} \leq 2300$	**Coefficient**	$100 \leq \text{Re}_{Tavg} \leq 500$	$500 < \text{Re}_{Tavg} \leq 2300$
B_1	203.3600	330.5606	B_1	210.3549	339.4869
B_2	-1.0990	-1.1689	B_2	-1.1050	-1.1725
B_3	-0.8220	-0.6454	B_3	-0.7639	-0.5324
Fully Developed Flow Region (Re$_{in}$)			**Fully Developed Flow Region (Re$_{Tavg}$)**		
Coefficient	$100 \leq \text{Re}_{in} \leq 500$	$500 < \text{Re}_{in} \leq 2300$	**Coefficient**	$100 \leq \text{Re}_{Tavg} \leq 500$	$500 < \text{Re}_{Tavg} \leq 2300$
B_1	149.2435	252.4621	B_1	150.3050	317.0829
B_2	-1.1020	-1.1783	B_2	-1.1028	-1.2112
B_3	-0.9118	-0.7257	B_3	-0.3521	-0.2677

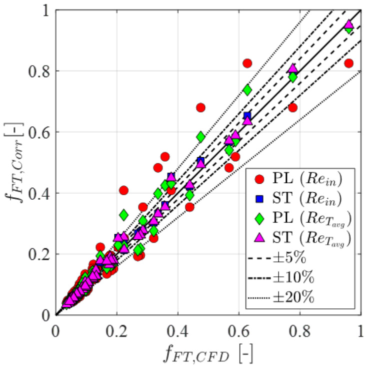

Metric	**PL-Form (Re$_{in}$)**	**PL-Form (Re$_{Tavg}$)**	**PLST-Form (Re$_{in}$)**	**PLST-Form (Re$_{Tavg}$)**
Mean Absolute Relative Difference	19.37%	10.90%	4.91%	4.56%
Maximum Absolute Relative Difference	83.64%	47.33%	24.40%	23.25%
% within ±5%	8.57%	25.71%	64.29%	71.43%
% within ±10%	27.14%	47.14%	90.00%	90.00%
% within ±15%	47.14%	74.29%	94.29%	95.71%
% within ±20%	61.43%	90.00%	97.14%	97.14%

Figure 19: CFD-based friction factor correlation (full tube flow) verification and statistics.

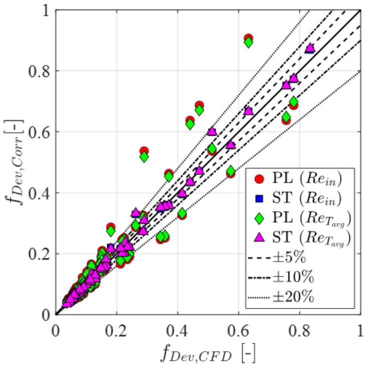

Metric	PL-Form (Re_{in})	PL-Form ($Re_{T_{avg}}$)	PLST-Form (Re_{in})	PLST-Form ($Re_{T_{avg}}$)
Mean Absolute Relative Difference	20.78%	17.23%	5.47%	5.61%
Maximum Absolute Relative Difference	85.28%	78.91%	25.50%	26.84%
% within ±5%	8.57%	8.57%	58.57%	60.00%
% within ±10%	15.71%	27.14%	90.00%	85.71%
% within ±15%	37.14%	55.71%	92.86%	92.86%
% within ±20%	55.71%	74.29%	95.71%	97.14%

Figure 20: CFD-based friction factor correlation (developing flow) verification and statistics.

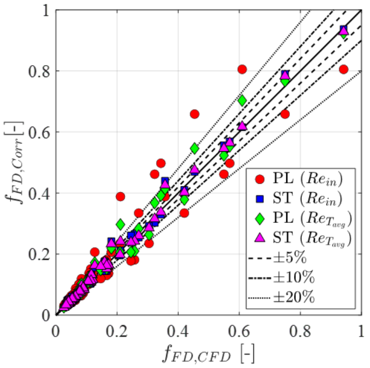

Metric	PL-Form (Re_{in})	PL-Form ($Re_{T_{avg}}$)	PLST-Form (Re_{in})	PLST-Form ($Re_{T_{avg}}$)
Mean Absolute Relative Difference	19.50%	8.07%	7.90%	6.19%
Maximum Absolute Relative Difference	83.97%	40.66%	33.54%	28.78%
% within ±5%	8.57%	47.14%	41.43%	58.57%
% within ±10%	18.57%	70.00%	70.00%	84.29%
% within ±15%	45.71%	84.29%	85.71%	92.86%
% within ±20%	60.00%	91.43%	91.43%	95.71%

Figure 21: CFD-based friction factor correlation (fully developed flow) verification and statistics.

Dehumidification Modeling of Generalized, Non-Round Tube Bundles

In HVAC&R systems, the evaporator coils (indoor unit during cooling mode operation) typically operate under dehumidifying (wet) conditions where the air temperature (sensible cooling) and humidity (latent cooling) are reduced. In the latter process, water vapor in the air condenses into droplets which can accumulate on the tube and fin surfaces, resulting in a complex simultaneous heat and mass transfer and phase change process. Modeling such phenomenon typically carries high degrees of uncertainty. Most existing dehumidification models assume a Lewis number (Equation (16)) of unity [165], even though experimental works in literature have reported Lewis numbers for large diameter ($\gtrapprox$7.0 mm) round tubes and various fin geometries such as plain fins [166]–[173], wavy fins [172], [174]–[178], louver fins [174], [175], [179], and lanced fins [174], [175] ranging from 0.1 – 1.62, suggesting that a unity Lewis number assumption is not always appropriate and thus limiting confidence in model prediction accuracy. In this work, we consider finless tube bundles with small diameter (< 5.0 mm), non-round, shape-optimized tubes to improve HX thermal-hydraulic performance in HVAC&R systems, and the dehumidification performance and Lewis number of such tube bundles has not been rigorously studied, further calling into question whether existing Lewis number relations and dehumidification model assumptions are applicable for novel heat transfer surfaces.

$$Le = \frac{h_s}{h_d c_{p,a}} \approx 1.0 \qquad (16)$$

Dehumidification Performance Modeling Methodology

The airside dehumidification modeling methodology (Figure 22) considers the sensible and latent heat loads separately. First, a steady-state, dry air CFD simulation is conducted in an automated fashion using ANSYS® Fluent 21.2 [158] to compute the sensible component (pressure, temperature, velocity). The dry air CFD solution is then loaded into ANSYS® FENSAP-ICE 21.2 [180], which simulates moist air dehumidification (latent component) utilizing the dry air velocity and temperature fields at a user-specified relative humidity. The moist air CFD simulations assume steady flow with no external forces, energy and/or mass sources, and the effects of pressure work, gravity, and kinetic energy are neglected. Additionally, the moist air simulations assume no condensate retention and carryover effects, i.e., any condensate is assumed to drain immediately from the tube surface and does not enter the downstream duct. The moist air CFD settings are as follows: (i) vapor particle model; (ii) initial relative humidity is defined as the inlet relative humidity; (iii) convergence criteria is 1E-15 or 50 iterations.

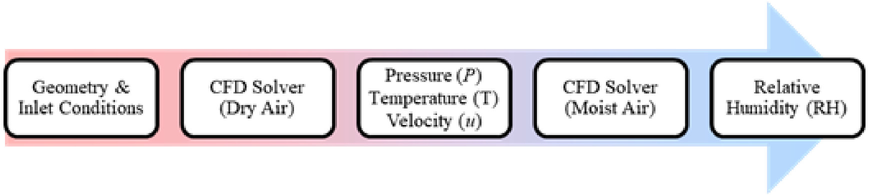

Figure 22: Dehumidification modeling methodology.

CFD Modeling, Simulation, & Data Reduction

The airside CFD computational domain (left image in Figure 23) is a steady-state, three-dimensional cross-section of the HX in the depth-wise direction. The three-dimensional domain is formed by extruding the two-dimensional CFD computational domain described above along the tube length direction by a distance equal to twice the tube hydraulic diameter. The inlet boundary (left face) is a uniform velocity, temperature, and relative humidity, while the outlet boundary (right face) is at constant atmospheric pressure. The tube walls are fixed to a temperature below the inlet air dew point temperature to ensure dehumidification will occur. The upper, lower, and lateral domain boundaries are no-slip, adiabatic, moving walls with a velocity equal to the inlet air velocity to emulate free-flow around the tube bundle. The computational domain mesh (right image in Figure 23) is a sweep of the (two-dimensional) lateral face mesh in the tube length direction. The lateral face is meshed as in the above discussion, and the element size in the tube length direction is equal that of the last element in the inflation mesh.

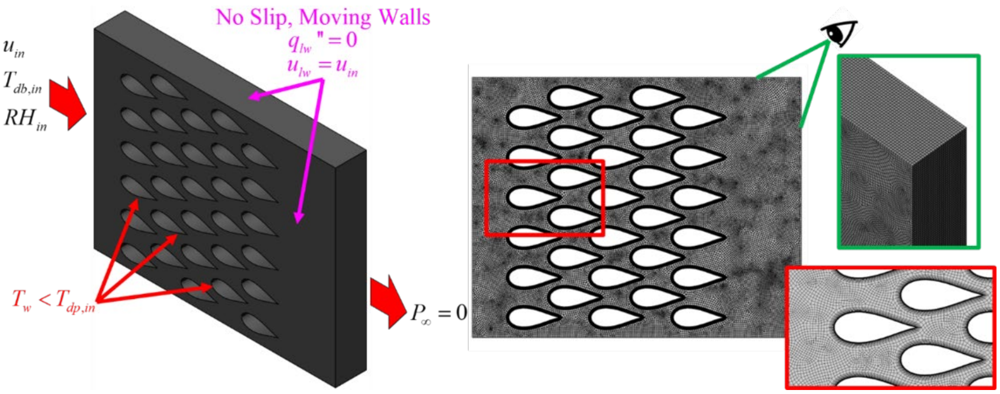

Figure 23: Dehumidification model: (Left) Sample domain & boundary conditions; (Right) Sample mesh.

The objective of the moist air CFD simulations is to determine the dehumidification performance, i.e., the Lewis number, of generalized, non-round tube bundles. In this work, the Lewis number is defined as in Equation (17), where h_s is the dry air sensible heat transfer coefficient, h_d is the mass transfer coefficient, and $c_{p,a}$ is the dry air thermal conductivity. The sensible heat transfer coefficient is computed using dry air CFD simulations or metamodel described above, while the thermal conductivity is can be computed using any appropriate fluid property evaluation method. The mass transfer coefficient can be computed using the heat-mass transfer analogy with the "U_sA-LMTD" method, i.e., the "U_dA-LMwD" method (U_dA-Log Mean Mass Fraction Difference method, Equation (18)) [143] where the mass transfer rate $(\dot{m}_w)$ is defined as in Equation (19) and the mass fraction of water vapor in air (w) is defined in terms of absolute humidity (ω) as in Equation (20). The absolute humidity can be computed using a fluid property evaluation since the temperature and relative humidity are both known quantities from the dry and moist air CFD simulations, respectively. Finally, the Reynolds number is defined using dry air fluid properties as in Equation (21).

$$Le = \frac{h_s}{h_d \cdot c_{p,a}\left(T_{db}\right)} \tag{17}$$

$$\dot{m}_w = h_d A_s \Delta w_{LM}; \quad \Delta w_{LM} = \frac{\left(w_w - w_{in}\right) - \left(w_w - w_{out}\right)}{\ln\left[\left(w_w - w_{in}\right)/\left(w_w - w_{out}\right)\right]} \tag{18}$$

$$\dot{m}_w = \dot{m}_a \cdot \left(w_{in} - w_{out}\right) \tag{19}$$

$$w = \frac{\omega\left(T_{db}, RH\right)}{\omega\left(T_{db}, RH\right) + 1} \tag{20}$$

$$\mathrm{Re}_{D_h} = \frac{\rho_a u_{in} D_h}{\mu_a} \qquad D_h = \frac{4 A_{min} D_{HX}}{A_s} \tag{21}$$

Experimental Validation

The dehumidification CFD model was validated using the 3-C1 (CNTHX) prototype (Figure 24) produced by Heat Transfer Technologies (HTT), which was tested under air-to-R410A evaporator conditions for eleven (11) steady-state points in accordance with

AHRI Standard 210/240 A-Test conditions [181]. The nominal experimental inlet conditions are also summarized in Figure 24. Additional details on experimental testing will be discussed in later sections.

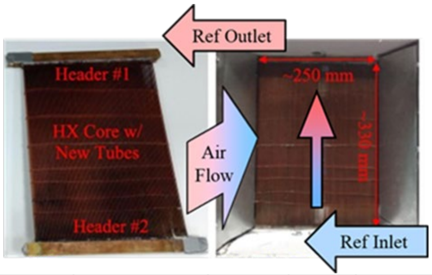

Inlet $T_{air,db}$	**Inlet RH**	**Inlet $T_{air,dp}$**	**Inlet Air Velocity**	**Inlet T_{ref}**	**Inlet x_{ref}**	**Refrigerant Flow Rate**	**Outlet Superheat**
[°C]	[%]	[°C]	[m/s]	[°C]	[-]	[g/s]	[K]
26.7	51	15.4	1.0 – 2.5	10.0	0.20	7.0 – 11.5	>8.0

Figure 24: CNTHX prototype.

Because the dehumidification CFD model considers the airside only, a (constant) wall temperature must be defined which accurately represents the refrigerant-side temperature. For heat and mass transfer applications, the logarithmic mean ("log-mean") temperature (Equation (22)) is appropriate for steady-state heat and mass transfer applications [143]. Additionally, the log-mean temperature can be directly calculated since the outlet refrigerant temperature is measured during experiments.

$$T_{LM} = \frac{T_{out} - T_{in}}{\ln\left[T_{out} / T_{in}\right]} \tag{22}$$

The experimental validation results are summarized in Figure 25 – Figure 27 and Table 19, where the metrics of interest are: (i) the outlet dry-bulb temperature ($T_{db,out}$, i.e., sensible heat transfer), (ii) relative humidity (RH_{out}), (iii) absolute humidity (ω_{out}), (iv) absolute humidity change ($\Delta\omega = \omega_{in} - \omega_{out}$, i.e., amount of dehumidification), and (v) sensible heat ratio (SHR = $Q_{sensible} / Q_{total}$), respectively. It is clear that the CFD model shows excellent agreement with experimental results for all metrics across all test conditions. While the errors for absolute humidity change seem large (maximum error: ~38.6%), it must be noted that the maximum latent capacity relative experimental uncertainty is 41.9%, and thus any agreement within this bound can be considered acceptable from a validation standpoint.

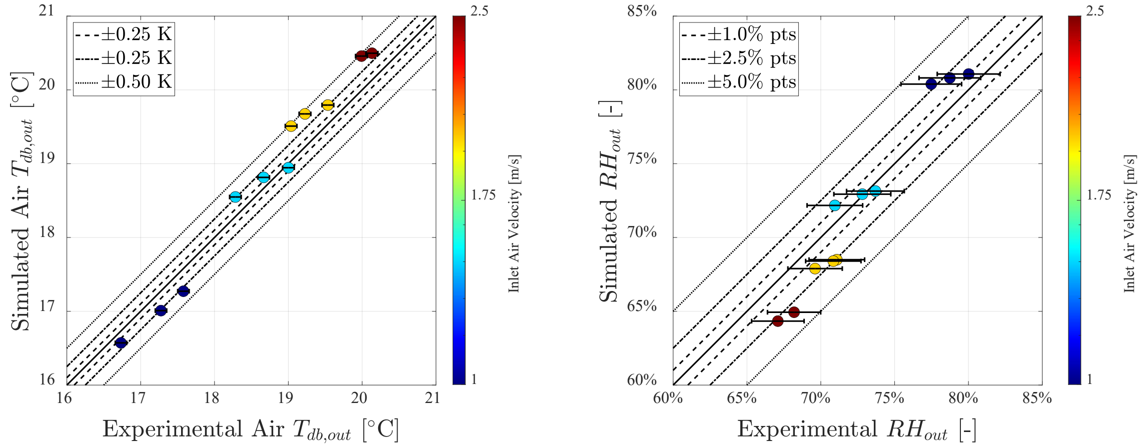

Figure 25: CNTHX experimental validation: (Left) Outlet dry bulb temperature; (Right) Outlet relative humidity.

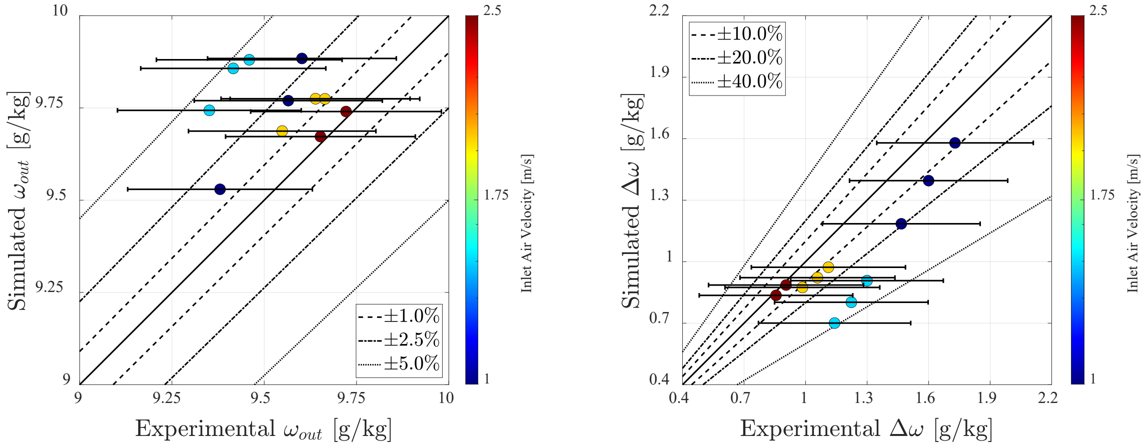

Figure 26: CNTHX dehumidification experimental validation: (Left) Outlet absolute humidity; (Right) Absolute humidity change.

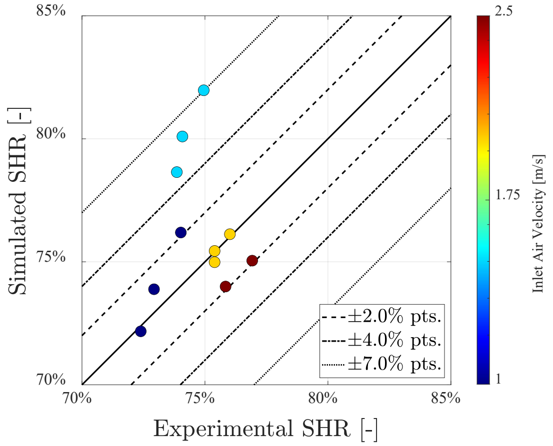

Figure 27: CNTHX dehumidification experimental validation: Sensible heat ratio.

Table 19: CNTHX dehumidification experimental validation statistics.

Metric	Error Type	Mean Error	Median Error	Maximum Error
Outlet $T_{air,db}$	Absolute	0.292 K	0.266 K	0.472 K
Outlet RH	Absolute	1.88% pts.	2.07% pts.	1.88% pts.
Outlet ω	Absolute Relative	2.22%	1.59%	4.68%
$\Delta\omega$	Absolute Relative	16.80%	12.79%	38.64%
SHR	Absolute	2.31% pts.	1.84% pts.	7.02% pts.

Parametric Study on the Impact of HX Inlet Conditions on Lewis Number

A parametric study was conducted to determine how Lewis number varies with changing inlet conditions. Three parametric variables are considered: (i) inlet air velocity (1.0 m/s, 2.0 m/s, 3.0 m/s), (ii) inlet relative humidity (40%, 51%, 70%), and (iii) inlet fluid-side “inlet” temperature (5°C, 10°C, 15°C), for a total of 27 cases. The inlet air dry bulb temperature is fixed to 26.7°C, which corresponds to the cooling mode indoor unit (i.e., evaporator) inlet dry bulb temperature from AHRI Standard 210/240 A-Test conditions [181]. The air velocities are chosen based on previous experience with residential HXs [96], while the inlet relative humidity values are chosen according to AHRI Standard 210/240 test conditions [181]. The tube wall temperature is the log-mean temperature (Equation (22)) of the measured fluid side temperatures. Since the CFD model does not consider internal fluid flow, the “inlet” temperature, i.e., the “refrigerant evaporating temperature”, is a parametric variable, while the fluid-side “outlet” temperature is computed by assuming a fixed outlet “superheat” of +5.0 K. If the computed tube wall temperature is greater than the inlet air dew point temperature, then the wall temperature is lowered by 7.0 K to ensure dehumidification.

The parametric study results are summarized in Figure 28. First, consider inlet air velocity (Reynolds number, top left in Figure 28) at fixed relative humidity (51%) and wall temperature (280.4 K). The relationship matches the expectation from literature [166]–[179], [182], i.e., Lewis number decreases with increasing air velocity, providing additional confidence in the modeling framework. This can also be explained by considering the sensible heat and mass transfer coefficients (top right in Figure 28). The mass transfer coefficient increases at a higher rate than the sensible heat transfer coefficient as air velocity increases, yielding lower Lewis number as air velocity increases.

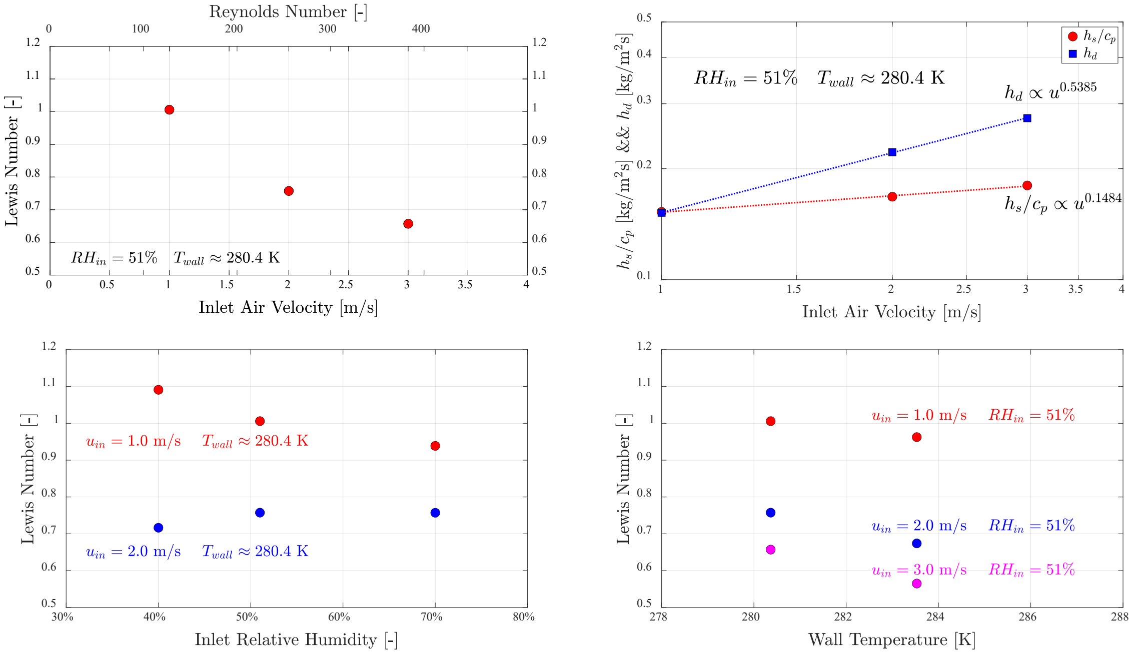

Figure 28: Lewis number parametric study results: (Top Left) Inlet air velocity (Reynolds number); (Top Right) Sensible heat transfer coefficient and mass transfer coefficient vs. inlet air velocity; (Bottom Left) Inlet relative humidity; (Bottom Right) Wall temperature.

Next, consider the impact of inlet relative humidity on Lewis number (bottom left in Figure 28) at fixed inlet air velocity (u_{in} = 2.0 m/s; Re = 255.4) and wall temperature (280.4 K). It can be seen that the Lewis number does not show much variation as inlet relative humidity changes (first increasing, then slightly decreasing). However, some correlations [7, 16] utilize inlet relative humidity (or similar air moisture content metrics) as a predictor variable for Lewis number to account for higher condensate removal rates at higher inlet relative humidity. This relation (Lewis number decreases as inlet relative humidity increases) can be seen in the low inlet air velocity case (u_{in} = 1.0 m/s; Re = 127.7), where the Lewis number monotonically decreases with increasing inlet relative humidity. This suggests that the Lewis number is more strongly related to inlet air velocity than inlet relative humidity, which agrees with previous literature [166]–[179], [182]. Finally, consider the impact of wall temperature on Lewis number (bottom right in Figure 28) at a fixed relative humidity (51%). For all inlet air velocities (uin = 1.0, 2.0, 3.0 m/s), the Lewis number decreases with increasing wall temperature, which agrees with previous literature [16]. This can also be explained by considering the sensible heat and mass transfer coefficients (top right in Figure 28). It is well known [143] that for a fixed geometry, the sensible heat transfer coefficient is independent of temperature potential, while, similarly, the mass transfer coefficient is independent of concentration potential. However, the concentration of water vapor in air is a (nonlinear) function of temperature, suggesting the existence of a relationship between mass transfer coefficient and temperature.

Lewis Number Correlation Development & Experimental Validation

CFD-based Lewis number correlations were built using the `fitnlm` and `stepwiselm` functions in Matlab [159]. Three correlations were built for the CNTHX tube bundle: (i) a power law function of Reynolds number only (Equation (23)), (ii) a power law function of

Reynolds number and inlet relative humidity (Equation (24)), and (iii) a linear regression determined by `stepwiselm` [159], where the base linear regression functional form is a log-transformed quadratic function of two variables (Reynolds number, inlet relative humidity) and is listed in Equation (25). For these correlations, the Reynolds number is defined as in Equation (21), while the inlet relative humidity (RH_{in}) is defined between the 0.0 – 100.0, e.g., 40% relative humidity is defined as RH_{in} = 40. The CFD-based Lewis number correlation coefficients are listed in and . The linear regression functional form determined by `stepwiselm` [159] is shown in Equation (26):

$$Le_{PL1} = A_1 \cdot \mathrm{Re}_{D_h}{}^{A_2} \tag{23}$$

$$Le_{PL2} = B_1 \cdot \mathrm{Re}_{D_h}{}^{B_2} \cdot RH_{in}{}^{B_3} \tag{24}$$

$$\ln\left(Le_{LR}\right) = \begin{pmatrix} C_1 + C_2 \cdot \ln\left(\mathrm{Re}_{D_h}\right) + C_3 \cdot \ln\left(RH_{in}\right) + C_4 \cdot \ln\left(\mathrm{Re}_{D_h}\right)^2 + \\ C_5 \cdot \ln\left(RH_{in}\right)^2 + C_6 \cdot \ln\left(\mathrm{Re}_{D_h}\right) \cdot \ln\left(RH_{in}\right) \end{pmatrix} \tag{25}$$

$$\ln\left(Le_{LR}\right) = C_1 + C_2 \cdot \ln\left(\mathrm{Re}_{D_h}\right) + C_3 \cdot \ln\left(RH_{in}\right) + C_6 \cdot \ln\left(\mathrm{Re}_{D_h}\right) \cdot \ln\left(RH_{in}\right) \tag{26}$$

Table 20: CFD-based Nusselt number correlation coefficients & exponents.

Power Law #1		**Power Law #2**	
Coefficient	**Value**	**Coefficient**	**Value**
A_1	7.9309	B_1	15.1747
A_2	-0.4273	B_2	-0.4244
-	-	B_3	-0.1675
Linear Regression			
Coefficient	**Value**	**Coefficient**	**Value**
C_1	9.4479	C_3	-1.8707
C_2	-1.7142	C_6	0.3263

A comparison of the CNTHX Lewis number correlations and the Wang et al. correlation [168] to the experimental data is summarized in Figure 29. Overall, the new correlations give acceptable agreement compared to the experimental data and are slightly better than the Wang et al. correlation [168], predicting all but one test point within the ±30% threshold. Additionally, it is interesting to note that the two power law functions give nearly identical predictions. This suggests that inlet relative humidity may not be strong predictor for Lewis number. However, it must be noted that the experiments considered a single inlet relative humidity (51%), and additional experiments should be conducted across a range of inlet relative humidity values to fully understand the impact of inlet relative humidity on Lewis number.

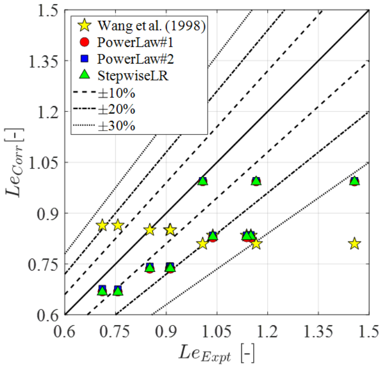

Metric	Wang et al. Correlation	Power Law #1	Power Law #2	Linear Regression
Mean Absolute Relative Difference	19.78%	17.56%	16.94%	17.54%
Maximum Absolute Relative Difference	44.42%	31.83%	31.67%	31.86%
% within ±10%	27.27%	18.18%	18.18%	18.18%
% within ±20%	54.55%	63.64%	72.73%	72.73%
% within ±30%	81.82%	90.91%	90.91%	90.91%

Figure 29: CFD-based Lewis number correlation validation & statistics.

Heat Exchanger Optimization with New Optimization Framework (M2.5, M3.1, M4.2)

Note: The contents of this section have been published in the following citation: Tancabel et al. [3].

The integrated multi-scale, multi-physics analysis and shape and topology optimization methodology discussed herein was applied to multiple design problems spanning many different system and refrigerant applications to highlight the flexibility of the newly proposed method. For the sake of brevity, one design problem is presented in detail as an example: optimization of the condenser for a commercially-available, state-of-the-art nominal 5.28 kW air-conditioning system [96] which utilizes a baseline tube-fin HX condenser.

Problem Description

This research considers air-to-R410A HXs in cross-flow where all HX models assume: (i) uniform normal inlet air velocity on the HX face and (ii) fully-developed uniform refrigerant flow. Airside thermal-hydraulic performance is predicted using CFD, while tube-level mechanical performance can be computed using FEA. Refrigerant-side thermal-hydraulic performance is calculated using existing correlations for single- and two-phase flow in small channels. The framework is utilized to design novel, finless air-to-R410A condensers which can outperform the tube-fin condenser in a commercially-available state-of-the-art nominal 5.28 kW (1.5-Ton) air-conditioning system [96]. The design variables and general schematics were summarized in Table 10 and Figure 3, respectively.

Multi-Objective Optimization

The multi-scale, multi-physics analysis with shape and topology optimization framework developed herein leverages a Multi-Objective Genetic Algorithm (MOGA) to conduct optimization [9]. The MOGA settings are summarized as follows: (i) population size of 150; (ii) population replacement of 15%; (iii) 1000 iterations. Full HX models are built and simulated using an experimentally-validated air-to-refrigerant HX modeling tool [162]. The airside thermal-hydraulic performance is evaluated with the CFD-based metamodels, while the tube-level mechanical performance is evaluated with the FEA-based metamodels. The refrigerant-side thermal-hydraulic performance is computed using empirical correlations and correction factors for single and (condensing) two-phase flow in small channels (Table 21). Refrigerant thermodynamic property calculations utilize NIST REFPROP version 9.1 [183] augmented with polynomial curve fits as proposed by Aute and Radermacher [184].

Table 21: Refrigerant-side thermal-hydraulic performance correlations.

Working Fluid	***h* Correlation**	**Δ*P* Correlation**
Air	CFD Metamodels	
Liquid refrigerant	Gnielinski (1976) [185]	Churchill (1977) [186]
Two-phase refrigerant	Shah (2016) [187]	Sun & Mishima (2009) [188]
Vapor refrigerant	Gnielinski (1976) [185]	Churchill (1977) [186]

Heat Exchanger Optimization

Optimization Problem Formulation

This research considers a bi-objective optimization problem targeting minimum airside pressure drop and HX core envelope volume. The problem formulation is summarized in Equation (5). The overall goal was to design air-to-R410A condensers featuring novel, non-round tubes. The optimal condensers should be able to replace the tube-fin condenser of a state-of-the-art nominal 5.28 kW (1.5-Ton) air-conditioning unit. All flow rates are set equal to the baseline HX. The airside pressure drop is constrained by at most double the baseline airside pressure drop value to give the optimizer increased flexibility to explore the design space. In all, four optimizations were run: two optimizations considering full tube shape optimization with a tube stress constraint and two additional optimizations targeting a fixed non-round tube shape (NTHX1) which has been conventionally manufactured in copper and will be presented in later sections of this report. The full tube shape optimization considers a copper alloy with ultimate strength (S_{ult}) of 200 MPa and a factor of safety (FS) on ultimate strength of 3.0. Of these two optimization cases, one targets a single fluid pass configuration (1P), while the second targets a three-fluid-pass configuration (3P). Note that the problem statement is sufficiently general, and it is possible to find additional promising designs by examining other pass configurations and/or removing the HX face area constraint.

$$\begin{gathered}\min \Delta P_{air}, V_{HX} \\ \text{s.t.} \\ \dot{Q}_{BL} \le \dot{Q} \le 1.1 \cdot \dot{Q}_{BL}; \quad \Delta P_{air} \le 2.0 \cdot \Delta P_{air}; \quad \Delta P_{ref} \le \Delta P_{ref,BL} \\ V_{HX} \le V_{HX,BL}; \quad 0.5 \le H_{HX}/L_{HX} \le 2.0; \quad A_f \le A_{f,BL}; \quad \sigma_{VM} \le S_{ult}/FS \\ \dot{V}_{air} = \dot{V}_{air,BL}; \quad \dot{m}_{ref} = \dot{m}_{ref,BL}; \quad \text{Number of HX Fluid Passes:}\{1,3\}\end{gathered} \tag{27}$$

The three-fluid-pass, full tube shape optimization problem considers all fifteen design variables listed in Table 10. For the fixed tube shape problem, the tube height, tube width, and tube shape control points are all fixed. Thus, only eight design variables are considered for the three-fluid-pass, fixed tube shape optimization problem: tube horizontal spacing, tube vertical spacing, number of tube banks, number of tubes per bank, inlet air velocity, and two fluid pass configuration variables. The single-fluid-pass optimization problems are identical to the three-fluid-pass problems, with the exception of removing the two fluid pass configuration variables.

Optimization Results

Figure 30 – Figure 32 present a summary of the optimization results colored by HX face area, core material volume, and core internal volume, respectively. All performance metrics are normalized with respect to the baseline HX. The dashed lines form the 20%-20% performance improvement target region for each objective. It is clear that the optimal designs from the full tube shape optimization are superior to those from the NTHX1 tube optimization, especially for the single fluid pass configuration. This is due to the full tube shape optimization allowing for significantly smaller tube shapes. In the presented cases, the full tube shape optimization tubes are at least 20% smaller than the NTHX1 tube. The benefits of smaller tubes are clearly reflected in the geometry metrics for the optimal HXs: at the baseline airside pressure drop, the smallest full tube shape optimization design has 4.5 times lower core envelope volume, 6 times lower core material volume, and 4.1 times lower core internal volume compared to the smallest NTHX1 optimal design. Compared to the baseline HX at the same airside pressure drop, the smallest full tube shape optimization design has 8.2 times lower core envelope volume, 5.5 times lower core material volume, and 6 times lower core internal volume, showcasing the power of the optimization methodology.

However, it must be noted that not all of the full tube shape optimization designs are manufacturable using today’s technology. To this end, the NTHX1 tube optimization was conducted to explore the viability of the conventionally-manufacturable non-round tube shape for this application. For the baseline airside pressure drop value, the smallest NTHX1 optimal design, which has three fluid passes, can achieve 47% reduction in HX core envelope volume, 20% reduction in HX face area, and 34% reduction in HX core internal volume compared to the baseline HX. For the minimum HX core envelope volume reduction (20%), it is possible to achieve up to 7% reduction in airside pressure drop, 20% reduction in HX face area, and 8% reduction in HX core internal volume; this is accomplished with a single fluid pass configuration. From an environmental standpoint, the tube internal volume reductions will correspond to significant charge reductions and thus lower the overall environmental impact, while the significant face area reductions are highly advantageous to HX manufacturers since face area is directly related to system footprint [44]. On the other hand, all optimal NTHX1 designs have at least a 10% increase in material volume (tubes only, no fins) compared to the baseline (tubes and fins), which results in higher material consumption and thus manufacturing costs. This is due to the NTHX1’s conservative tube thickness, which was utilized to ensure that the tube did not rupture.

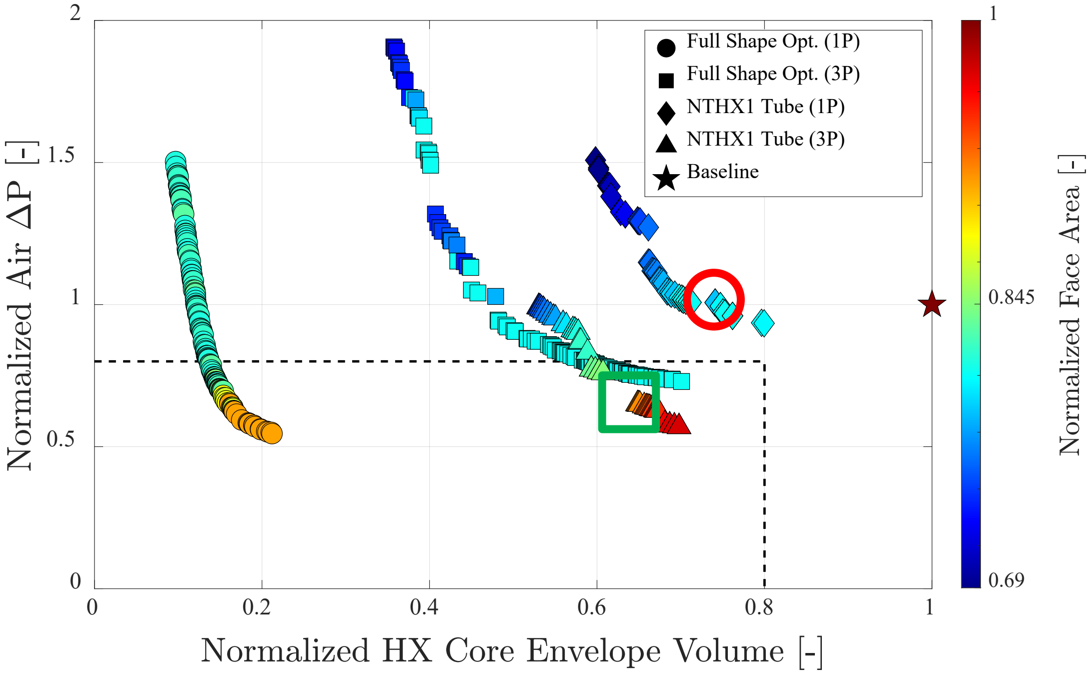

Figure 30: Optimal condenser designs colored by HX face area.

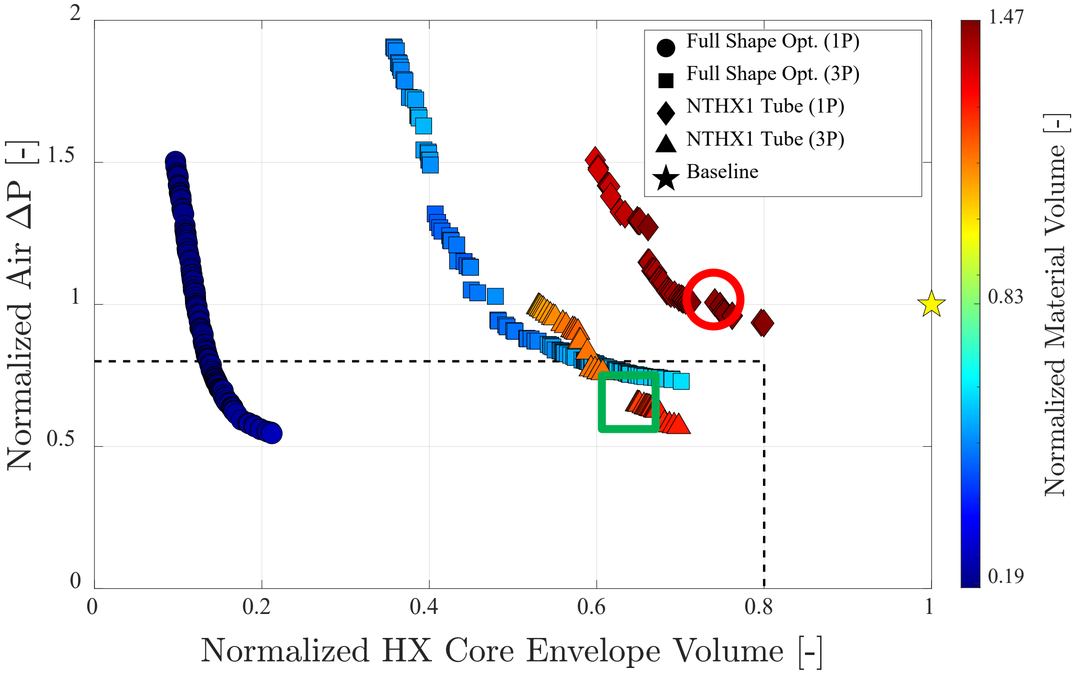

Figure 31: Optimal condenser designs colored by HX core material volume.

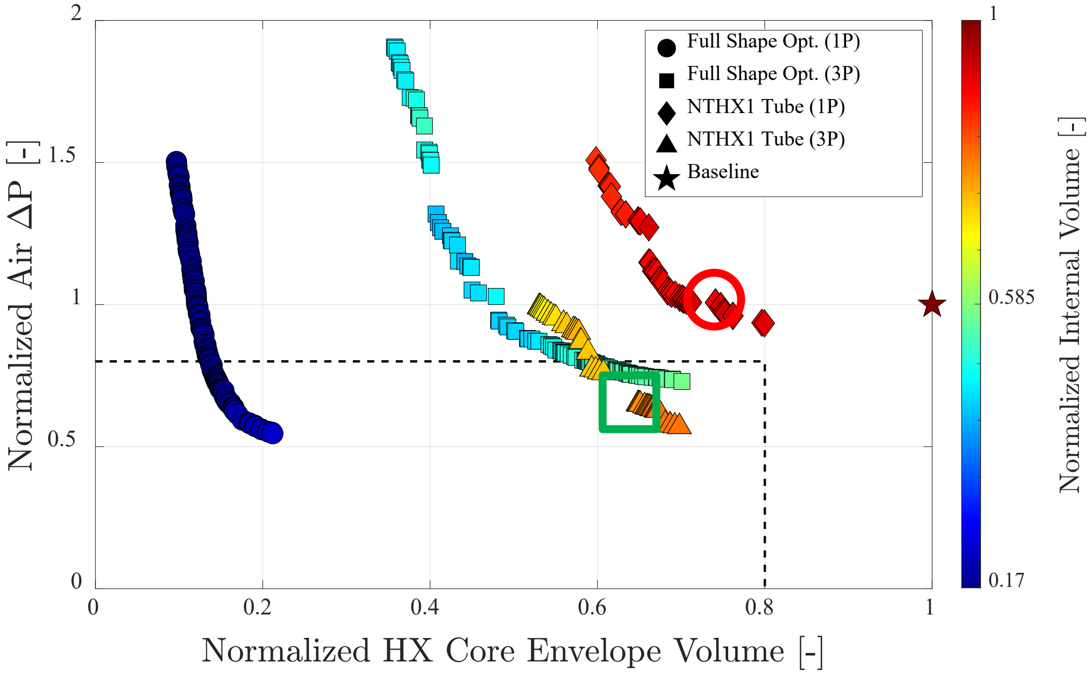

Figure 32: Optimal designs colored by HX core internal volume.

Brief Discussion on Experimental Validation

Two HX designs proposed by the design framework for this optimization problem were prototyped by HTT to conduct comprehensive component-level experimental validations. They are marked by the red circle and green box in Figure 30 – Figure 32. The experimental validation of these prototypes is summarized in later sections of this report.

<u>Summary of Optimizations Conducted</u>

The optimization framework was applied to multiple design problems (Table 22) with a wide variety of refrigerants, including conventional refrigerants (R410A), next generation replacement refrigerants (R32, R454B), and low-GWP and natural refrigerants (R290, supercritical carbon dioxide (sCO_2)), and applications (A/C system, heat pump system, gas coolers). It is clear that the optimization framework is capable of designing HXs utilizing non-round, shape- and topology-optimized tubes which show significant improvements over state-of-the-art baseline HXs across a wide variety of HX geometric and thermal-hydraulic performance metrics, including satisfying the objectives of >20% smaller and >20% improved thermal-hydraulic performance. Of all cases considered, only one optimization did not result in HXs which completely outperformed the baseline across all metrics (face area for sCO2 gas cooler with a microchannel HX baseline). In this case, it was noted that the HX core envelope volume reductions were due to large HX depth reductions resulting from the small tube size, and some potential methods to find additional designs with reduced face areas would be to allow for more tube banks in the depth-wise direction and/or to consider a HX with multiple slabs. The generality of the optimization framework developed herein allows such considerations and should be explored in the future to find HX designs with even greater improvements beyond those listed in Table 22.

Table 22: Summary of completed HX optimization studies (with References).

				Best Case Improvements			
Reference	**Optimization Study**	**Application**	**Tube Shape**	**Air ΔP**	**Core Envelope Volume**	**Face Area**	**Core Internal Volume**
Tancabel et al. [3]	R410A Condenser (A)	Nom. 5.28 kW A/C system	NTHX1	43%↓	47%↓	31%↓	31%↓
	R410A Condenser (B)	Nom. 5.28 kW A/C system	Variable	46%↓	90%↓	27%↓	83%↓
Tancabel et al. [189]	R410A Condenser (C)	Nom. 5.28 kW A/C system	NTHX1	62%↓	53%↓	34%↓	43%↓
Internal Study (A)	R410A Evaporator	Nom. 5.28 kW A/C system	NTHX1	82%↓	68%↓	16%↓	70%↓
Internal Study (B)	R410A Indoor Unit HX (A)	Dual-mode heat pump	NTHX1	62%↓	N/A	40%↓	N/A
	R410A Indoor Unit HX (B)	Dual-mode heat pump	Variable	77%↓	N/A	37%↓	N/A
Tancabel et al. [189]	R32 Condenser	Nom. 5.28 kW A/C system	NTHX1	47%↓	57%↓	50%↓	44%↓
	R454B Condenser	Nom. 5.28 kW A/C system	NTHX1	63%↓	47%↓	34%↓	41%↓
Tancabel et al. [190]	R290 Condenser	Nom. 2.4 kW A/C system	NTHX1	43%↓	69%↓	14%↓	49%↓
Tancabel et al. [191]	sCO_2 Gas Cooler (A)	FTHX Baseline	Variable	N/A	74%↓	7%↓	74%↓
	sCO_2 Gas Cooler (B)	MCHX Baseline	Variable	79%↓	85%↓	133%↑	73%↓

Heat Exchanger Fatigue Analysis (M2.2, M2.4)

Certain aspects of the technologies or methodologies described in this section may be the subject of one or more patent applications and/or issued patents, including U.S. Patent App. No. 17/196,894, now published as U.S. Patent Pub. No. 2021/0285727.

Stress & Fatigue Analysis Framework

Note: The contents of this section have been published in the following citation: Zhang et al. [192].

Previous studies have revealed that HXs with non-round tubes can offer high heat transfer performance with minimal hydraulic penalty [16]. The FEA modeling in present work was developed based on novel, non-round tube HXs. Figure 33 shows a sample non-round tube HX, which is comprised of tubes, headers, and spacers which maintain the tube pitch throughout the HX core.

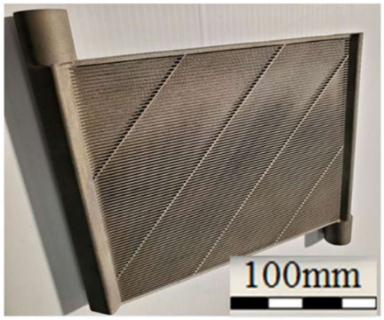

Figure 33: Sample non-round tube HX produced by additive manufacturing [16].

A fatigue analysis framework has been developed to analyze the mechanical performance and fatigue risk of HXs with non-round tubes and includes the following steps:

1. The HX geometry is digitized using CAD software SOLIDWORKS [193].
2. The HX geometry is imported into the simulation software Abaqus [194], where the simulation domain is defined (single tube or entire HX), constrains were assigned (tie between header/solder, between solder/tube), boundary conditions and loads were set (6 MPa or 3.45 MPa baseline at the inner tube wall and header), and the mesh is created.
3. Linear stress analysis simulations are performed.
4. The linear stress analysis results were imported into the fe-safe suite [195] to conduct detailed fatigue analysis simulations.

The fatigue analysis relies on material properties which are usually collected by experimental tests. To analyze the materials whose test data are not available, fatigue properties can be approximated using the built-in Approximate Material Function in Abaqus [194]. This function uses Bäumel-Seeger’s method [196] to generate approximate fatigue parameters based on the ultimate tensile strength (UTS) and elastic modulus of the material.

The stress analysis modeling was validated by comparing the predicted tube deformation to the measured deformation obtained from an experimental static pressure loading test as shown in Figure 34(a). A single tube was tested by injecting pressurized gas from one end of the tube, while the other end was sealed. The tube material was either copper or aluminum. The tube deformation was defined as the change in tube height (i.e., highest and lowest point of the tube) before and after applying pressure. The maximum applied pressure was 20 MPa. To mimic the experimental setup, a numerical model for pressure-loading single tubes was developed as shown in Figure 34(b). A comparison of the predicted and experimental tube deformation for an aluminum non-round tube is shown in Figure 35. The comparison shows a very good agreement between numerical model results to the experimental data, validating the stress analysis modeling and enabling the development of the HX fatigue analysis modeling.

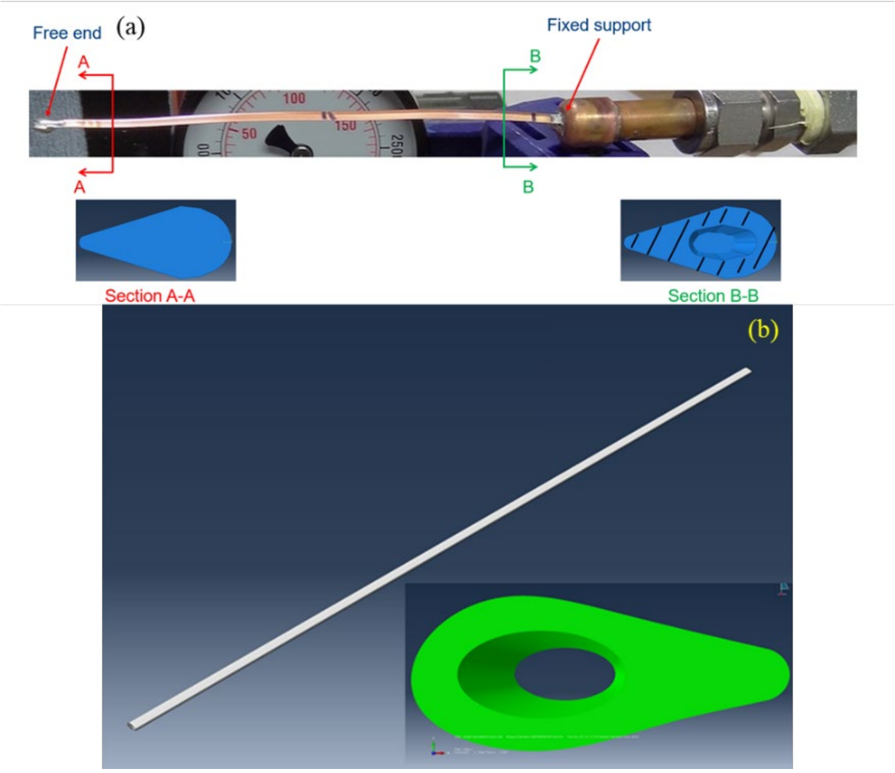

Figure 34: Single tube deformation test: (a) Experimental setup; (b) Numerical model.

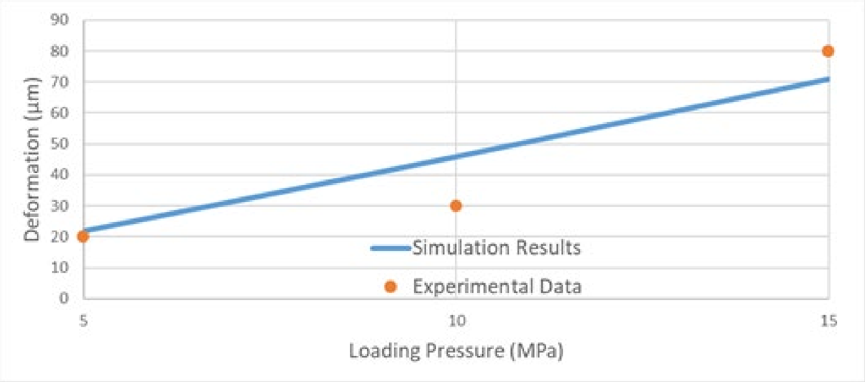

Figure 35: Single tube deformation test: (a) Experimental setup; (b) Numerical model.

Single Tube Fatigue Analysis

The framework was first utilized to conduct fatigue analysis for single tube samples using two different kinds of materials: (i) Al6061-T6 forging and (ii) 99.99% copper. The baseline pressure loading is 6 MPa (870 PSI) applied to the tube inner surface to mimic the refrigerant hydraulic pressure. Note that 6 MPa is approximately a 2x factor of safety for the operating pressure of R410A condensers for A/C applications. Since saturation pressure depends on the refrigerant, the loading was scaled up to a factor of 10x in the fatigue analysis to understand the impact of severe pressure loading with higher pressure refrigerants than those seen in R410A systems. Note also that the stress scale-up is for the fatigue analysis only, and the static stress analysis need only be conducted for the baseline loading, significantly reducing the simulation time. The loading was periodically applied to the tube, i.e., in one loading cycle, the applied pressure is from the scaled loading (e.g., 12 MPa if the scale factor is 2) to zero, then that back to the scaled loading for one complete cycle. The fatigue analysis returns a metric termed “life repeats”, which is defined as the number of loading cycles the part experiences until the first failure occurs, indicating the lifetime of the part.

Figure 36 shows the fatigue analysis results for four non-round tube shapes using both copper (99.99% Cu) and aluminum (Al6061-T6 forging) for different loading scale factors. Note that the maximum number of cycles set in the fatigue analysis simulations is 1E+08, so if the parts can withstand more than 1E+08 cycles, the data is not shown. It is clear that all tubes can bear more than 1E+08 loading cycles without failure for the baseline 6 MPa loading. From a material perspective, it was found that the copper tubes fatigue curves have gentler slopes than the aluminum alloy, suggesting that the lifetimes of 99.99% copper tubes are less than Al6061-T6 forging when the loading scale is low. However, as the loading scale increases, 99.99% copper tubes have longer lifetimes than the Al6061-T6 tubes.

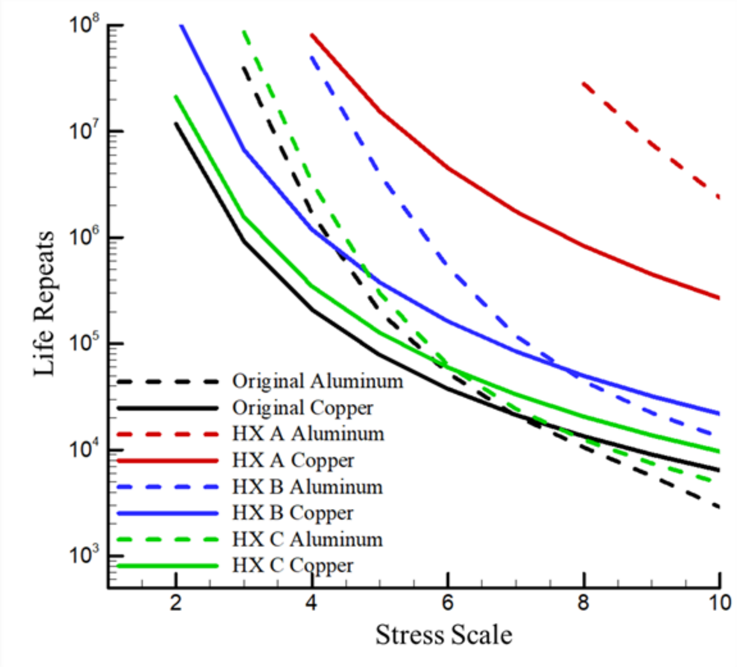

Figure 36: Single tube fatigue analysis: 4 tube designs using copper and aluminum.

Also shown in Figure 36 the black, red, blue, and green colors represent the results for Original Tube, Tube A, Tube B, and Tube C tubes, respectively. Figure 37 and Figure 38 present contours for the logarithmic value of the number of life cycles when the loading scale factor is set to 10 for copper and aluminum, respectively. It is clear that for the original design, the critical location is at the two extreme horizontal ends of the internal channel for all designs, which is often the location of the sharpest corner and thus significant stress concentration. Of all designs, Tube A is the best performing, likely due to the two round internal channels having minimal stress concentration (no sharp corners on the internal channel). The worst-performing tubes are the Original Tube and Tube C, where the main difference is that Tube C has a smaller, elliptical-shaped internal channel geometry which, from Figure 36, does slightly improve the fatigue life performance, but only marginally.

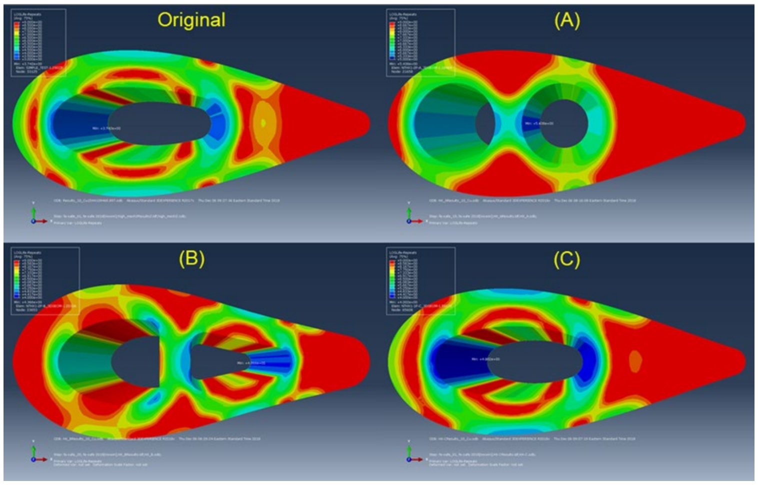

Figure 37: Single copper tube fatigue analysis: Contours of logarithmic life cycles.

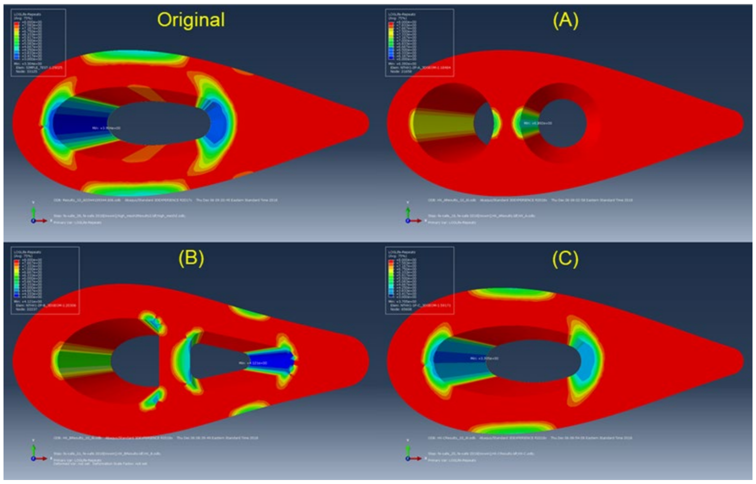

Figure 38: Single aluminum tube fatigue analysis: Contours of logarithmic life cycles.

<u>Header Stress Analysis</u>

Stress analyses were conducted on the HX header to investigate the impact of header shape and reservoir depth on the mechanical performance of the HX header.

Effect of Header Shape

A stress analysis model was developed to study the effects of header shape on mechanical performance. The cross-sections of interest are square, half round, and round (Figure 39), where the header material is copper. An internal pressure of 3.45 MPa is applied to header internal surfaces to obtain the header stress contours shown in Figure 40. The results indicate that for all shapes, the stress concentration happens at the same place: the header inner surface opposite the slot for the tube bundle. When comparing the stress magnitude, the round shape has the lowest maximum stress (~115 MPa) while the square shape has the highest maximum stress (~540 MPa). The half round shape can significantly reduce the maximum stress on the header (maximum stress of ~160 MPa) while serving as a good trade-off between the round and square geometries.

Figure 39: Header cross-sections: (Left) Square; (Middle) Half-Round; (Right) Round.

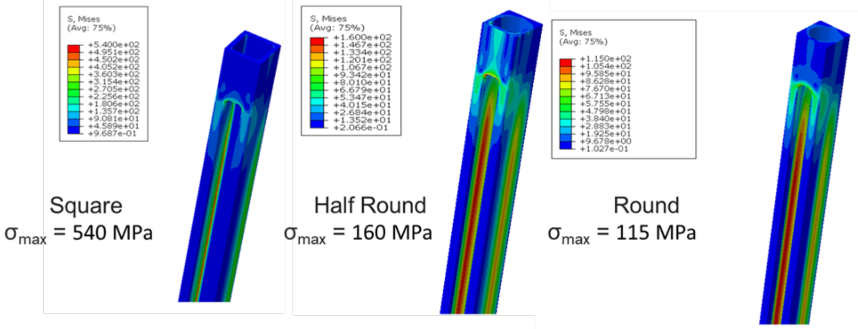

Figure 40: Header stress distribution: (Left) Square; (Middle) Half-Round; (Right) Round.

Effect of Header Volume

The header stress analysis model was then utilized to study the effects of header volume on the mechanical performance. Since the header length and height are fixed based on the tube bundle geometry, the only parameter of interest is the header width (Figure 41). Three header widths were investigated: (i) 10 mm, (ii) 7.5 mm, and (iii) 5 mm, where the internal pressure is again set to 3.45 MPa (500 PSI). Figure 42 shows the stress distribution at the same cross-section cut location of the different-sized headers, where the maximum stress on the 10 mm, 7.5 mm, and 5 mm headers are 16.8, 16.73 and 14.95 MPa, respectively. It can be concluded that no significant stress difference can be observed when the header width changes from 10 mm to 5 mm. This analysis indicated that a HX designer can size the internal channel of the header to focus on minimizing refrigerant charge and also the impacts of header pressure drop and flow maldistribution rather than focusing on the mechanical performance, which was relatively insensitive to header internal channel size.

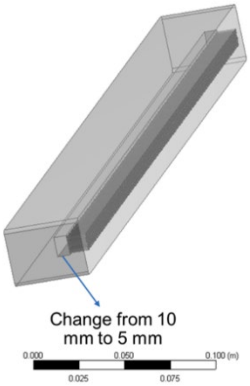

Figure 41: Header cross-sections: (Left) Square; (Middle) Half-Round; (Right) Round.

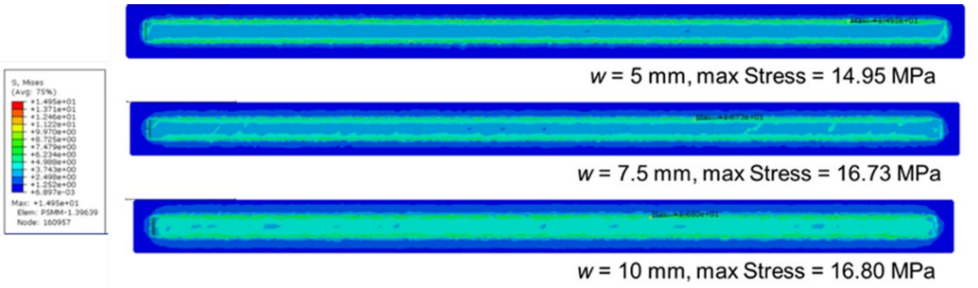

Figure 42: Header stress distribution: (Left) Square; (Middle) Half-Round; (Right) Round.

Effect of Imperfect Fitting of Tubes and Spacer Holes

In real fabrications, the tubes will not perfectly fit into the spacer holes, which may lead to stress concentration. To this end, the impact of an imperfect tube-spacer joint was investigated for a sample test case (Figure 43) where the tube was rotated 1.5° from the original orientation, creating an uneven distribution of solder for the tube-spacer joint. The internal surface pressure was fixed to 3.45 MPa across the entire HX. Here, the tube and spacer are copper while the solder is aluminum. Figure 44 shows the stress distribution in the solder with ideal orientation (no rotation) and 1.5° rotation, respectively. The highest stresses from the two cases are 113 and 134 MPa, respectively, indicating that the tube rotation increases the stress in the solder and further emphasizing the need for accurate tube hole cuts for header manufacturing.

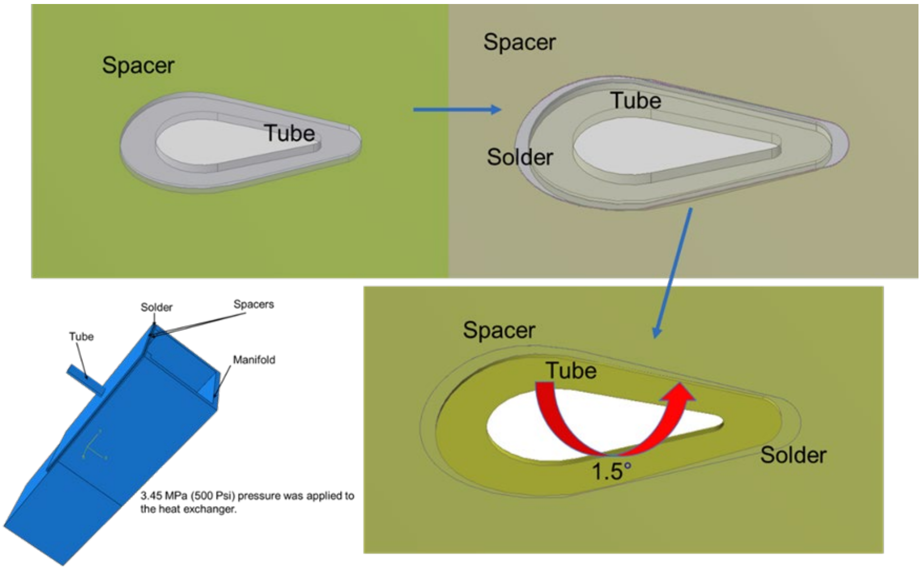

Figure 43: Header stress analysis for imperfect tube-solder joints.

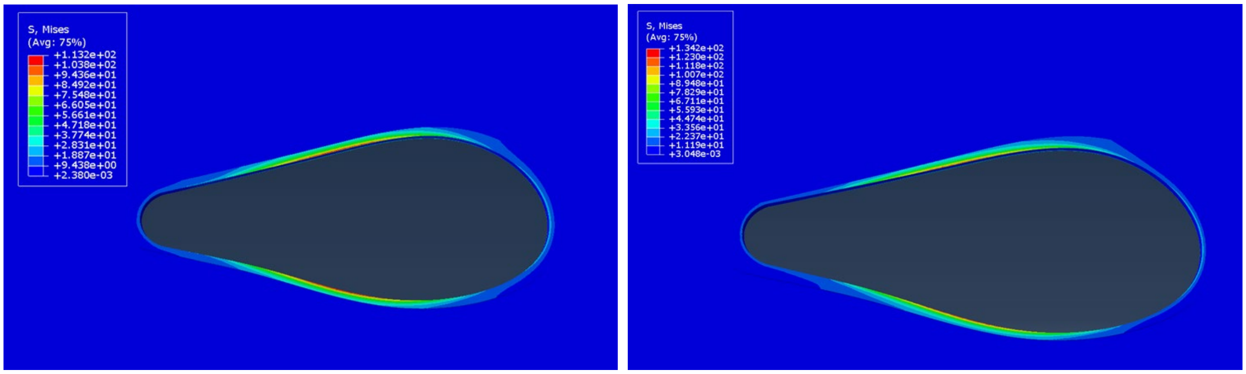

Figure 44: Solder stress distribution: (Left) Ideal fit vs. (Right) tube with 1.5° rotation.

Plastic Strain Modeling of the Solder

Since the stress is high on the tube-solder joint (~130 MPa), the strain in the solder may be beyond the elastic region. Therefore, it is necessary to conduct a study on the plastic strain on the solder. The model shown in Figure 43 was thus extended to consider plastic effects in the solder. The solder is made of SAC 396 (Alloy: Sn95.5Ag3.9Cu0.6), while all other components are made of copper. Actual plastic stress-strain curves are employed to describe the stress-strain relationships for two solder alloys, (i) SAC 396 and (ii) copper, with yield stress 35 MPa and 120 MPa, respectively (Figure 45). Figure 46 depict the plastic stress and strain on the solder. When using SAC 396 solder (yield strength = 35 MPa), the highest stress on the solder will be the yield stress, indicating the solder is truly in the plastic deformation region with maximum plastic strain of 3E-03 m/m.

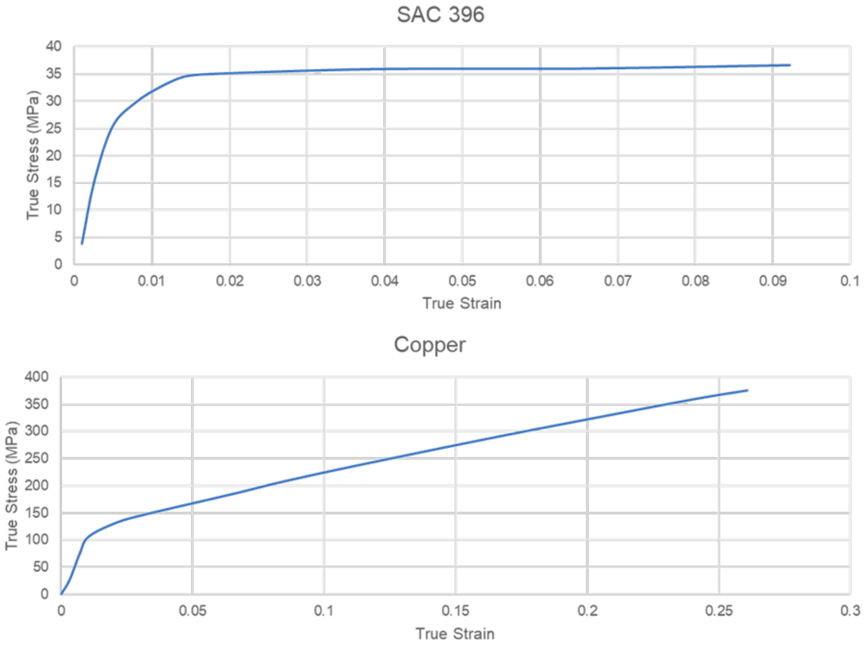

Figure 45: Plastic stress-strain curves: (Top) SAC 396; (Bottom) Copper.

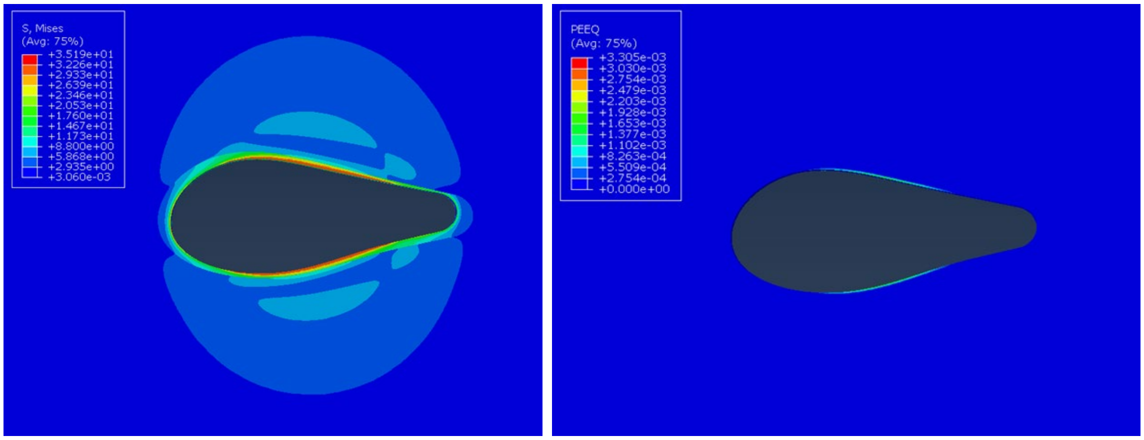

Figure 46: Solder plastic stress analysis: (Left) Plastic stress; (Right) Plastic strain.

Fatigue Analysis of Fully Assembled HXs

Note: The contents of this section have been published in the following citation: Zhang et al. [197].

Figure 47 shows a schematic view of the HX header assembly studied in this section, which is comprised of tubes and two headers at the two ends of each tube. Tubes are connected to the header though a layer of solder as the joining material. To save computational resources, some simplifications have been applied: (i) the symmetric nature of the HX geometry of allows only half of the HX to be considered; and (ii) . only 7 tubes are included in the model instead of the full HX (typically 100-1000s of tubes) since a preliminary test revealed that a 7-tube model can accurately capture the stress changes due to interactions between tubes, and thus the locations and values of maximum stress from the 7-tube model is very close to the full HX model considering >100 tubes. The materials of solder and tube/header are Al4004 and Al6063-T6, respectively. As before, the inner pressure of the HX is set to 3.45 MPa (500 PSI) and is applied to all inner surfaces of the tubes and header.

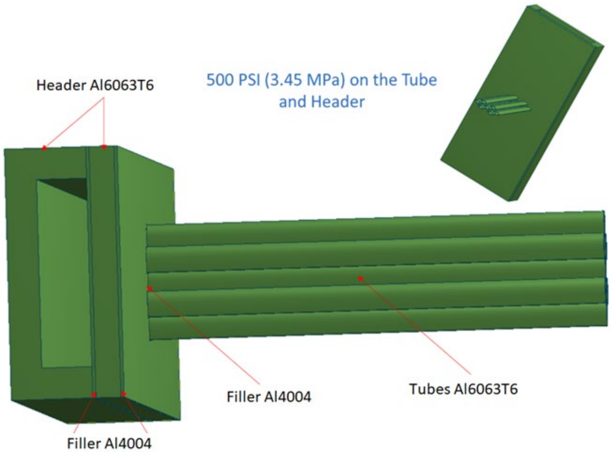

Figure 47: Schematic model of full tube-header assembly.

Three tube cross-sections are considered as shown in Figure 48. The tubes are connected to the header with thin layer of solder, depicted as thin brown layers in Figure

48. Note that the outer perimeters of the solder layer are approximately the same for all tube shapes (~5 mm), while the solder and tube wall thicknesses are 0.06 mm and 0.1 mm for all shapes, respectively.

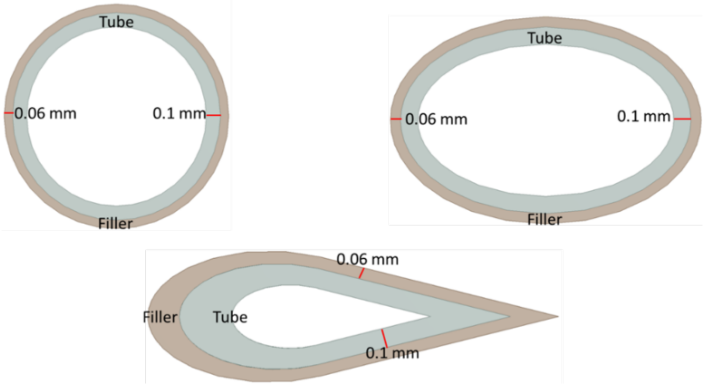

Figure 48: Tube shapes of interest: (Top Left) Round; (Top Right) Ellipse; (Bottom) Non-Round Tube.

Figure 49 depicts the stress on the tubes for all three cases. Note only four of the seven tubes are shown for simplicity. The highest stresses on the round, ellipse, and non-round tubes are 28.7 MPa, 189.1 MPa, and 84.1 MPa, respectively. It is unsurprising that the round tubes have the lowest stress levels, as the ellipse and non-round tubes have significant stress concentration at the extreme horizontal ends of the tube. However, it is important to note that, while the non-round tube trailing edge comes to a sharp point, the large material thickness at this location reduces the stress concentration and results in the non-round tube having lower stress than the ellipse tube and higher stress than the round tube.

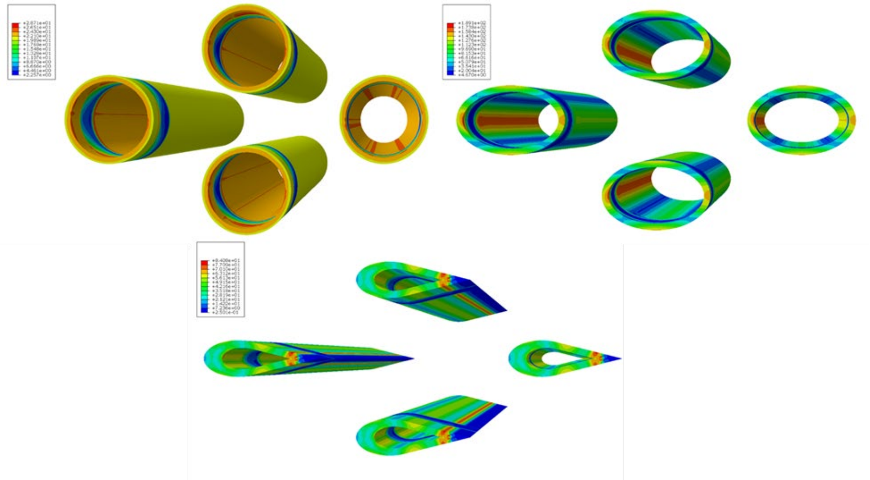

Figure 49: Tube bundle stress contours: (Top Left) Round; (Top Right) Ellipse; (Bottom) Non-Round Tube.

The stress distribution of the solder for all three cases are shown in Figure 50. The highest stresses on the round, ellipse, and non-round solders are 22.1 MPa, 49.0 MPa, and 46.2 MPa, respectively. A key difference in the location of the maximum stress location for the tubes and the solder is apparent, especially for the non-round solder. That is, the critical locations of the round and ellipse solder are the extreme top, bottom, left, and right vertices of the shape, while the highest stresses on the non-round solders occur near the edges of upper and lower surfaces instead of the trailing edge sharp corner. This is due to the pressure being applied directly to the tubes then being passed through the tube thickness to the solders. The location of the highest stress in the solder happens at the location of minimum tube thickness, which may not necessarily coincide with the maximum stress location on the tube cross-section.

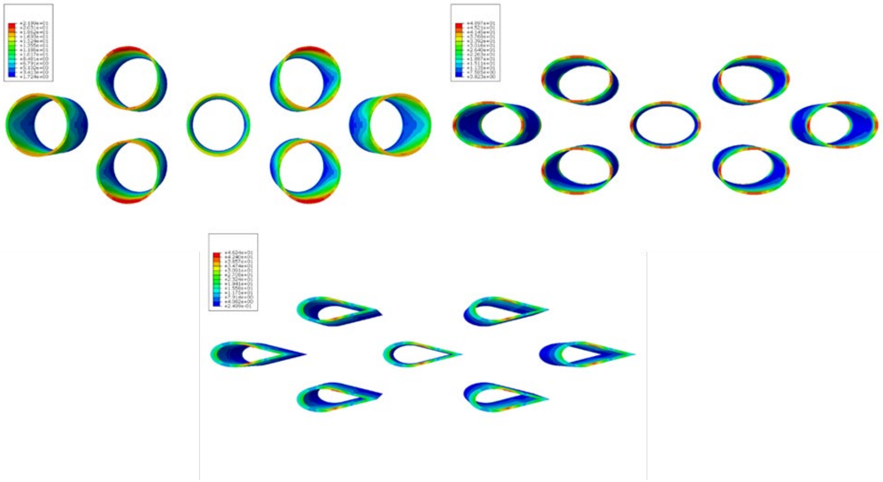

Figure 50: Tube bundle solder stress contours: (Top Left) Round; (Top Right) Ellipse; (Bottom) Non-Round Tube.

Figure 51 shows the stress distributions within the headers, where the highest stress is less than 18 MPa. Note that the green background indicates that most of the header experiences stresses on the order of 7 MPa and directly results from the pressure applied directly to the header. Some low stress areas can be found between holes resulting from the interactions between two applied stresses creating low stress regions.

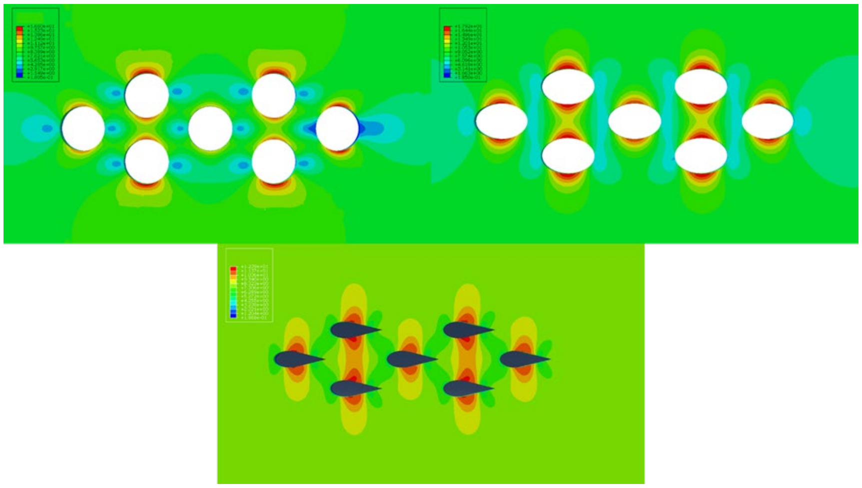

Figure 51: Header stress contours: (Top Left) Round; (Top Right) Ellipse; (Bottom) Non-Round Tube.

The results of the static stress analysis were used to conduct fatigue analysis for the HX header assembly. As before, a “1-0” stress curve is implemented, i.e. the stress switches repeatedly from “1” to “0” then back to “1”, where “1” and “0” indicate an applied stress (computed from the above stress analysis) and no applied stress, respectively. As with the single tube fatigue analysis, the internal pressure loading is scaled up to 10x the baseline value to investigate the effects of different loading conditions. The metric of interest is the number of life repeats. Figure 52 shows the impact of stress scale on the lifespan of the header assemblies. Since the stress on the ellipse tube HX is the highest, it has a shortest lifespan of ~1 million cycles at the baseline loading and ~34 cycles with 10x loading. Assuming a typical, steady-state compressor duty cycle is ~40 minutes, it can be calculated that an ellipse tube HX header with this design will have a lifespan of ~38 years. The other two designs have even longer lifespans.

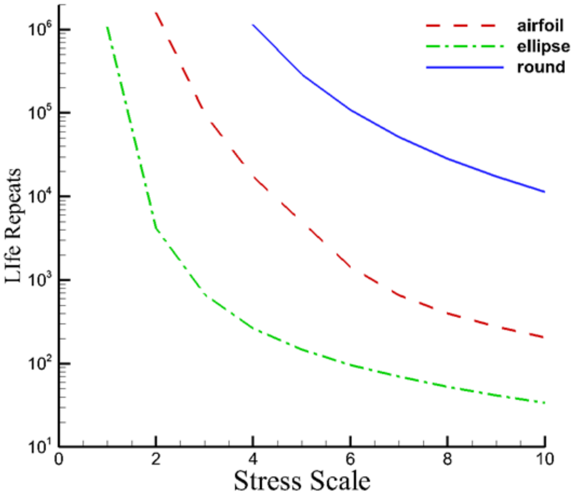

Figure 52: Life repeats vs. stress scale for different tube-header designs.

Summary

A framework of static stress and fatigue analysis of high-performance HXs with non-round tubes was developed. The framework includes CAD modeling with SOLIDWORKS [193], stress analysis modeling using by ABAQUS [194], and fatigue analysis using fe-safe [195]. The stress analysis model was validated by comparing tube deformation under internal pressure loading to experimental data. The framework was utilized to analyze the stress and fatigue life for different HX components, including individual tubes, headers, and welding layers, as well as for the fully-assembled HXs. Some conclusions are summarized as following:

- A fatigue analysis was conducted on four tube geometries with unique internal port shapes. It was found that that tube fatigue life can be improved by exploring rounded port shapes and also implementing multi-port tube designs.
- A stress analysis was conducted on three header cross-section geometries. It was found that that more rounded header shapes improve mechanical performance. In addition, the header depth was found to have minimal impact on header mechanical performance.
- The effects of imperfect fitting of the spacer and tube was investigated. It was determined that imperfect tube-spacer joints increase the stress on the solder joint by ~20% when the tube is rotated 1.5° versus a level fit, which will slightly reduce the overall lifespan of the part.

- The framework was utilized to conduct fatigue analysis on fully-assembled HXs using three tube shapes, (i) round, (ii) ellipse, and (iii) non-round. The fatigue analysis indicates that although the ellipse-tube HX has the lowest lifespan of the three HXs, the part should be able to survive ~1 million cycles without failure under the baseline loading.

Heat Exchanger Manufacturing (M2.4, M 3.2, M 4.1-4.2)

Certain aspects of the technologies or methodologies described in this section may be the subject of one or more patent applications and/or issued patents, including U.S. Patent App. No. 17/196,894, now published as U.S. Patent Pub. No. 2021/0285727.

The manufacturing efforts for this project are listed below. A detailed report on each effort is included in the following section.

- (M2.4) Investigation of novel non-round tube manufacturing & tube-header integration methods.
- (M3.2) Fabrication of HX prototypes using manufacturing methods developed in M2.4. The HX nominal capacity was 3-5 kW and were based on optimizations conducted using the aforementioned framework from M2.3.
- (M4.1-4.2) Fabrication of HX prototypes for higher-capacity applications (~3-Tons) incorporating industry feedback on non-round tube manufacturing and tube-header integration strategies and were based on optimizations conducted using the M2.3 framework.

Heat Exchanger Prototypes Summary

This project resulted in ten HX prototypes which utilize non-round tube shapes which are summarized in Table 23. Nine HXs were prototyped by HTT utilizing conventional manufacturing methods developed as a result of this project while one HX was prototyped using additive manufacturing methods. Images of the HXs are summarized in Figure 53.

Table 23: HX Prototype Summary.

Serial Number (HX Material)	Application	Nominal Capacity	Pressure Test Status	Experimental Evaluation
1 – C2 (Copper)	Air-to-R410A Condenser	400 W	Leak tight (~300 psig)	N/A
3 – C1 (Copper)	Air-to-R410A Condenser	400 W	Leak tight (~400 psig)	• Dry Evaporator Testing • Capacity predicted within ±10% • Air ΔP predicted within ±30% • Sim. consistent overprediction • Wet Evaporator Testing (R-410A) • Sensible load predicted within ±10% • Latent load predicted within ±20% • Air ΔP under wet operation up to 2.3x higher than under dry operation
ENTHX-001 (Titanium)	Air-to-Water Radiator	3.2 kW	Leaking (~20 psig) Leaks on tubes (x3)	• Capacity predicted within ±10% • Air ΔP predicted within ±40% • Attributed to high surface roughness from AM printing
6 – C3 (Copper)	Air-to-R410A Condenser	1.10 kW	Leak tight (~400 psig)	N/A

7 – C4 (Copper)	Air-to-R410A Condenser	1.63 kW	Leaking (~400 psig)	N/A
8 – C4 (Copper)	Air-to-R410A Condenser	1.63 kW	Leaking (~350 psig)	N/A
9 – E1 (Copper)	Air-to-R410A Evaporator	4.48 kW	Leak tight (~300 psig)	N/A
10 – E2 (Copper)	Air-to-R410A Evaporator	5.67 kW	Leak tight (~300 psig)	• Two test points simulated at UMD • Independent validation testing at industry partner laboratory • Performance agrees within 10% of predicted values and performance data from CEEE lab
11 – E2 (Copper)	Air-to-R410A Evaporator	5.67 kW	Leaking	N/A
12	Air-to-R410A Condenser	11.27 kW	Failed pressure test	N/A

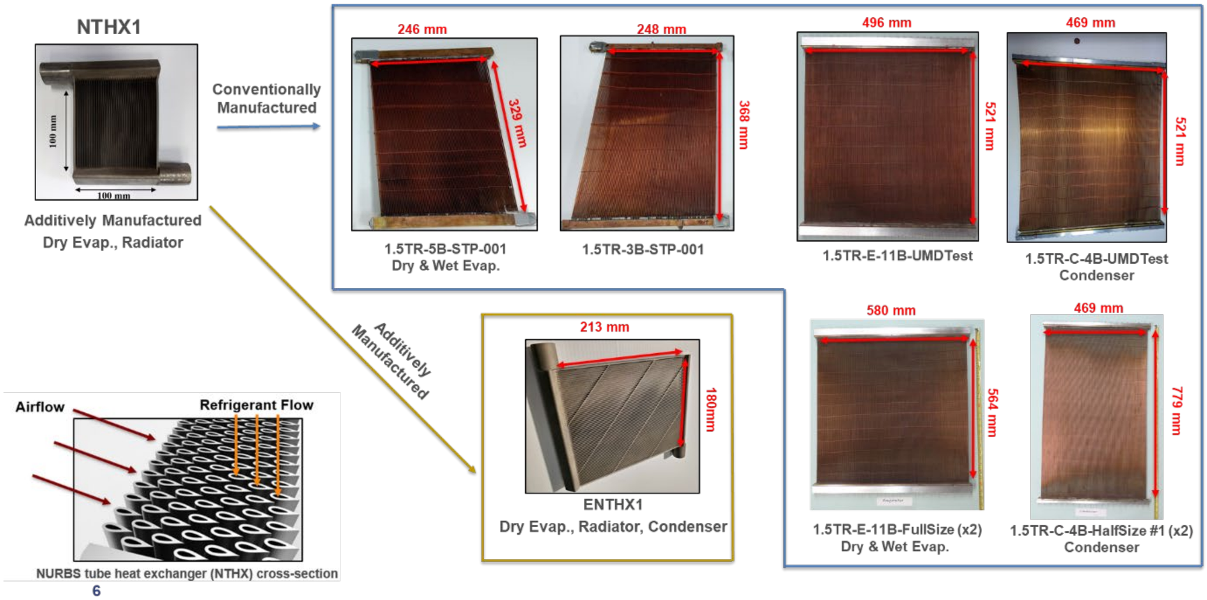

Figure 53: Images of HX prototypes manufactured during the project.

Non-Round Tube Manufacturing

Three companies were contracted to produce non-round tubes for the HX prototypes produced during this project, one for copper tubes and two for aluminum tubes. A summary of the tube manufacturing developments is provided below.

- Small Tube Products (STP) produced non-round tubes by reforming round copper tubes (0.16 mm wall thickness) using a drawing process (Figure 54). The project team placed an order for 45 kg of tubes, which resulted in 9,024 tubes with a total length of >5.5 km. These tubes were utilized in six HX prototypes.
- Brazeway produced non-round tubes via aluminum extrusion to produce four non-round tube profiles. One example is shown in Figure 55.
- MetalKraft produced ~3000 non-round tubes via aluminum extrusion (Figure 56) which were utilized to build one HX prototype.

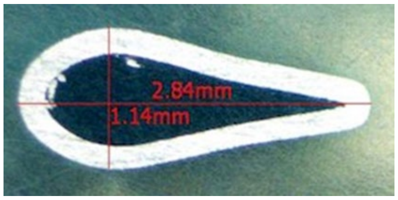

Figure 54: Non-round copper tube profile manufactured by drawing at STP.

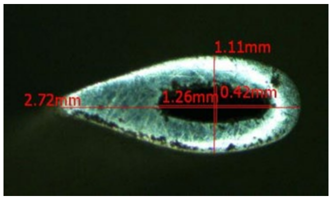

Figure 55: Non-round aluminum tube profile manufactured by extrusion at Brazeway.

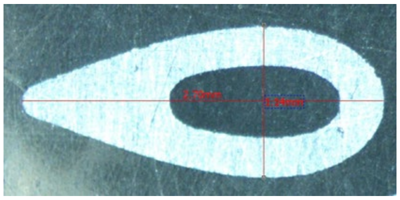

Figure 56: Non-round aluminum tube profile manufactured by extrusion at MetalKraft.

Copper Heat Exchangers

HX Prototype 6-C3

Prototype 6-C3 (Figure 57) is an air-to-R410A condenser with a nominal capacity of 1.10 kW (see Table 23). This prototype was pressure tested without leaks up to 2.7 MPa (400 PSI). A single baffle location is shown in red in Figure 57.

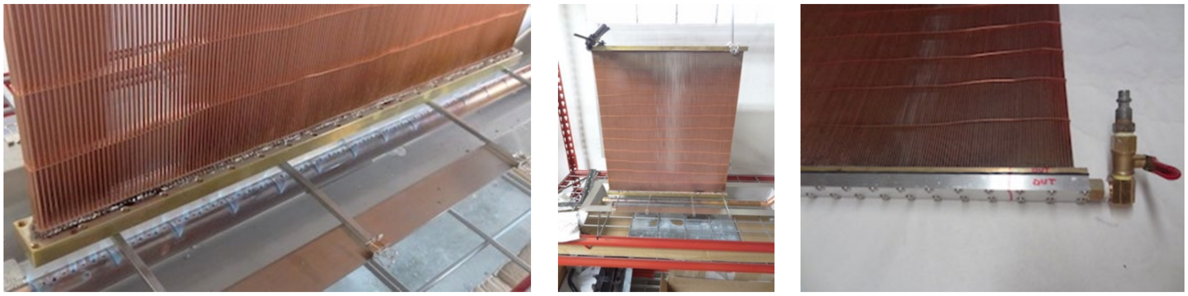

Figure 57: HX Prototype 6-C3: (Left, Middle) Under construction; (Right) Pressure Test and Baffle location shown in red.

HX Prototype 7-C4 & 8-C4

Prototypes 7-C4 (Figure 58) and 8-C4 are two identical air-to-R410A condensers with a nominal capacity of 1.63 kW (see Table 23). This HX design includes a baffle in each header. These HXs were pressure tested without leaks up to 3.0 MPa (450 PSI).

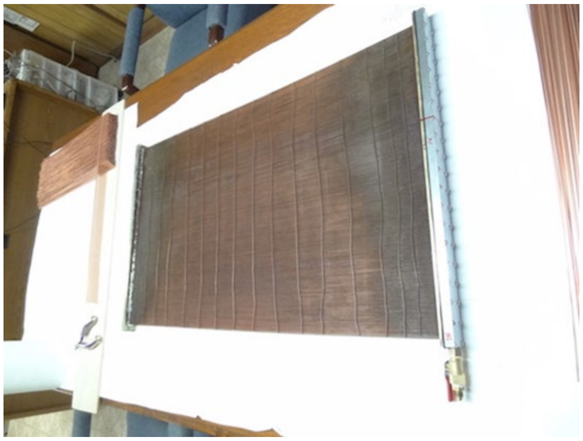

Figure 58: HX Prototype 7-C4.

HX Prototype 10-E2

Prototype 10-E2 (Figure 59) is an eleven-bank air-to-R410A evaporator with a nominal capacity of 5.67 kW (see Table 23) with identical tube bundle geometry as 9-E1 and 11-E2. Wire EDM cutting of the headers revealed good overall casting, although some areas required additional solder: These prototypes were pressure tested without leaks up to 1.5 MPa (250 PSI).

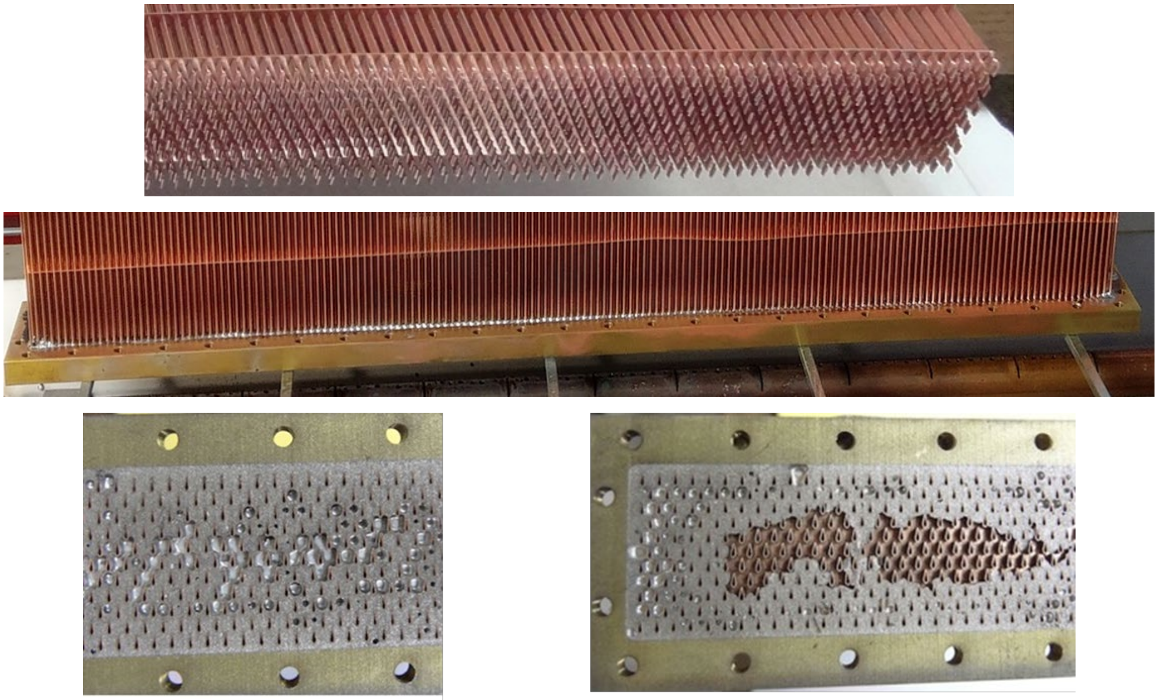

Figure 59: HX Prototype 10-E2: (Top) Tube bundle; (Middle) Header after casting; (Bottom) Cut header with tube ends showing.

Aluminum HX Prototype Manufacturing for System-Level Testing

An all-aluminum HX prototype was manufactured by HTT with the intent to be used as a drop-in replacement for the baseline tube-fin condenser for system-level experimental testing of a packaged unit A/C system.

Aluminum HX Construction

Aluminum HX Tube Procurement

New aluminum tubes were procured using Al 6063 alloy (Figure 60). The tubes had no twist, bowing, or end-cut burrs. The tubes were "aged" since selected 6063 alloy can be age hardened to improve tube handling.

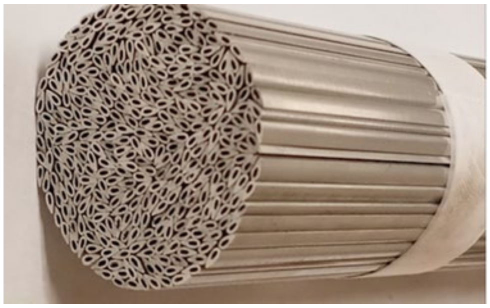

Figure 60: Al 6063 tubes for all-aluminum HX prototype (one bundle shown).

Aluminum HX Assembly

The aluminum HX tubes were threaded into the spacer and headers at HTT (Figure 61). At the brazing facility, the U-channel tanks were tack-welded to the header, and side rails were tack-welded to the tank to complete the frame. During brazing, the tank ends remain open and will be covered with welded caps post-braze (Figure 62).

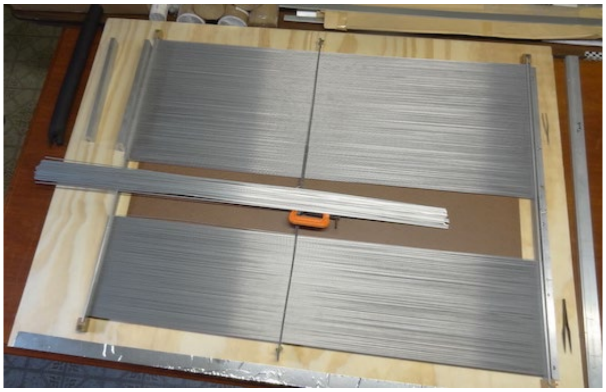

Figure 61: Aluminum HX assembly (~75% complete HX prototype shown).

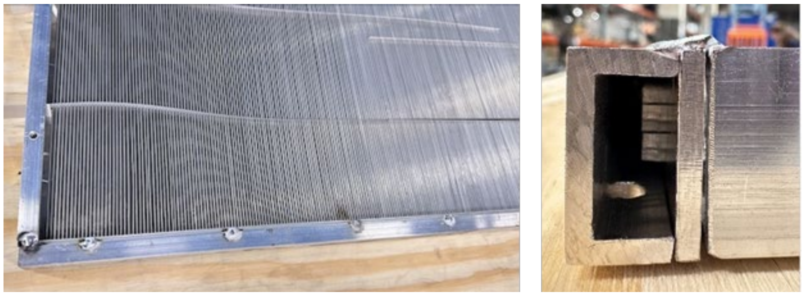

Figure 62: Aluminum HX pre-braze: (Left) Complete frame; (Right) Open tank ends.

Aluminum HX Brazing

The all-aluminum condenser prototype (left image in Figure 63) was brazed at Diesel Radiator using the Diesel Radiator brazing expert determined braze cycle based on similar-sized HXs with the same header type (i.e., headers joined to U-channels of the same size). Prior to brazing, all tubes were straight, and the HX was square. A post-braze inspection revealed that the braze alloy did not fill some areas around some tubes (red arrow in Figure 63). Diesel Radiator recommended re-brazing with a modified braze recipe, although unsuccessful since gaps remained. A third braze cycle was determined too risky due to silicone erosion and weakening of the alloys from multiple brazes.

Figure 63: (Left) Full aluminum HX prototype before brazing at Diesel Radiator; (Right) Post-braze inspection revealed small gaps near tube trailing edges.

Aluminum HX Leak Testing & Leak Repair

Multiple tube-to header leaks and some header-to-tank leaks were found on both headers (Figure 64). Since re-brazing was not an option, HTT investigated multiple adhesive solutions which could accomplish the following (i) Penetrate and seal small cracks and gaps; (ii) resist 90°C; (iii) hold 3.4 MPa (500 PSI) pressure (i.e., slightly higher than typical R410A condenser pressures for A/C applications).

Figure 64: Full aluminum HX prototype with multiple post-braze leaks.

HTT investigated many adhesives as potential leak sealing solutions. A test block with varying hole diameters between 1.0-2.0 mm were drilled, and 1.00 mm aluminum wire was inserted into the holes. Only one adhesive was successful: Loctite L-263, a high strength anaerobic thread sealant consistently sealed the gaps between 0.06-0.99 mm. In each test (Figure 65), Loctite 263 was applied to 6 wires with the same gap and cured. The part was pressurized to 3.4 MPa and temperature increased to 90°C for multiple hours without leaks. Five total tests with Loctite 263 were successful. The tests were cumulative on the same cube, i.e., the first test endured pressure / temperature 5 times. There were no failures, and this adhesive was chosen to attempt leak repair on the HX.

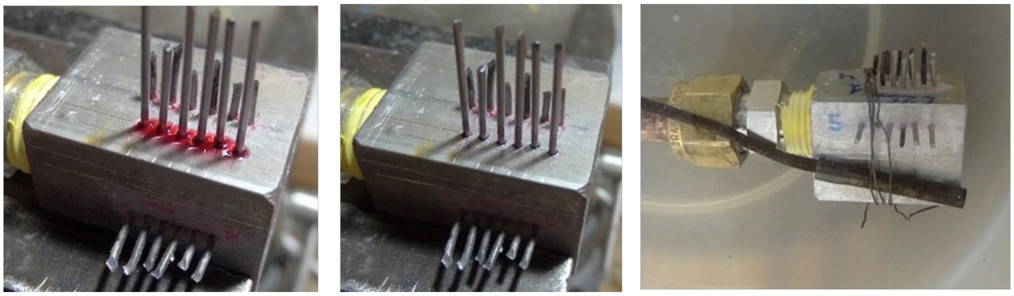

Figure 65: Adhesive leak repair test: (Left) Pre-curing; (Middle) Post-curing; (Right) Pressure test.

To attempt to fix the leaks, the headers were first cleaned with acetone. Loctite 263 was applied along both sides of the entire header (top images of Figure 66), and good adhesive penetration into the whole header depth was observed. The adhesive was allowed to cure for 48 hours, and the same procedure was then done for the other header. During the next pressure test (bottom image of Figure 66), some leaks were found to be sealed, while others were not. Additionally, new leaks (tube-to-header and tank-to-header) were discovered.

Figure 66: Adhesive leak repair #1: (Top) Adhesive application; (Bottom) Leak test.

To improve adhesive penetration into the remaining leaking gaps, vacuum (1020 microns) was applied to the HX while the adhesive cured. Additionally, the HX was put in a bag with oxygen-absorbing sachets. The bag was then vacuumed to remove as much air as possible, and left for 24 hours to cure. This was mostly successful, as only a few very small tube-to-header leaks remained (Figure 67).

Figure 67: Adhesive leak repair and pressure test #2 showing small leaks.

To accelerate the testing schedule, the project team agreed to introduce an EasySeal compound inside the HX and circulate it through the system to seal the remaining HX leaks. Prior to this, a pressure test to operating pressure was deemed necessary. The HX failed at 2.7 MPa (400 PSI), below the target pressure of 3.4 MPa (500 PSI), resulting in the tank separating from the header (Figure 68). With the tank separated from the header, it can be seen that there is no braze fillet between the tubes and the header on the inside. Additionally, the tank to header joint line also shows only partial braze. Overall, there were good braze fillets around the tubes on the outside of the header, but no braze fillets could be found around the tubes inside the tank. Additionally, there was a weak tank to header braze. The adhesive leak repairs were mostly successful, but due to a poor braze, the HX did not hold the required pressure and failed.

Figure 68: Aluminum HX post-pressure test: (Top) Tank-header joint failure; (Bottom) Poor brazed interfaces between tube-header and header-tank.

Summary of Aluminum HX Prototype Manufacturing & Repair

In summary, the HX was not brazed properly at Diesel Radiator, causing multiple tube-to-header and header-to-tank leaks, and ultimately failure below the required pressure. Due to time constraints, nearing the end of the project extension, a replacement HX could not be built.

Component & System-Level Experimental Testing (M3.3, G/NG#2, M4.3)

The experimental efforts for this project are listed below. A detailed report on each effort is included in the following section.

- (M3.3) A HX test facility was constructed for component-level testing and experimental validation of the optimization framework.
- (G/NG#2) Nine (9) in-house experiments on six (6) HX prototypes were completed: (i-ii) 2 radiator (water), (iii-v) 3 condenser (R134a, R410A), (vi-ix) 4 evaporator (R134a, R410A)). Additionally, one HX prototype (R410A evaporator) was sent to an industry partner for independent component-level validation and feedback.
- (M4.3) Preparation of a test facility for system-level tests and experimental testing of a state-of-the-art packaged unit A/C system provided by an industry partner to validate system energy efficiency and charge reduction potential when the system was retrofitted with an evaporator designed in M4.2.

Heat Exchanger Component-Level Experimental Testing

Note: The contents of this section have been published in the following citations: Tancabel et al. [3]; Klein [5].

In this project, nine (9) in-house experiments were conducted to assess the component-level performance of six (6) HX prototypes. A full summary of the test data can be found at the end of this section. For the sake of brevity, two of the nine experimental validations are discussed in detail to go along with explanations of the experimental methods (e.g., setup, uncertainty, data reduction, procedure).

Experimental Setup & Experimental Uncertainty

The experimental test facility consists of a closed-loop wind tunnel, a pumped refrigerant loop, and a data acquisition system (DAQ). The closed-loop wind tunnel is an ASHRAE standard-compliant (33, 41.1, 41.2, 41.3, 41.6) wind tunnel test facility [198-202] with a test capacity range from 500 W to 10 kW (Figure 69). The airside mass flow rate is measured using a seven-nozzle grid which was calibrated under the procedure described in ASHRAE Standard 41.2 [200]. Air sampling trees with an in-line 1/10 DIN RTD and chilled mirror hygrometer were located before and after the HX test section to obtain air temperature and dew point. An air mixer and air straightener ensure a uniform flow and temperature at the plane of the air sampling tree. The HX inlet air temperature and humidity are controlled by a cooling coil, heating coil, dehumidification coil, and humidifier. To measure the HX airside pressure drop, a differential pressure transducer was used with four pressure taps directly before and after the HX.

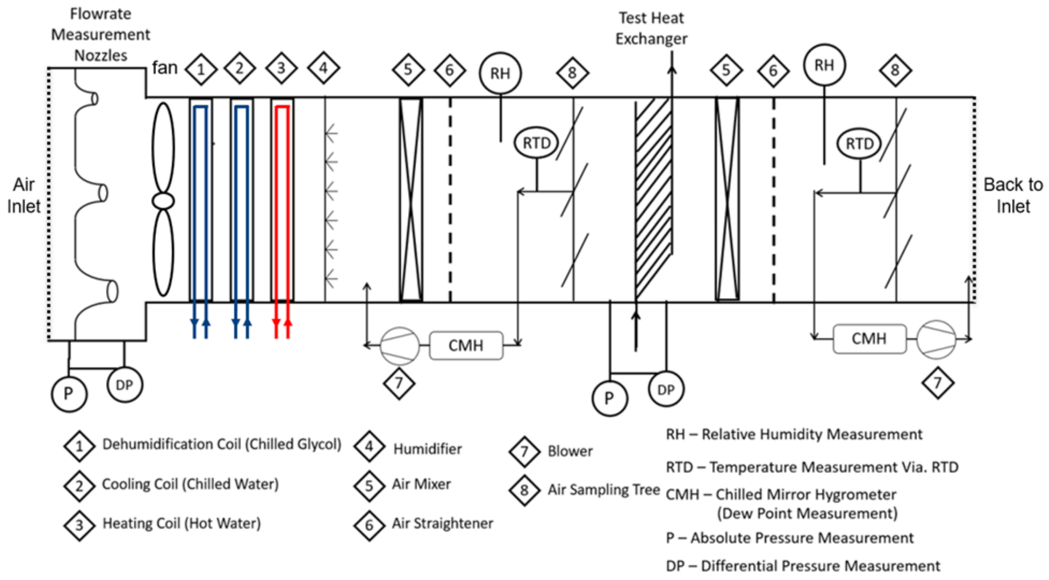

Figure 69: Schematic of closed loop wind tunnel.

The refrigerant flow is controlled by a pumped refrigerant loop (Figure 70) with a capacity range of 500 W to 10 kW to match the wind tunnel facility. A column of subcooled liquid refrigerant created at the diaphragm pump inlet is passed through a Coriolis mass flow meter to measure the refrigerant mass flow rate. The subcooled refrigerant state point (temperature and pressure) is measured before entering a resistance heater, where a wattmeter measures the power input to the refrigerant. The refrigerant state points (temperature and absolute pressure) are measured immediately before the HX inlet and after the HX outlet, along with the differential pressure. The DAQ began recording data for thirty minutes once the entire system reached steady state.

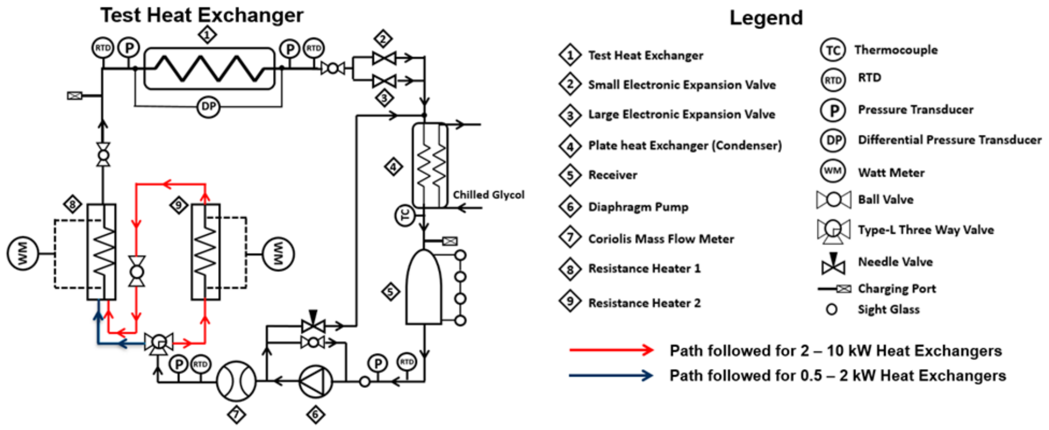

Figure 70: Schematic of pumped refrigerant loop.

A summary of test facility instrumentation and their respective systematic uncertainties are listed in Table 8. An uncertainty propagation analysis following the procedures of ASME PTC 19.1 – 2013 [204] and Moffat [205] was carried out using a coverage factor of 2, and the total experimental uncertainties for pressure drop and capacity are listed in Table 24.

Table 24: HX test facility instrumentation & systematic uncertainty.

System	Instrument	Range	Systematic Uncertainty
Closed Wind Tunnel	1/10 DIN RTD	-200 to 800°C	± 0.03 to 0.07°C
	Barometric Pressure	60 to 110 kPa	± 150 Pa
	Dew Point Sensor	-40 to 60°C	± 0.2°C
	HX Differential Pressure	0 to 249 Pa	± 0.62 Pa
	Nozzle Differential Pressure	0 to 1244 Pa	± 3.11 Pa
	T type Thermocouple	-250 to 350°C	± 0.5°C
Pumped Refrigerant Loop	1/10 DIN RTD	-200 to 800°C	± 0.03 to 0.07°C
	Absolute Pressure	0 to 3447 kPa	± 1.7 kPa
	Coriolis Mass Flow Meter	0 to 500 g/s	± 0.1% of reading
	Differential Pressure	0 to 34.5 kPa	± 0.03 kPa
	T type Thermocouple	-250 to 350°C	± 0.5°C
	Watt Meter	0 – 4 kW	± 20 W
Total airside pressure drop experimental uncertainty			±5.0 to ±47%
Total capacity experimental uncertainty			±1.0%

Data Reduction

The airside and refrigerant-side capacities are measured for each test. The total HX capacity $\left(\dot{Q}\right)$ is taken to be the arithmetic average of the airside and refrigerant-side capacities, as represented in Equation (28). ASHRAE Standard 33 [198] requires that the energy balance (EB) should be within ±5.0% for all experimental tests. The energy balance is defined as in Equation (29).

$$\dot{Q}_{HX} = \frac{\dot{Q}_{air} + \dot{Q}_{ref}}{2}, \tag{28}$$

$$EB = \frac{\dot{Q}_{air} - \dot{Q}_{ref}}{\dot{Q}_{HX}} \times 100\%. \tag{29}$$

A heat loss compensation study was conducted to eliminate the deviation caused by the temperature gradient between the wind tunnel air temperature and the laboratory environmental temperature to improve the experimental energy balance. To ensure a constant temperature gradient throughout the compensation test, the wind tunnel inlet air temperature was set to 35.0°C, and the room temperature was set to 25.0°C. The wind tunnel inlet and outlet air temperatures were then recorded without flowing any refrigerant through the HX. The baseline heat loss can be computed as in Equation (30). During condenser testing, the wind tunnel air temperature would increase across the HX, and the resulting experimental heat loss can be computed using Equation (31).

$$\dot{Q}_{loss,BL} = \dot{m}_{air} \cdot c_{p,air} \cdot \Delta T_{air}. \tag{30}$$

$$\dot{Q}_{loss,expt} = \dot{Q}_{loss,BL} \times \frac{T_{air,out,expt} - T_{air,in,expt}}{T_{air,in,BL} - T_{air,out,BL}}. \tag{31}$$

In this study, both dry and wet condition tests were conducted, and the data reduction methods for each case are explained separately.

Dry Condition

The airside and refrigerant-side capacities under dry conditions can be calculated using Equations (32) and (33), respectively.

$$\dot{Q}_{air,dry} = \dot{m}_{air,dry,in} \cdot c_{p,air,dry} \cdot \Delta T_{air,dry}, \tag{32}$$

$$\dot{Q}_{ref} = \dot{m}_{ref} \cdot \Delta i_{ref}. \tag{33}$$

Wet Condition

The airside capacity calculation under wet conditions is computed using as in Equation (34), while the refrigerant-side capacity is the same as shown in Equation (33).

$$\dot{Q}_{air,wet} = \dot{m}_{air,wet,in} \cdot \Delta i_{air,wet}. \tag{34}$$

<u>Prototype Blockage Testing</u>

Prior to experimental testing, all HXs were subjected to thermal image blockage testing to ensure that the tubes were not blocked, as blocked tubes would compromise the experimental accuracy of the full HX prototype. The blockage testing consisted of flowing chilled isopropyl alcohol through the HX while under the observation of a thermal camera. Time lapse images of two blockage tests for HX prototypes 3-C1 and 6-C3 are shown in Figure 71. A HX proceeds to detailed wind tunnel testing upon passing the blockage test.

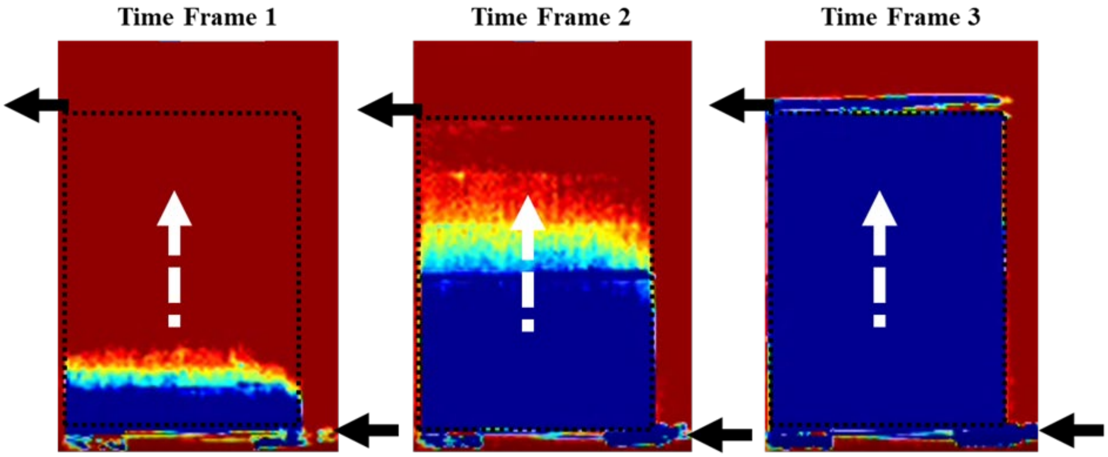

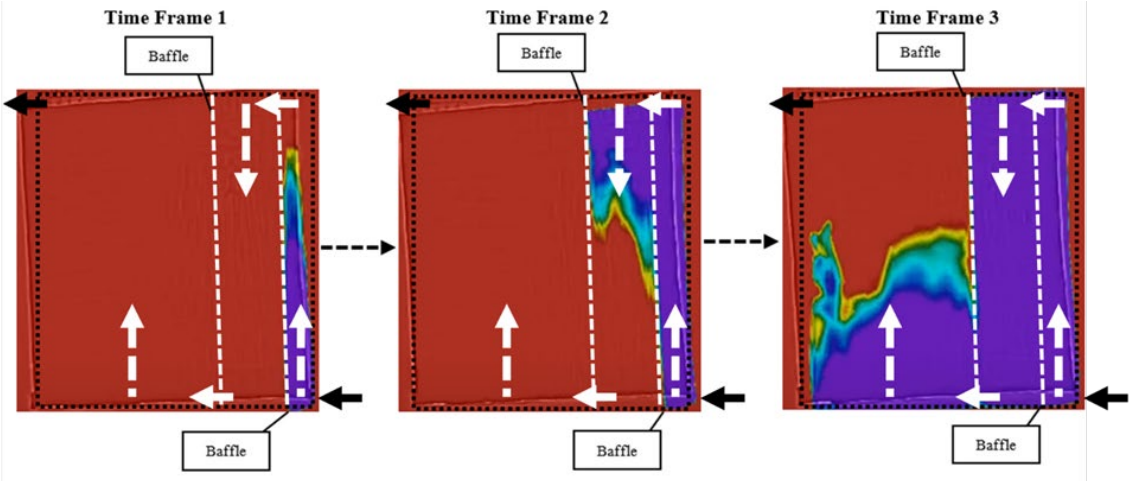

Figure 71: Blockage testing time lapse for (Top) 3-C1 & (Bottom): 6-C3.

Experimental Validation of Prototype 3-C1 “Prototype #1”

Prototype #1 is a 1/16th scale proof-of-concept HX design prototype and is marked with a red circle in Figure 30 – Figure 32. The full-scale design corresponds to a condenser with similar airside pressure drop, but with 25% core envelope volume reduction, 20% face area reduction, and 8% internal volume reduction. The prototype was scaled such that the inlet mass fluxes were kept constant. Thus, prototype scaling is not expected to impact the experimental validation study. This specific HX design was chosen for the following reasons:

- A single-fluid-pass HX has simpler manifolds, i.e., the manifold does not require baffles, which may leak;
- The airside pressure drop is large enough to avoid experimental uncertainty issues; and
- The air volume flow rate is fixed to the same as the baseline value, and the simulated optimal HX has the same airside pressure drop (and thus fan power) as the baseline, i.e., the simulated optimal HX has the same capacity and fan power as the baseline with 25% core envelope volume reduction and 20% face area reduction.

Prototype #1 was tested under steady-state air-to-R410A evaporator conditions under both dry and dehumidifying conditions in accordance with AHRI Standard 210/240 C-Test and A-Test, respectively [181]. For each test condition, twelve data points were collected. The inlet air velocity range was 1.0 – 2.5 ms-1, and the R410A mass flow rate range was selected to ensure an outlet superheat of at least 8.0 K, thus guaranteeing single-phase (vapor) refrigerant at the HX outlet and improving the accuracy of the sensor readings. This corresponded to an R410A mass flow rate of 5.0 – 9.5 gs-1 for the dry condition tests and 7.0 – 11.5 gs-1 for the dehumidifying condition tests. The energy balance for both dry and dehumidifying conditions are shown in Figure 72 and range from -5.5% to -1.0% for the dry condition tests and -2.5% to +5.0% for the dehumidification condition tests.

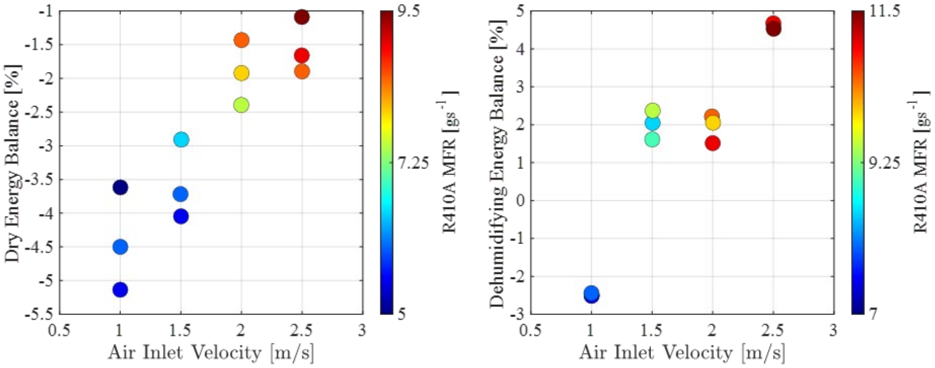

Figure 72: Prototype #1 energy balance: (Left) dry evaporator condition; (Right) dehumidifying condition.

The comparison of simulated and experimental HX performance are shown in Figure 73. For each metric, all values are normalized with respect to the maximum measured or predicted value. For the dry tests, the simulated airside pressure drop overpredicted experimental results by up to 30%, but the deviation decreases significantly as air velocity increases. The dry capacity agreement was excellent, with simulated values matching experimental results within ±10% for all cases.

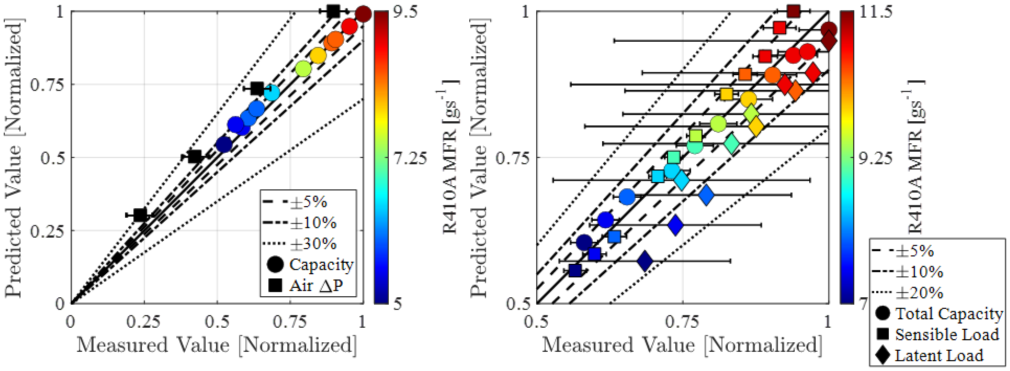

Figure 73: Prototype #1 validation: (Left) dry evaporator capacity & airside pressure drop; (Right) dehumidifying condition capacity.

During wet condition testing, condensing water droplets form “water bridges” between adjacent tubes (Figure 74). Water droplets collected on the spacers, which hold tubes in place during prototype manufacturing, until the larger water droplets “overflowed” down the tube length due to gravity. The water bridges cause additional flow obstruction which is not accounted for during CFD modeling, which assumes dry air conditions. As shown in Figure 74, the water bridge flow obstruction caused the airside pressure drop to increase by a factor of approximately 2.5 across the entire operating range. Nevertheless, the HX simulations predicted the total heat load very accurately, which is promising from a validation standpoint.

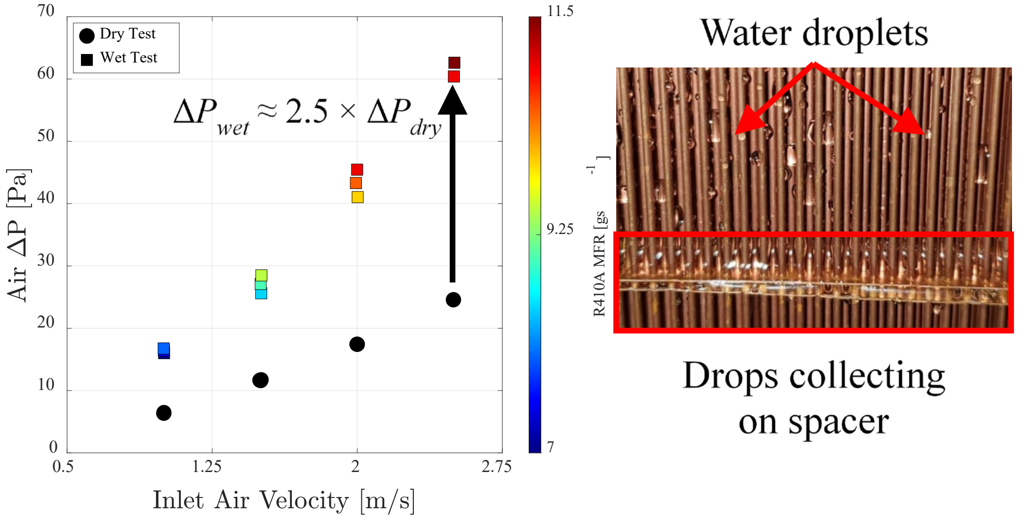

Figure 74: Prototype #1 wet condition experiment: (Left) air pressure drop; (Right); water droplets on HX tubes.

Experimental Validation of Prototype 6-C3 “Prototype #2”

Prototype #2 is a 1/4th scale proof-of-concept HX design prototype and is marked with a green box in Figure 30 – Figure 32. The full-scale design corresponds to a condenser with 35% core envelope volume reduction, 35% airside pressure drop reduction, 9% face area reduction, and 23% internal volume reduction. The prototype was scaled such that the inlet mass fluxes were kept constant. Thus, prototype scaling is not expected to impact the experimental validation study.

Prototype #2 was tested under air-to-R410A condenser conditions for nine (9) steady state points in accordance with AHRI Standard 210/240 A-Test [181]. The air inlet velocity ranged from 0.5 – 2.0 ms-1, while the R410A mass flow rate range was 3.6 – 8.6 gs-1 to ensure an outlet subcooling of at least 5.0 K for all cases and guarantee single-phase (liquid) refrigerant at the HX outlet and improving the accuracy of the sensor readings. Figure 75 shows the energy balance (range from -1.5% to +1.0%) and the comparison of simulated and experimental airside pressure drop and capacity values. As before, the simulated airside pressure drop overpredicted experimental results (up to 27%), but the deviation decreases to within ±10% as air velocity increases. The capacity agreement was excellent, with simulated values matching experimental results within ±3.0% for all cases.

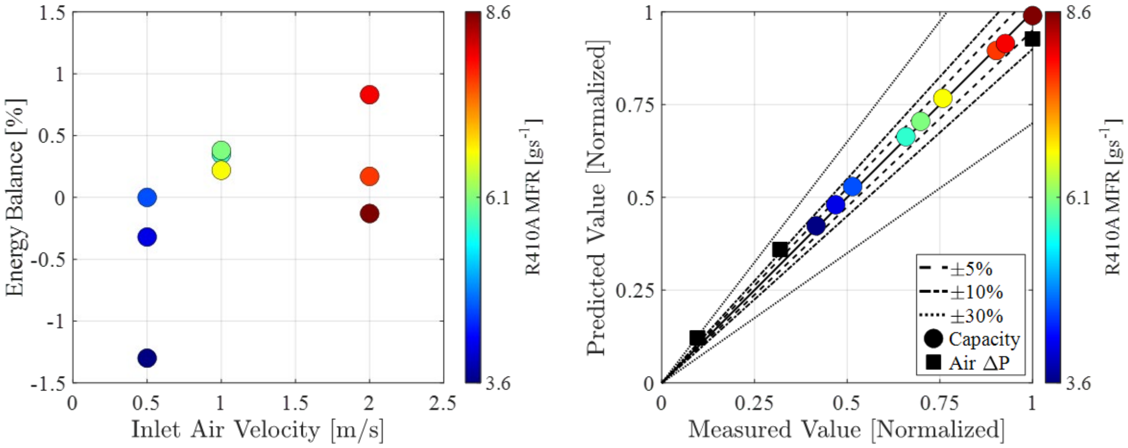

Figure 75: Prototype #2 condenser experimental validation: (Left) energy balance; (Right).

Summary of Component-Level HX Testing and Experimental Validations

In total, nine (9) in-house experiments were conducted to assess the component-level performance of six (6) HX prototypes: (i-ii) 2 radiator (water), (iii-v) 3 condenser (R134a, R410A), (vi-ix) 4 evaporator (R134a, R410A)). A complete summary of the capacity (Figure 76) and airside pressure drop (Figure 77) is shown below. Overall, there was excellent agreement between the predicted and measured performance of all HXs tested, providing strong evidence that this new class of compact finless HXs are performing as intended under typical HVAC&R application conditions. Additionally, it provides evidence that the multi-physics optimization framework presented herein can successfully design high performance HXs with simulated performance within ±10% of the desired performance targets, which will significantly advance the tech-to-market potential of such HXs.

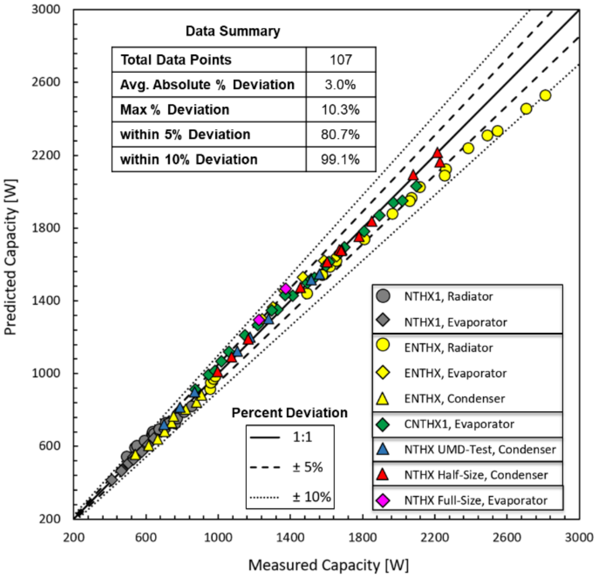

Figure 76: Component-level experimental validation summary: capacity.

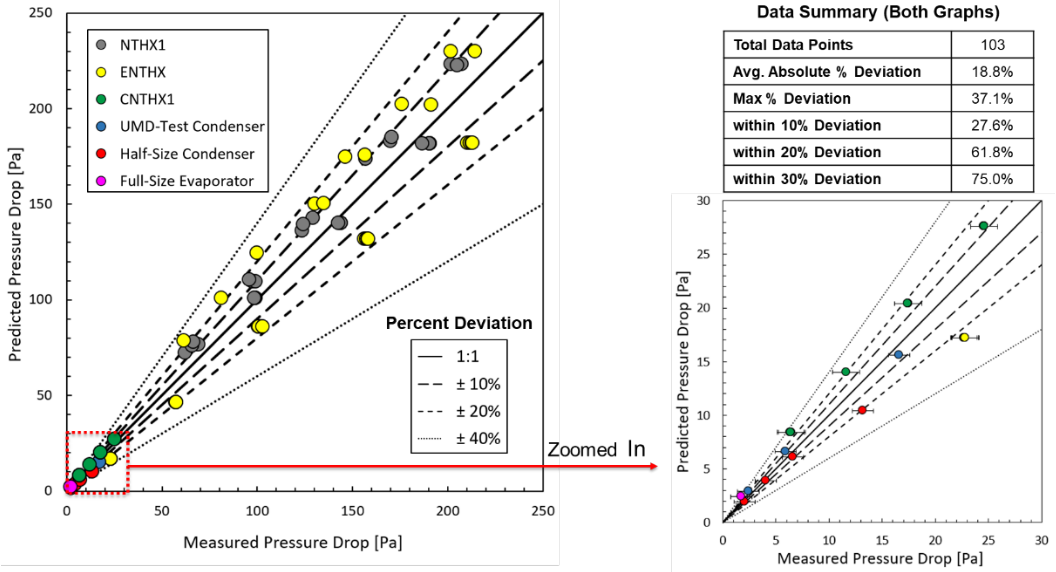

Data Summary (Both Graphs)

Total Data Points	103
Avg. Absolute % Deviation	18.8%
Max % Deviation	37.1%
within 10% Deviation	27.6%
within 20% Deviation	61.8%
within 30% Deviation	75.0%

Figure 77: Component-level experimental validation summary: airside pressure drop.

System-Level Packaged A/C Unit Experimental Testing

Note: The contents of this section have been published in the following citations: Klein [5].

System-level testing was conducted on a commercially-available packaged A/C unit provided to the project team by an industry partner (Figure 78). The packaged A/C unit has a nominal capacity of 8.4 kW, 14 SEER, and uses R410A. A typical application for this unit would be a residential home. The unit has a return and supply air duct openings for the evaporator loop with a single speed fan. A single speed condenser fan draws in air from the side and expels heated air through the top. A divider separates the two air streams. Both the evaporator and condenser are tube-fin heat exchangers, the compressor is single-stage scroll, and the expansion device used is a thermostatic expansion valve (TXV).

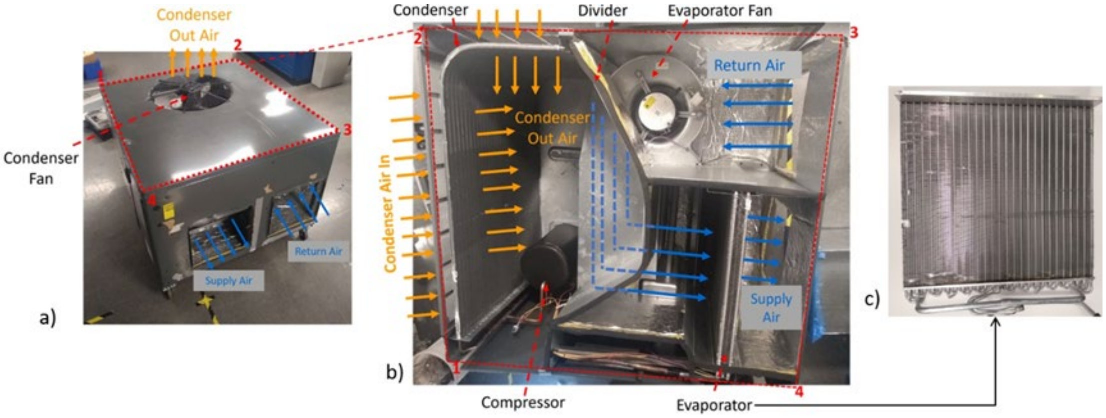

Figure 78: (a) Packaged A/C unit (b) Unit top view without top cover (c) Baseline tube-fin evaporator.

<u>Test Facility Schematics & Instrumentation</u>

A test facility was designed and constructed to evaluate the system level performance of the packaged air conditioning unit at AHRI 210/240 test conditions [181]. Figure 79 shows the ducted closed evaporator loop constructed to evaluate the evaporator's thermal-hydraulic performance. Air flow is driven through the evaporator loop by a single speed fan. The air's dry bulb (DB) temperature, relative humidity, and absolute pressure are measured at the unit's supply and return duct openings. Air-side mass flow rate was measured using the pressure drop across a 17.78 cm (7 in) nozzle based on ASHRAE standard 41.2 [200]. The air was reconditioned to the desired return temperature and relative humidity using a series of resistance heaters and steam humidifier, respectively. External Static Pressure (ESP) across the supply and return was controlled by a variable speed centrifugal fan. Air-side pressure drop was also measured across the evaporator. Figure 79 also shows the condenser air-side schematic and instrumentation. Temperature, relative humidity, and absolute pressure at the inlet of the condenser were measured. Temperature and absolute pressure at the outlet of the condenser fan were measured. The air was then cooled to the desired temperature via an air-to-water HX with variable water flowrate.

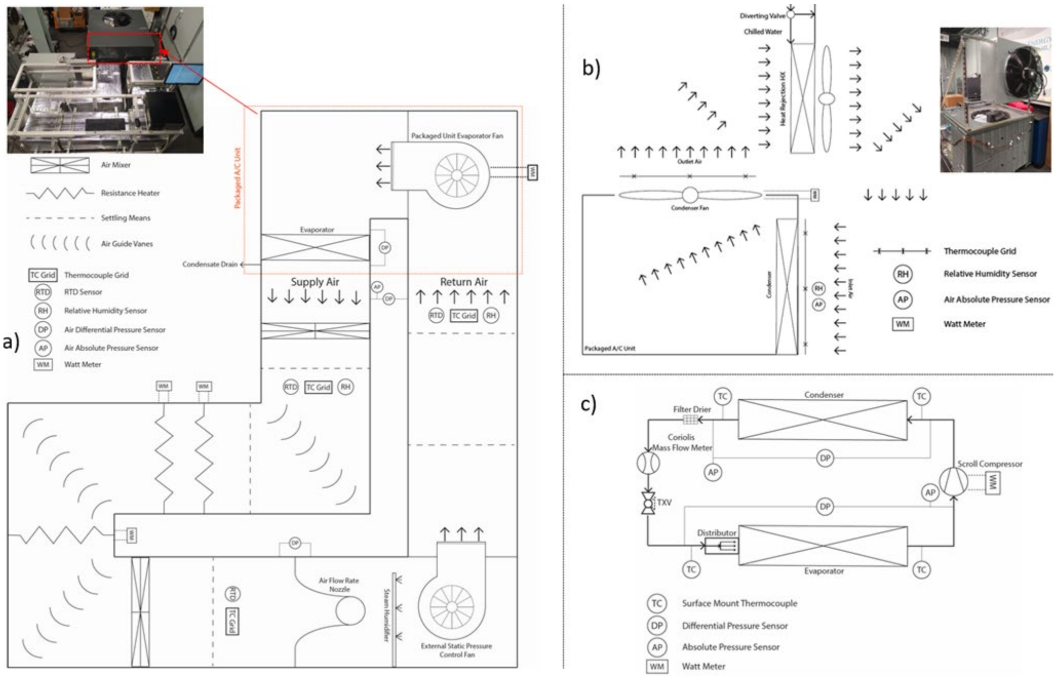

Figure 79: Evaporator closed loop schematic and connection to packaged unit.

The final packaged unit test facility was placed in an environmental chamber as shown in Figure 80. The environmental chamber does not provide any active cooling or de-humidification, but provides an enclosed space for the air-to-water heat ejection heat exchanger to properly control the inlet air temperature of the condenser.

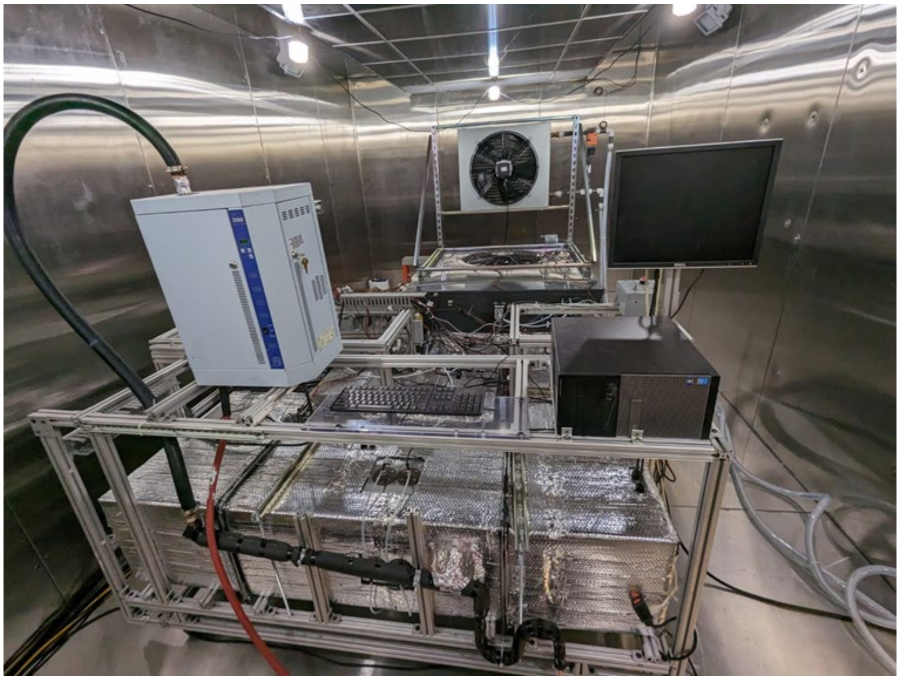

Figure 80: Packaged unit test facility in environmental chamber.

Data Reduction Methodology & Uncertainty

Equation (35) shows the definition of the evaporator's air-side sensible heat ratio (SHR), sensible, total capacity, its refrigerant-side capacity, and average capacity (average between refrigerant-side and air-side capacity). Equation (36) and Equation (37) calculate the evaporator's energy balance and system level COP, respectively. Equation (38) shows the definition for the condenser's air-side mass flow rate and the calculated refrigerant-side capacity. Uncertainty propagation analysis followed performance code ASME 19.1 [203] with a coverage factor of 2. Table 25 shows a summary of the test facility instrumentation uncertainties and uncertainty range for measured system performance parameters.

$$SHR = \frac{\dot{Q}_{e,a,s}}{\dot{Q}_{e,avg}} = \frac{\dot{m}_a \cdot c_{p,avg} \cdot \left(T_{e,a,i} - T_{e,a,o}\right)}{0.5 \cdot \left(\dot{Q}_{e,r} + \dot{Q}_{e,a,total}\right)} = \frac{\dot{m}_a \cdot c_{p,avg} \cdot \left(T_{e,a,i} - T_{e,a,o}\right)}{0.5 \cdot \left(\left[\dot{m}_r \cdot \left(h_{r,o} - h_{r,i}\right) + \dot{m}_a \cdot \left(h_{a,i} - h_{a,o}\right) + \dot{W}_{fan}\right]\right)} \tag{35}$$

$$EB_e = 200\% \times \frac{\left(\dot{Q}_{e,r} - \dot{Q}_{e,a,total}\right)}{\left(\dot{Q}_{e,r} + \dot{Q}_{e,a,total}\right)} \tag{36}$$

$$COP = \frac{\dot{Q}_{e,avg}}{\dot{W}_{unit,total}} \tag{37}$$

$$\dot{m}_{c,a} = \frac{\left(\dot{Q}_{c,r} + \dot{W}_{c,fan}\right)}{c_{p,avg} \cdot \left(T_{c,a,o} - T_{c,a,i}\right)} = \frac{\left(\left[\dot{m}_r \cdot \left(h_{r,i} - h_{r,o}\right)\right] + \dot{W}_{c,fan}\right)}{c_{p,avg} \cdot \left(T_{c,a,o} - T_{c,a,i}\right)} \tag{38}$$

Table 25: Packaged unit test facility instrumentation & systematic uncertainty.

Metric	Measurement	Units	Instrument Type	Instrument or Measured Parameter Range	Uncertainty Range
Air	Temperature	°C	Type T Thermocouple	-250 to 35	±0.5
			1/10 DIN RTD	-200 to 800	±0.03 to 0.07
	Barometric Pressure	kPa	Strain	80 to 110	±0.06
	ESP and Evap. ΔP	Pa	Strain	0 to 248.8	±1.00
	Nozzle ΔP	Pa	Strain	0 to 622.1	±2.49
	Relative Humidity	%	Thin Film Capacitance	0 to 100%	±1.0% F.S.
R410A	Mass Flow Meter	g/s	Coriolis	0 to 606	±0.1 % of Reading
	Temperature	°C	Type T Thermocouple	-250 to 350	±0.5
	Absolute Pressure	kPa	Strain	0 to 3447	±1.72
	ΔP	kPa	Strain	0 to 103.4	±0.43
Power Consumption	Total Unit	kW	Hall Effect	0 to 20	±0.5% of Reading
	Evap & Cond Fan, Compressor	kW	Hall Effect	0 to 4	±0.2 % of Reading
	Resistance Heater	kW	Hall Effect	0 to 4	±20
Measured Performance Parameters	Evap. VFR	m^3/s	-	0.467 to 0.484	±0.02
	Evap. Avg. Q	kW	-	8.12 to 10.15	±0.57
	SHR	-	-	0.67 to 0.78	±0.04
	COP	-	-	3.25 to 4.62	±0.23 to 0.27
	R410A Charge	kg	-	2.01 to 2.36	±0.11
	Cond. Q	kW	-	9.54 to 11.38	±0.3
	Cond. VFR	m^3/s	-	1.40 to 1.45	±0.1

HX Prototype Overview & Retrofitting Considerations

NTHX prototype 10-E2 (NTHX-Full Size Evaporator, NTHX-FSE) is an air-to-R410A evaporator with a nominal capacity of 5.3 kW (1.5-Tons) optimized by the framework discussed herein. Note that this system is a nominal 8.4 kW capacity unit, and thus the evaporator used for testing is slightly undersized. A new evaporator could not be prototyped within the project timeline due to logistical challenges related to parts procurement, and thus system testing was required to proceed with this undersized evaporator. Figure 81 shows the prototype, a representative (not exact) cross section of its shape and topology optimized non-round bare tube core, and its installation configuration and into the A/C unit. It was installed in the same location as the baseline tube-fin evaporator.

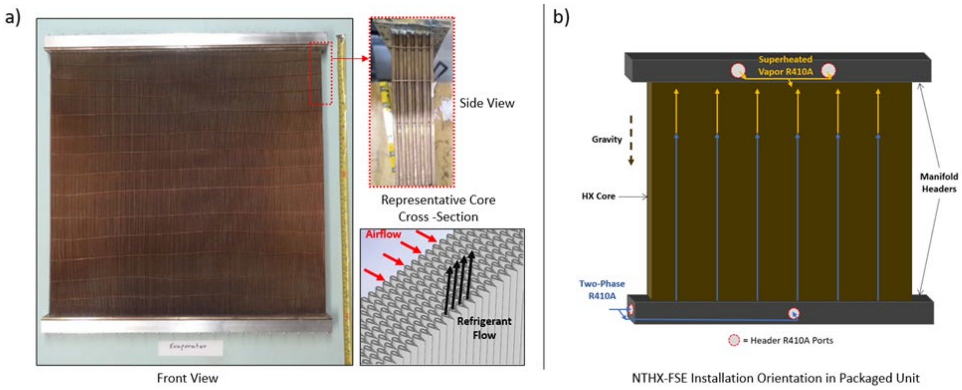

Figure 81: (a) NTHX-FSE overview including front and side views and CAD rendering; (b) Installation orientation in packaged unit.

To facilitate the evaporator retrofit into the packaged unit, a number of design changes were made from the component-level testing, as listed below:

- Leaking gasket replaced with new gasket.
- The single vapor outlet port was replaced with two larger outlet ports (Figure 82). The new outlet port refrigerant cross-sectional area is now ~70-75% (previously 15-20%) of the baseline evaporator outlet port cross-sectional area. This will drastically reduce the refrigerant-side pressure drop in the outlet header.
- A back-up refrigerant inlet port was installed in the center of the inlet manifold (Figure 82) that can be utilized if the primary refrigerant inlet port is causing refrigerant maldistribution. The back-up inlet port is toggled using a ball valve (Figure 82).

Following the HX installation, the packaged unit was pressure tested to 175 psig for 4 days with nitrogen. The system held pressure for the full duration, and thus the system advanced to performance testing.

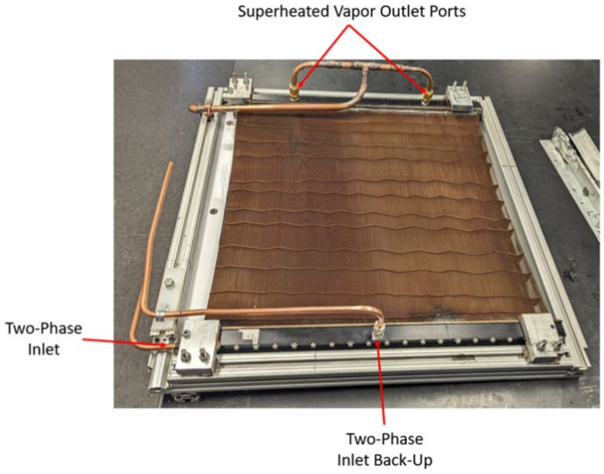

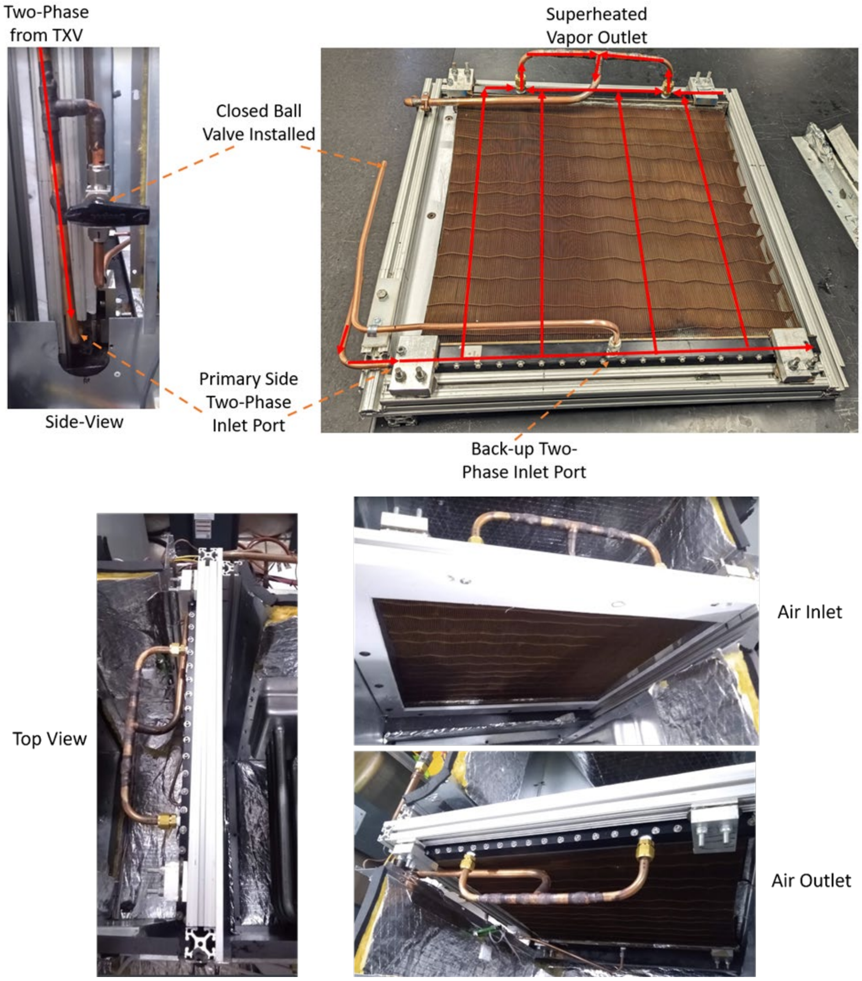

Figure 82: Modified NTHX-FSE: (Top) New inlet and outlet refrigerant ports; (Middle) Flow path; (Bottom) Installed in packaged unit.

Packaged Unit Experimental Testing & Results

The Packaged A/C unit's air-side testing conditions were based on AHRI Standard 210/240 standard [181] and the test matrix and conditions are shown in Table 26.

Table 26: Packaged unit AHRI 210/240 testing conditions [181].

	Baseline Unit		**Retrofitted Unit**	
AHRI 210/240 Test Type	A_{full}	B_{full}	A_{full}	B_{full}
Evaporator Fan Speed	Full	Full	Full	Full
External Static Pressure [Pa, in H_2O]	124.4, 0.5	124.4, 0.5	124.4, 0.5	124.4, 0.5
Evaporator Loop Air Return Temp. (Dry Bulb/Wet Bulb) [°C]	26.7/19.4	26.7/19.4	26.7/19.4	26.7/19.4
Condenser Air Inlet Temp. (Dry Bulb/Wet Bulb) [°C]	35/23.9	27.8/18.3	35/23.9	27.8/18.3
Compressor Speed	Full	Full	Full	Full

The packaged unit was first tested at AHRI A and B test conditions with the baseline evaporator. All steady-state tests were 50-60 minutes in length. R410A charge was determined according to AHRI standard 210/240 [181] for systems with a TXV as follows: Steady state A conditions were reached with ~60-70% of rated factory charge; R410A was added until at least 5.6 K subcooling was reached; the TXV was adjusted until at least 4.0 K superheat was reached while still maintaining at least 5.6 K subcooling. The charge was not changed for B test condition. Once baseline testing was completed, the baseline evaporator was then replaced with the NTHX-FSE prototype and tested at AHRI A test conditions only. Table 27 shows a summary of the experimental performance under AHRI test conditions. Note, the last column shows the change in performance before and after the retrofit for AHRI A test only due to the prototype HX beginning to leak refrigerant while the AHRI B test experiment was being conducted.

Table 27: Packaged unit test facility instrumentation & systematic uncertainty.

Measured Parameters			**Units**	**Baseline (AHRI B)**	**Baseline (AHRI A)**	**Retrofit (AHRI A)**	**Difference (AHRI A)**
Evaporator	Airside	VFR	m^3/s	0.468	0.467	0.484	+3.7%
	Airside	ΔP	Pa	30.18	29.48	17.55	-40.5%
	Airside	SHR	-	0.74	0.78	0.67	-0.11pts.
	Fan	Power Consumption	W	227.6	225.7	224.1	-0.7%
	R410A	ΔP (Evap. + Suction Line)	kPa	63.8	75.0	32.6	-56.6%
	R410A	Outlet Pressure	kPa	1071	1098	962	-135 kPa
	R410A	Superheat	K	6.0	5.5	9.1	+3.7 K
	Average	Q	kW	10.15	9.12	8.12	-11.0%
	-	Energy Balance	%	-4.5	+2.6	-6.8	N/A
Condenser	Airside	VFR	m^3/s	1.45	1.42	1.40	-1.5%
	Fan	Power Consumption	W	277.5	271.9	270.0	-0.7%
	R410A	Outlet Pressure	kPa	2341	2786	2680	-106 kPa
	R410A	Subcooling	K	7.8	7.6	6.0	-1.6 K
	R410A	Q	kW	11.38	10.98	9.54	-13.1%
Compressor		Mass Flow Rate	g/s	54.7	55.0	45.9	-16.5%
		Power Consumption	kW	1.68	2.01	1.98	-1.5%
System-Level Metrics		Total Power Consumption	kW	2.20	2.53	2.50	-1.3%
		COP	-	4.62 ± 0.27	3.60 ± 0.23	3.25 ± 0.23	-9.8%
		R410A Charge	kg	2.36	2.36	2.01	-14.8%

The energy balance between the evaporator's measured air-side and refrigerant-side capacity was always less the 7% in magnitude, indicating good agreement. The A/C unit's cooling capacity and COP decreased by 11% and 10%, respectively, at AHRI A conditions after NTHX-FSE replaced the baseline evaporator. This could be due to multiple factors

- NTHX-FSE was originally optimized to serve as a replacement to a nominal 5.3 kW (1.5-Ton) R410A evaporator. However, the evaporator is being used in a nominal 8.4 kW (2.4-Ton) system. Thus, NTHX-FSE is undersized for the application.
- Next, it is likely there is refrigerant maldistribution due to the oversized aluminum header manifolds.

- Lastly, the SHR was significantly lower (-0.11 pts.) compared to the baseline evaporator indicating a higher latent load and severe condensate build-up within the tube bundle core.

A consequence of the undersized evaporator, refrigerant maldistribution, and high condensate build-up was that the R410A evaporation pressure was 135 kPa lower as the TXV attempted to increase the temperature difference between the air and refrigerant. This caused the R410A suction line density to decrease and resulted in a 17% lower R410A mass flow rate. Air-side and refrigerant-side evaporator pressure dropped by 41% and 57% over the baseline, respectively. NTHX-FSE's retrofit facilitated a R410A charge reduction of 15%. If not for NTHX-FSE's oversized headers, the charge reduction would have been greater. Reducing the header size will help realize a higher reduction in R410A charge. It is recommended to focus on re-designing the headers to further reduce the evaporator's total internal volume and refrigerant charge and mitigate refrigerant maldistribution, as well as investigate methods to reduce condensate retention in the HX core.

Packaged Unit Simulation, Experimental Validation, & Retrofit Analysis

Baseline System Modeling & Experimental Validation

The A/C system was simulated using an experimentally validated, component-model based steady-state simulation tool [205]. First, the baseline simulation model (e.g., baseline compressor, THX, condenser, and evaporator, Figure 83) was calibrated using the results from AHRI Standard 210/240 A and B tests [181] using industry-standard correction methods, e.g., (i) compressor power and refrigerant mass flow rate correction as a linear function of pressure ratio, and (ii) excess charge correction as a linear function of simulated condenser liquid length [96]. The convergence criteria are the experimental superheat and subcooling values. Results of the baseline experimental validation are summarized in Table 28. The excellent experimental validation of the calibrated baseline model gives confidence that retrofitting the HX components will give good predictions of simulated system performance for a drop-in retrofit of the optimum HXs.

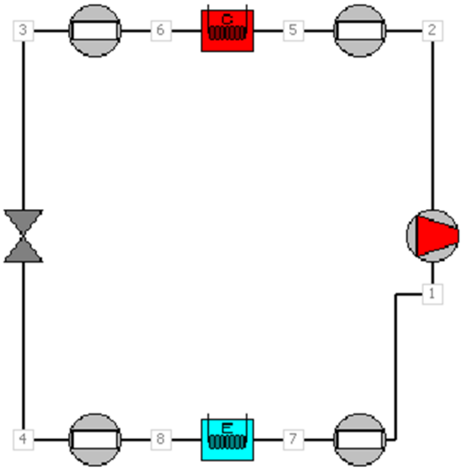

Figure 83: Schematic of system model.

Table 28: Baseline packaged unit experimental validation.

AHRI Test	System Configuration (Experiment / Model)	COP	Q	SHR	System Power	Evaporator Pressure	Low-side ΔP (Evap+Suction Line)	Charge
-	-	NORM	NORM	-	NORM	kPa	Normalized	NORM
A	Baseline System (Experiment)	1.00	1.00	0.78	1.00	1089	1.00	1.00
	Baseline System (Simulation)	0.992	1.008	0.76	0.988	1154	0.315	1.00
	Difference	-0.8%	+0.8%	-2% pts.	-1.2%	+65	-68.5%	0%
B	Baseline System (Experiment)	1.00	1.00	0.74	1.00	1135	1.00	1.00
	Baseline System (Simulation)	0.955	0.972	0.74	0.995	1128	0.353	1.00
	Difference	-4.5%	-2.8%	0% pts.	-0.5%	-7	-64.7%	0%

Retrofitted System Simulation Analysis

The system model was then used to simulate two different configurations (i) NTHX-FSE evaporator retrofit only with all other components the same as the baseline and (ii) both NTHX condenser and NTHX-FSE evaporator retrofitted. A comparison of the baseline system HXs with the optimal NTHXs used for full retrofit (simulation-based only) is summarized in Table 29. It is clear that the optimal HXs are significantly smaller than the baseline tube-fin HXs. Additionally, note that the core weight reductions are on the order of 20%, satisfying the project goals.

Table 29: HX-level comparison: Packaged unit HXs vs. optimal NTHXs.

HX	Version	Core Envelope Volume	Core Internal Volume	Core Material Volume	Airside HT Area	Core Weight	Comments
[-]	[-]	[-]	[-]	[-]	[-]	[-]	[-]
Condenser	Baseline	1.00	1.00	1.00	1.00	1.00	• Cu tube / Al fin
	NTHX1	0.485	0.449	1.076	0.312	0.793	• All Al HX (tubes + headers) • Headers not included
Percent Difference		51.5%↓	55.1%↓	7.6%↑	68.8%↓	20.7%↓	N/A
Evaporator	Baseline	1.00	1.00	1.00	1.00	1.00	• All Al HX (tubes + fins)
	NTHX1	0.445	0.294	0.808	0.348	2.68 (Cu) 0.808 (Al)	• All Cu HX (tubes + headers) • Headers not included • All Al HX → ~19% lighter
Percent Difference		55.5%↓	70.5%↓	19.2%↓	65.2%↓	168%↑ (Cu) 19.2%↓ (Al)	N/A

The simulation results of NTHX-FSE only retrofit and fully retrofitted (NTHX-FSE and NTHX condenser) performance are presented in Table 30 and Table 31, respectively. Table 30 indicates good agreement between experimental and simulation results at AHRI A conditions with NTHX-FSE retrofitted COP, cooling capacity, power, and charge all predicted within 10%. Simulated SHR, evaporator pressure drop, and evaporator pressure are all higher than simulated results. System model results from Table 31 indicate that retrofitting the packaged A/C unit with both new HXs can potentially result in significant refrigerant charge reductions of up to 60% with slight cooling capacity and COP reduction of 7-10% and 4-7%, respectively. The charge reduction is largely due to the internal volume reductions resulting from significant refrigerant-side hydraulic diameter reductions (~75-90%) compared to the baseline round tubes. Additionally, a properly sized evaporator is expected to facilitate a COP improvement of up to 10-15% compared to the baseline system. A multi-pass condenser with a subcooling pass could further reduce HX size, weight, and charge, thus enabling improved system performance.

Table 30: Evaporator-retrofitted packaged unit simulation results.

AHRI Test	System Configuration (Experiment / Model)	COP	Q	SHR	System Power	Evaporator Pressure	Low-side ΔP (Evap+Suction Line)	Charge
-	**-**	**NORM**	**NORM**	**-**	**NORM**	**kPa**	**Normalized**	**NORM**
A	Evap. Retrofit System (Experiment)	1.00	1.00	0.67	1.00	962	1.00	1.00
	Evap. Retrofit System (Simulation)	1.062	1.075	0.74	0.98	1143	1.81	1.10
	Difference	+6.2%	+7.5%	+7% pts.	-2%	+181	+81%	+10%
B	Baseline System (Experiment)	1.00	1.00	0.74	1.00	1128	1.00	1.00
	Evap. Retrofit System (Simulation)	0.973	0.967	0.72	1.00	1136	2.84	0.962
	Difference	-2.7%	-3.3%	-2% pts.	0%	+8	+184%	-3.8%

Table 31: Fully retrofitted (Condenser + Evaporator) packaged unit simulation results.

AHRI Test	System Configuration (Experiment / Model)	COP	Q	SHR	System Power	Evaporator Pressure	Low-side ΔP (Evap+Suction Line)	Charge
-	**-**	**NORM**	**NORM**	**-**	**NORM**	**kPa**	**Normalized**	**NORM**
A	Baseline System (Simulation)	1.00	1.00	0.78	1.00	1098	1.0	1.00
	Full Retrofit System (Simulation)	0.928	0.959	0.75	1.004	1163	0.840	0.385
	Difference	-7.2%	-4.1%	-3% pts.	+0.4%	+65	-16.0%	-61.4%
B	Baseline System (Simulation)	1.00	1.00	0.74	1.00	1135	1.00	1.00
	Full Retrofit System (Simulation)	0.896	0.928	0.73	1.014	1139	0.986	0.398
	Difference	-10.4%	-7.2%	-1% pts.	+1.4%	+4	-1.4%	-60.2%

Significant Accomplishments and Conclusions

Heat Exchanger Analysis, Modeling, & Optimization

- A new comprehensive and experimentally validated air-to-refrigerant HX optimization framework with simultaneous thermal-hydraulic performance and mechanical considerations for novel, non-round, shape- and topology-optimized tubes.
- Capable of designing single and two-phase HXs (i.e., radiators, condensers, and evaporators) for any refrigerant choice and/or operating requirements with significant engineering time savings compared to conventional design practices.
- Accelerate design and time to market for next generation HXs.
- Facilitate industry transition to new refrigerants at lower charge.
- Comprehensive body of knowledge for multi-physics performance of non-round tube bundles, including:
    - tube-level mechanical performance for static and fatigue loading (targeting manufacturing challenges, e.g., burst pressure product qualification testing),
    - aeroacoustics generated noise performance (targeting operational challenges resulting from noise & vibration), and
    - internal flow thermal-hydraulic performance (targeting novelty challenges, e.g., >20% performance improvements).
    - First to conduct comprehensive simulations of non-round tube bundle dehumidification
        - Verification that existing dehumidification modeling assumptions for Lewis number, originally formulated for tube-fin HXs with diameters > 7.0 mm, remain somewhat valid for small diameter, finless tube bundles using shape-and-topology optimized tubes.
    - Development of experimentally-validated CFD-based Lewis number correlations for three (conventionally manufactured) non-round tube bundle geometries with improved prediction accuracy compared to existing Lewis number correlations in literature.
- The framework was utilized to develop novel HXs a wide variety of refrigerants, including conventional refrigerants (R410A), next generation replacement refrigerants (R32, R454B), and low-GWP and natural refrigerants (R290, supercritical carbon dioxide (sCO2)), and applications (A/C system, heat pump system, gas coolers). These HXs consistently met the following design targets compared to commercially available, high performance HXs for stationary systems:
    - >20% weight reduction;
    - >20% envelope volume reduction; and
    - >25% refrigerant charge reduction.

Heat Exchanger Manufacturing

This project resulted in ten HX prototypes which utilize non-round tube shapes; nine HXs were prototyped utilizing conventional manufacturing methods developed as a result of this project while one HX was prototyped using additive manufacturing methods. One additional HX prototyping effort for an all-aluminum HX was attempted to enable complete retrofit of a commercially-available packaged A/C unit. Unfortunately, the braze failed, and the HX ruptured during a burst pressure test.

Additionally, design knowhow and novel manufacturing methods were developed for non-round tubes and tube-header joints which could enable industry-scale mass-manufacturing of non-round tube HXs, as outlined below:

- Copper tube manufacturing
  - The production of non-round copper tubes was successful after a few iterations by the manufacturer to eliminate bow and twist on the tubes.
- Copper tube HX manufacturing
  - Developed a copper HX manufacturing process which is suitable for manufacturing with some additional improvements learned:
  - Out of many thousands of tube-solder casts, only a handful of leaks appeared and were easily repaired by fluxing and re-melting the solder in that location.
  - The solder cast to brass header (interface) leaks were the area with the majority of the leaks.
  - Casting of Sn-Ag solder into the header cavity could be significantly improved and leaks eliminated by the following:
    - The brass header could be pre-tinned with solder, which may eliminate interface leaks entirely.
    - The HX core could be pre-heated to avoid prematurely solidifying the solder, which will prevent bubbles and cavities being trapped below the tube ends in the cavity.
- Aluminum tube manufacturing
  - The production of aluminum non-round tubes was successful. Thousands of perfect tubes were produced by the extruder without issues. The tubes were straight, rigid, had no burr at the ends and held excellent tolerance from first extrusion to last.
- Aluminum HX manufacturing
  - The aluminum HX manufacturing process described above is suitable for manufacturing with some additional improvements learned.
  - Brazing of such HX requires additional study and further braze tests. The project team and brazing experts in industry are confident that such HX can be successfully brazed.
  - The assembly methods developed during this project are applicable to manufacturing.
  - Brazing optimization process for subsequent braze tests should include the following:
    - Increasing vacuum time to remove trapped oxygen from thousands of small tubes which are ~1 m long (or potentially longer).
    - Determine best ramp and soak time to allow the frame (relatively heavier than tubes) to heat up at similar rate as the tube bundle.

        - Determine soak time to allow clad layer to wet all parts properly, including inside the tanks and all frame parts.
- Other methods for cutting headers holes
    - Wire EDM is the most accurate method to cut the non-round holes with the required accuracy for brazing, and with holes that have the same entry and exit dimensions.
    - Another option is the sinker EDM method, where an electrode in the shape of the teardrop hole “sinks” into the header should be investigated as a faster and possibly cheaper alternative.
- Adhesive casting of manifolds
    - Adhesive casting of manifolds could work for evaporator use (low temperature/pressure) but at this time, not for the condenser (high temperature/pressure). Adhesive development specific for this application for use in condensers is required.
- Final Remarks on HX Manufacturing
    - The effort for developing the manufacturing processes for each of the HX material types and the making these HXs was greater than anticipated, but a rewarding experience. We hope that the industry will adopt these processes for the production of smaller, more efficient heat exchangers in energy-efficient products.

Component & System-Level Experimental Testing

- Six different HX prototypes experimentally tested over project duration under radiator, condenser, and evaporator conditions.
    - Capacity predicted within +/- 10%.
    - Air-side pressure drop predicted within +/- 40%.
- NTHX-FSE functionality confirmed at UMD and tested independently by industry partner.
    - Evaporator performance agrees within 10% of predicted values and performance data from CEEE lab
- Test facility capable of evaluating comprehensive system level performance of packaged air conditioning unit constructed.
    - Baseline Fin-Tube Evaporator Experimental Performance
        - Capacity and COP of unit predicted within ±5%.
    - NTHX Full Size Evaporator Experimental Performance
        - COP and total cooling capacity decreased by 9.7% & 11%.
        - R410A refrigerant charge decreased by 15%.
        - Condensate bridging and refrigerant maldistribution more severe than anticipated.

Path Forward

Multiple potential avenues for future work have resulted from this work. These are summarized for all three research thrusts (HX analysis, modeling, & optimization; manufacturing; experimental studies) as below.

Heat Exchanger Analysis, Modeling, & Optimization

- Improvement of proposed Lewis number correlations to a fully generalized case, i.e., comprehensive tube shape and topology optimization, larger operating range (inlet air temperatures, relative humidity values, and velocities; more tube wall temperatures, etc.)
- Comprehensive modeling of variable geometry bundles, i.e., all tubes are located in any location on an arbitrary canvas, where each tube shape / size may be different, and some tubes may be finned or finless.
  - Dry & wet condition airside thermal-hydraulic performance characterization (i.e., heat transfer coefficient, pressure drop, Lewis number)
  - Aeroacoustics performance characterization
  - Fatigue performance characterization
- Address additional physics not considered herein which may have unforeseen impacts on HX performance and lifespan, including:
  - Surface inhibitors, e.g., fouling / frosting and corrosion
  - Tube vibrations from fluid-structural interactions (airside and internal fluid side)
  - Two-phase internal flow thermal-hydraulic performance to ensure that existing two-phase flow correlations are valid for non-round tube shapes with small characteristic diameters.
  - Refrigerant-side maldistribution and combined air / refrigerant maldistribution cases.
  - Integration of fans and/or blowers to properly account for the actual airside inlet velocity profiles.
- Extending HX optimization capabilities beyond single, fixed inlet component-level optimization. For example:
  - Component-level optimization considering multiple HX operating conditions, i.e., consider multiple operating conditions / design targets (e.g., capacity, pressure drop).
  - System-level context optimization, e.g., for a simple four-component vapor compression system, optimize the HX pair (condenser / evaporator) at the same time to maximize system-level metrics (COP, charge, etc.)
  - Integrating circuitry optimization methodologies (e.g., [230]–[233]) to further improve HX performance.

Heat Exchanger Manufacturing

- Addressing challenges with copper tube HX leaks, esp. (i) tube-to-solder leaks and (ii) solder-to-brass header (interface) leaks.
- Adhesive casting for headers/ tanks is a promising option for manufacturing such HX since it involves (i) no EDM cutting process, (ii) no brazing, and (iii) less energy-intensive manufacturing.

  - However, no commercial adhesives were found with all desirable properties, i.e., (i) low viscosity to penetrate high-density tube arrays, and (ii) can withstand high temperature and pressure (90+°C, 3.4+ MPa) which would be required for HVAC&R operation.
- The aluminum HX manufacturing process described herein is suitable for manufacturing, but additional improvements are needed to facilitate commercialization, including but not limited to:
  - Brazing of such HX requires additional study and further braze tests to optimize the brazing process. For example:
    - Increasing vacuum time to remove trapped oxygen.
    - Determine best ramp and soak time to allow the frame heat up at similar rate as the tube bundle.
    - Determine soak time to allow clad layer to wet all parts properly, including inside the tanks and all frame parts.

Component & System-Level Experimental Testing

- Further testing should be conducted on non-round tube HX prototypes, especially under dehumidifying conditions to further quantify fundamental heat & mass transfer principles.
  - This could be quantified by developing experimental correlations of Lewis number.
- Refrigerant maldistribution and condensate bridging were found to be more severe than anticipated during the system-level testing.
  - The next generation of non-round tube HXs should be designed with these considerations in mind, e.g., optimized header shapes, variable tube spacing, etc.
- Conduct system-level testing with appropriately sized non-round tube HXs operating as both the condenser and evaporator to experimentally validate the performance improvement / charge reduction potential.
  - Condenser
    - The new condenser prototype brazing was unsuccessful, and project end-time constraints prevented another condenser prototype from being manufactured.
    - The condenser was designed as a single-flow-pass, where the exit of all tubes and the exit header act as a receiver. A multi-pass condenser with a subcooling pass could further reduce HX size & charge.
  - Evaporator:
    - The evaporator was undersized, resulting in degraded system performance.
    - Additionally, the large evaporator headers were overdesigned to ensure pressure holding, and smaller headers provide an opportunity for further charge reduction.

Products

Journal Publications

In Print

1. Tancabel, J., et al. (2022). Multi-scale and multi-physics analysis, design optimization, and experimental validation of heat exchangers utilizing high performance, non-round tubes. *Applied Thermal Engineering, 216*, 118965. DOI: https://doi.org/10.1016/j.applthermaleng.2022.118965

In Preparation

1. Klein, E., et al. **Development of Shape Optimized Variable Geometry Bare Tube Heat Exchangers using Adjoint Methods.** Target Journals: *Applied Thermal Engineering, International Journal of Refrigeration, International Journal of Heat & Mass Transfer*.
2. Klein, E., et al. **Experimental Analysis of Finless Shape-and-Topology Optimized Heat Exchangers for Air Conditioning Applications.** Target Journals: *Applied Thermal Engineering, International Journal of Refrigeration, International Journal of Heat & Mass Transfer*.
3. Tancabel, J., et al. CFD-Based Dehumidification Performance Modeling of Shape-Optimized, Non-Round Tube Bundles in Air-to-Refrigerant Heat Exchangers. Target Journals: *Applied Thermal Engineering, International Journal of Refrigeration, International Journal of Heat & Mass Transfer*.
4. Tancabel, J., et al. **Design Optimization of A-Type Heat Exchangers based on High Performance, Non-Round Tubes**. Target Journals: *Applied Thermal Engineering, International Journal of Refrigeration, International Journal of Heat & Mass Transfer*.
5. Tancabel, J., et al. Aeroacoustics Noise Characterization of Shape-Optimized Non-Round Tube Bundles in Cross-Flow Configuration. Target Journal: *ASME Journal of Vibrations & Acoustics*.

Conference Publications

In Print

1. Klein, E., et al. (2018). **A Review of Recent Advances in Additively Manufactured Heat Exchangers**, *17th International Refrigeration & Air Conditioning Conference*, West Lafayette, Indiana, USA, July 9-12, 2018.
2. Tancabel, J. et al. (2018). **Review of Shape and Topology Optimization for Design of Air-to-Refrigerant Heat Exchangers**, *17th International Refrigeration & Air Conditioning Conference*, West Lafayette, Indiana, USA, July 9-12, 2018.
3. Tancabel, J., et al. (2019). **Multi-scale and multi-physics analysis of novel high performance, reduced charge evaporators with novel tube shapes**, *9th International Conference on Compressor and Refrigeration*, Xi'an, China, July 10-12, 2019.
4. Tancabel, J., et al. (2019). **Design Optimization of High Performance, Reduced Charge Condensers with Novel Tube Shapes**, *25th IIR International Congress of Refrigeration*, Montréal, Québec, Canada, August 24-30, 2019.

5. Klein, E., et al. (2019). **Experimental Study of a Novel Shape-Optimized Air-to-Refrigerant Heat Exchanger**. *2nd Pacific Rim Thermal Engineering Conference*, Maui, Hawaii, USA, December 13-17, 2019.
6. Tancabel, J., et al. (2020). **Optimization of R290 heat exchangers utilizing high performance, non-round tubes**. *14th IIR Gustav Lorentzen Conference on Natural Refrigerants (GL2020)*, Kyoto, Japan, December 6-9, 2020.
7. Klein, E., et al. (2021). **Experimental Study of a Novel Shape-Optimized Air-to-Refrigerant Heat Exchanger under Evaporator Conditions**, *18th International Refrigeration and Air Conditioning Conference*, West Lafayette, Indiana, USA, May 24-28, 2021.
8. Tancabel, J., et al. (2021). **Design Optimization of A-Type Heat Exchangers based on High Performance, Non-Round Tubes**, *18th International Refrigeration and Air Conditioning Conference*, West Lafayette, Indiana, USA, May 24-28, 2021.
9. Zhang, M., et al. (2021). **Stress and Fatigue Analysis of High-Performance Heat Exchangers**, *18th International Refrigeration and Air Conditioning Conference*, West Lafayette, Indiana, USA, May 24-28, 2021.
10. Tancabel, J., et al. (2021). **Design Optimization and Experimental Validation of Heat Exchangers Utilizing High Performance, Non-Round Tubes**. *15th International Conference on Heat Transfer, Fluid Mechanics and Thermodynamics (ATE-HEFAT)*, July 25-28, 2021. Paper awarded the “ATE-HEFAT 2021 Best Session Paper Award” for the Session: “Experimental Methods 3”.
11. Tancabel, J., et al. (2022). **Optimization of Novel Air-to-Refrigerant Heat Exchangers for Lower-GWP Refrigerants in Air-Conditioning Systems.** *14th REHVA HVAC World Congress* (CLIMA 2022). Rotterdam, The Netherlands. May 22-25, 2022.
12. Tancabel, J., et al. (2022). **Investigation of Shape Optimized Non-Round Tubes for CO_2 Gas Coolers.** *15th IIR-Gustav Lorentzen Conference on Natural Refrigerants*. Trondheim, Norway. June 13-15, 2022.
13. Tancabel, J., et al. (2022). **Aeroacoustics Noise Characterization of Shape-Optimized Non-Round Tube Bundles in Cross-Flow Configuration.** *18th International Refrigeration & Air-Conditioning Conference*. West Lafayette, Indiana, USA. July 10-14, 2022.
14. Zhang, M., et al. (2023). **Stress and Fatigue Analysis of Heat Exchangers with Different Tube Shapes**. *8th Thermal and Fluids Engineering Conference*. College Park, MD, USA. March, 26-29, 2023.
15. Tancabel, J., et al. (2023). CFD-Based Dehumidification Performance Modeling of Shape-Optimized, Non-Round Tube Bundles in Air-to-Refrigerant Heat Exchangers. *17th International Heat Transfer Conference*. Cape Town, South Africa, August 14-18, 2023.
16. Klein, E., et al. (2024). **Retrofit and Experimental Validation of a Packaged Air-Conditioning Unit with Heat Exchangers Utilizing Shape- and Topology-Optimized Tube Bundles**. *2024 ASHRAE Winter Conference*. Chicago, IL, USA. January 20-24, 2024.

Abstract-Only Presentations

1. Tancabel, J., & Aute, V. (2021). Multi-Scale & Multi-Physics Analysis, Approximation-Assisted Optimization, and Experimental Validation of Compact

Heat Exchangers utilizing High-Performance, Non-Round Tubes. *14th World Congress of Structural and Multidisciplinary Optimization*. June 13-18, 2021.

2. Tancabel, J., et al. (2023). Comparison of Approximation-Assisted and Adjoint Optimization Methods to Design Shape Optimized Air-to-Refrigerant Heat Exchangers. *15th World Congress of Structural and Multidisciplinary Optimization*. Cork, Ireland. June 5-9, 2023.

Inventions/Patents

Patent Pending

- Aute, V.C., et al. (2021). **Cross-flow heat exchanger systems and methods for fabrication thereof.** U.S. Patent Application No. 17/196,894. Publication Number: US20210285727A1.

Project Team and Roles

University of Maryland, College Park (UMCP)

Contribution

Multi-physics HX optimization framework development & HX design optimization

Experimental testing

Project management

Personnel

Reinhard Radermacher, PI; Minta Martin Professor of Engineering and Director, Center for Environmental Energy Engineering (CEEE)

Vikrant Aute, Co-PI; Research Professor and Co-Director, CEEE

Yunho Hwang, Co-PI; Research Professor and Co-Director, CEEE

Jan Muehlbauer; Senior Faculty Specialist, CEEE

James Tancabel; Postdoctoral Associate, CEEE

Ellery Klein; PhD graduate, CEEE

Cheng-Yi Lee; Graduate Research Assistant, CEEE

Heat Transfer Technologies, LLC (HTT)

Contribution

Novel manufacturing methods for non-round tubes

Novel tube-header integration strategies

HX prototyping

Personnel

Yoram Shabtay, Co-PI; President, HTT

John Black; V.P. Market Development, HTT

Naomi Carmeli-Shabtay; R&D Engineer, HTT

Oak Ridge National Laboratory (ORNL)

Contribution

Stress & fatigue analysis of tubes and full HX assemblies

Personnel

Mingkan Zhang; R&D Associate Staff Member

Zhenglai Shen; R&D Associate Staff Member

Industry Partners

Arconic, Brazeway, Burr Oak Tool, Daikin, Danfoss, Goodman Manufacturing / Daikin Comfort, Guentner, Johnson Controls, Inc., Modine, Wieland

References

[1] J. Tancabel, V. Aute, and R. Radermacher, "Review of shape and topology optimization for design of air-to-refrigerant heat exchangers," in *17th International Refrigeration & Air Conditioning Conference*, West Lafayette, Indiana, USA, 2018.

[2] E. Klein, J. Ling, V. Aute, and R. Radermacher, "A Review of Recent Advances in Additively Manufactured Heat Exchangers," in *17th International Refrigeration and Air Conditioning Conference at Purdue*, 2018.

[3] J. Tancabel *et al.*, "Multi-scale and multi-physics analysis, design optimization, and experimental validation of heat exchangers utilizing high performance, non-round tubes," *Appl Therm Eng*, vol. 216, p. 118965, Nov. 2022, doi: 10.1016/j.applthermaleng.2022.118965.

[4] J. Tancabel, "AN INTEGRATED, MULTI-PHYSICS ANALYSIS AND DESIGN OPTIMIZATION FRAMEWORK FOR AIR-TO-REFRIGERANT HEAT EXCHANGERS WITH SHAPE OPTIMIZED TUBES," PhD, University of Maryland, College Park, College Park, MD, USA, 2022.

[5] E. Klein, "DEVELOPMENT OF VARIABLE TUBE GEOMETRY HEAT EXCHANGERS USING ADJOINT METHOD WITH PERFORMANCE EVALUATION OF AN ADDITIVELY MANUFACTURED PROTOTYPE," University of Maryland, College Park, College Park, MD USA, 2023.

[6] United States Energy Information Administration, "Annual Energy Outlook 2022 with Projections to 2050," 2022.

[7] United States Department of Energy Office of Energy Efficiency and Renewable Energy, "Energy Conservation Standards for Residential Central Air Conditioners and Heat Pumps," 2017.

[8] United Nations Environment Ozone Secretariat, "Briefing Note on Ratification of the Kigali Amendment," 2017.

[9] W. M. Kays and A. L. London, *Compact Heat Exchangers*. New York: McGraw-Hill, 1984.

[10] S. Paitoonsurikarn, N. Kasagi, and Y. Suzuki, "Optimal design of micro bare-tube heat exchanger," *Proceedings of Symposium on Engineering in the 21st century (SEE 2000)*, no. 3, 2000, Accessed: Oct. 06, 2022. [Online]. Available: https://citeseerx.ist.psu.edu/viewdoc/download?doi=10.1.1.17.1531&rep=rep1&type=pdf

[11] N. Saji, S. Nagai, K. Tsuchiya, H. Asakura, and M. Obata, "Development of a compact laminar flow heat exchanger with stainless steel micro-tubes," *Physica C Supercond*, vol. 354, no. 1–4, pp. 148–151, May 2001, doi: 10.1016/S0921-4534(01)00064-8.

[12] N. Kasagi, Y. Suzuki, N. Shikazono, and T. Oku, "Optimal design and assessment of high performance micro bare-tube heat exchangers," in *4th Int. Conf. on Compact Heat Exchangers and Enhancement Technologies for the Process Industries*, 2003, pp. 241–246.

[13] D. Bacellar, J. Ling, V. Aute, and R. Radermacher, "Multi-scale, multi-physics design of micro and mini bare tube heat exchangers using multi-objective approximation assisted optimization," in *15th International Heat Transfer Conference*, Tokyo, Japan, 2014.

[14] D. Bacellar, V. Aute, Z. Huang, and R. Radermacher, “Novel airside heat transfer surface designs using an integrated multi-scale analysis with topology and shape optimization,” in *16th International Refrigeration and Air Conditioning Conference* , West Lafayette, Indiana, USA, 2016.

[15] H.-T. Chen, Y.-S. Lin, P.-C. Chen, and J.-R. Chang, “Numerical and experimental study of natural convection heat transfer characteristics for vertical plate fin and tube heat exchangers with various tube diameters,” *Int J Heat Mass Transf*, vol. 100, pp. 320–331, Sep. 2016, doi: 10.1016/j.ijheatmasstransfer.2016.04.039.

[16] D. Bacellar, V. Aute, Z. Huang, and R. Radermacher, “Design optimization and validation of high-performance heat exchangers using approximation assisted optimization and additive manufacturing,” *Sci Technol Built Environ*, vol. 23, no. 6, pp. 896–911, Aug. 2017, doi: 10.1080/23744731.2017.1333877.

[17] Z. Huang, “Development of a compact heat exchanger with bifurcated bare tubes,” PhD Dissertation, University of Maryland College Park, 2017.

[18] Westphalen D., K. Roth, and J. Brodrick, “Heat Transfer Enhancement,” *ASHRAE J*, vol. 48, no. 4, pp. 68–70, 2006, Accessed: Jul. 19, 2022. [Online]. Available: https://www.proquest.com/docview/220462097?pq-origsite=gscholar&fromopenview=true#

[19] K. Deb, *Multi-objective optimization using evolutionary algorithms*. New York: John Wiley & Sons, 2001.

[20] T. W. Simpson, J. D. Peplinski, P. N. Koch, and J. K. Allen, “Metamodels for computer-based engineering design: survey and recommendations,” 2001.

[21] G. Stanescu, A. J. Fowler, and A. Bejan, “The optimal spacing of cylinders in free-stream cross-flow forced convection,” *Int J Heat Mass Transf*, vol. 39, no. 2, pp. 311–317, Jan. 1996, doi: 10.1016/0017-9310(95)00122-P.

[22] M. F. Wright, “Plate-fin-and-tube condenser performance and design for a refrigerant R-410A air-conditioner ,” Master’s Thesis, Georgia Institute of Technology, 2000.

[23] R. S. Matos, J. V. C. Vargas, T. A. Laursen, and F. E. M. Saboya, “Optimization study and heat transfer comparison of staggered circular and elliptic tubes in forced convection,” *Int J Heat Mass Transf*, vol. 44, no. 20, pp. 3953–3961, 2001.

[24] K. A. Aspelund, “Optimization of plate-fin-and-tube condenser performance and design for refrigerant R-410A air-conditioner,” Master’s Thesis, Georgia Institute of Technology, 2001.

[25] S. W. Stewart and S. V. Shelton, “Finned-tube condenser design optimization using thermoeconomic isolation,” *Appl Therm Eng*, vol. 30, no. 14–15, pp. 2096–2102, Oct. 2010, doi: 10.1016/j.applthermaleng.2010.05.018.

[26] R. S. Matos, J. V. C. Vargas, T. A. Laursen, and A. Bejan, “Optimally staggered finned circular and elliptic tubes in forced convection,” *Int J Heat Mass Transf*, vol. 47, no. 6–7, pp. 1347–1359, Mar. 2004, doi: 10.1016/j.ijheatmasstransfer.2003.08.015.

[27] R. S. Matos, T. A. Laursen, J. V. C. Vargas, and A. Bejan, “Three-dimensional optimization of staggered finned circular and elliptic tubes in forced convection,” *International Journal of Thermal Sciences*, vol. 43, no. 5, pp. 477–487, May 2004, doi: 10.1016/j.ijthermalsci.2003.10.003.

[28] R. Hilbert, G. Janiga, R. Baron, and D. Thévenin, “Multi-objective shape optimization of a heat exchanger using parallel genetic algorithms,” *Int J Heat Mass Transf*, vol. 49, no. 15–16, pp. 2567–2577, Jul. 2006, doi: 10.1016/j.ijheatmasstransfer.2005.12.015.

[29] O. A. Abdelaziz, “Development of Multi-Scale, Multi-Physics, Analysis Capability and its Application to Novel Heat Exchanger Design and Optimization,” PhD Dissertation, University of Maryland, College Park, 2009.

[30] O. Abdelaziz, V. Aute, S. Azarm, and R. Radermacher, “Approximation-Assisted Optimization for Novel Compact Heat Exchanger Designs,” *HVAC&R Res*, vol. 16, no. 5, pp. 707–728, Sep. 2010, doi: 10.1080/10789669.2010.10390929.

[31] K. Saleh, V. Aute, S. Azarm, and R. Radermacher, “Online Approximation Assisted Multiobjective Optimization with Space Filling, Variance and Pareto Measures with Space Filling, Variance and Pareto Measures,” in *13th AIAA/ISSMO Multidisciplinary Analysis Optimization Conference*, Reston, Virigina: American Institute of Aeronautics and Astronautics, Sep. 2010. doi: 10.2514/6.2010-9103.

[32] V. Aute, K. Saleh, O. Abdelaziz, S. Azarm, and R. Radermacher, “Cross-validation based single response adaptive design of experiments for Kriging metamodeling of deterministic computer simulations,” *Structural and Multidisciplinary Optimization*, vol. 48, no. 3, pp. 581–605, Sep. 2013, doi: 10.1007/s00158-013-0918-5.

[33] H. Hajabdollahi, P. Ahmadi, and I. Dincer, “Multi-Objective Optimization of Plain Fin-and-Tube Heat Exchanger Using Evolutionary Algorithm,” *J Thermophys Heat Trans*, vol. 25, no. 3, pp. 424–431, Jul. 2011, doi: 10.2514/1.49976.

[34] S. Qian, L. Huang, V. Aute, Y. Hwang, and R. Radermacher, “Applicability of entransy dissipation based thermal resistance for design optimization of two-phase heat exchangers,” *Appl Therm Eng*, vol. 55, no. 1–2, pp. 140–148, Jun. 2013, doi: 10.1016/j.applthermaleng.2013.03.013.

[35] L. Daróczy, G. Janiga, and D. Thévenin, “Systematic analysis of the heat exchanger arrangement problem using multi-objective genetic optimization,” *Energy*, vol. 65, 2014, doi: 10.1016/j.energy.2013.11.035.

[36] P. Ranut, G. Janiga, E. Nobile, and D. Thévenin, “Multi-objective shape optimization of a tube bundle in cross-flow,” *Int J Heat Mass Transf*, vol. 68, pp. 585–598, Jan. 2014, doi: 10.1016/j.ijheatmasstransfer.2013.09.062.

[37] V. Aute, O. Abdelaziz, D. Bacellar, and R. Radermacher, “Novel Heat Exchanger Design Using Computational Fluid Dynamics and Approximation Assisted Optimization,” in *ASHRAE 2015 Winter Conference*, Chicago, Illinois, USA, 2015.

[38] N. El Gharbi, A. Kheiri, M. El Ganaoui, and R. Blanchard, “Numerical optimization of heat exchangers with circular and non-circular shapes,” *Case Studies in Thermal Engineering*, vol. 6, pp. 194–203, Sep. 2015, doi: 10.1016/j.csite.2015.09.006.

[39] L. Huang, V. Aute, and R. Radermacher, “Airflow distribution and design optimization of variable geometry microchannel heat exchangers,” *Sci Technol Built Environ*, vol. 21, no. 5, pp. 693–702, Jul. 2015, doi: 10.1080/23744731.2015.1047699.

[40] D. Bacellar, V. Aute, and R. Radermacher, “Performance evaluation criteria & utility function for analysis of compact air-to-refrigerant heat exchangers,” in *16th International Refrigeration and Air Conditioning Conference*, West Lafayette, Indiana, USA, 2016.

[41] R. A. Felber, G. Nellis, and N. Rudolph, “Design and Modeling of 3D-Printed Air-Cooled Heat Exchangers,” in *16th International Refrigeration and Air Conditioning Conference*, West Lafayette, Indiana, USA, 2016.

[42] Z. Huang, Z. Li, Y. Hwang, and R. Radermacher, “Application of entransy dissipation based thermal resistance to design optimization of a novel finless evaporator,” *Sci China Technol Sci*, vol. 59, no. 10, pp. 1486–1493, Oct. 2016, doi: 10.1007/s11431-016-0312-3.

[43] M. A. Arie, A. H. Shooshtari, V. V. Rao, S. V. Dessiatoun, and M. M. Ohadi, “Air-Side Heat Transfer Enhancement Utilizing Design Optimization and an Additive Manufacturing Technique,” *J Heat Transfer*, vol. 139, no. 3, Mar. 2017, doi: 10.1115/1.4035068.

[44] M. A. Arie, A. H. Shooshtari, R. Tiwari, S. V. Dessiatoun, M. M. Ohadi, and J. M. Pearce, “Experimental characterization of heat transfer in an additively manufactured polymer heat exchanger,” *Appl Therm Eng*, vol. 113, pp. 575–584, Feb. 2017, doi: 10.1016/j.applthermaleng.2016.11.030.

[45] D. Bacellar, Z. Huang, J. Tancabel, V. Aute, and R. Radermacher, “Multi-scale analysis, shape optimization and experimental validation of novel air-to-refrigerant heat exchangers,” in *9th World Conference on Experimental Heat Transfer, Fluid Mechanics, and Thermodynamics*, Iguazu Falls, Brazil, 2017.

[46] M. Darvish Damavandi, M. Forouzanmehr, and H. Safikhani, “Modeling and Pareto based multi-objective optimization of wavy fin-and-elliptical tube heat exchangers using CFD and NSGA-II algorithm,” *Appl Therm Eng*, vol. 111, pp. 325–339, Jan. 2017, doi: 10.1016/j.applthermaleng.2016.09.120.

[47] J. H. K. Haertel and G. F. Nellis, “A fully developed flow thermofluid model for topology optimization of 3D-printed air-cooled heat exchangers,” *Appl Therm Eng*, vol. 119, pp. 10–24, Jun. 2017, doi: 10.1016/j.applthermaleng.2017.03.030.

[48] B. D. Raja, V. Patel, and R. L. Jhala, “Thermal design and optimization of fin-and-tube heat exchanger using heat transfer search algorithm,” *Thermal Science and Engineering Progress*, vol. 4, pp. 45–57, Dec. 2017, doi: 10.1016/j.tsep.2017.08.004.

[49] Y. Zhicheng, W. Lijun, Y. Zhaokuo, and L. Haowen, “Shape optimization of welded plate heat exchangers based on grey correlation theory,” *Appl Therm Eng*, vol. 123, pp. 761–769, Aug. 2017, doi: 10.1016/j.applthermaleng.2017.05.005.

[50] U. Han, H. Kang, H. Lim, J. Han, and H. Lee, “Development and design optimization of novel polymer heat exchanger using the multi-objective genetic algorithm,” *Int J Heat Mass Transf*, vol. 144, p. 118589, Dec. 2019, doi: 10.1016/j.ijheatmasstransfer.2019.118589.

[51] K. R. Saviers, R. Ranjan, and R. Mahmoudi, “Design and validation of topology optimized heat exchangers,” in *AIAA Scitech 2019 Forum*, Reston, Virginia: American Institute of Aeronautics and Astronautics, Jan. 2019. doi: 10.2514/6.2019-1465.

[52] H. Lim, U. Han, and H. Lee, “Design optimization of bare tube heat exchanger for the application to mobile air conditioning systems,” *Appl Therm Eng*, vol. 165, p. 114609, Jan. 2020, doi: 10.1016/j.applthermaleng.2019.114609.

[53] F. Feppon, G. Allaire, C. Dapogny, and P. Jolivet, “Body-fitted topology optimization of 2D and 3D fluid-to-fluid heat exchangers,” *Comput Methods Appl Mech Eng*, vol. 376, p. 113638, Apr. 2021, doi: 10.1016/j.cma.2020.113638.

[54] H. Kang, U. Han, H. Lim, H. Lee, and Y. Hwang, “Numerical investigation and design optimization of a novel polymer heat exchanger with ogive sinusoidal wavy tube,” *Int J Heat Mass Transf*, vol. 166, p. 120785, Feb. 2021, doi: 10.1016/j.ijheatmasstransfer.2020.120785.

[55] A. Liu, G. Wang, D. Wang, X. Peng, and H. Yuan, “Study on the thermal and hydraulic performance of fin-and-tube heat exchanger based on topology optimization,” *Appl Therm Eng*, vol. 197, p. 117380, Oct. 2021, doi: 10.1016/J.APPLTHERMALENG.2021.117380.

[56] M. J. H. Rawa, Y. A. Al-Turki, N. H. Abu-Hamdeh, and A. Alimoradi, “Multi-objective optimization of heat transfer through the various types of tube banks arrangements,” *Alexandria Engineering Journal*, vol. 60, no. 3, pp. 2905–2919, Jun. 2021, doi: 10.1016/j.aej.2021.01.017.

[57] Z. Xu, Y. Guo, H. Yang, H. Mao, Z. Yu, and H. Zhang, “Performance calculation and configuration optimization of annular radiator by heat transfer unit simulation and a multi-objective genetic algorithm,” *Proceedings of the Institution of Mechanical Engineers, Part E: Journal of Process Mechanical Engineering*, vol. 235, no. 5, pp. 1292–1303, Oct. 2021, doi: 10.1177/09544089211001792.

[58] J. C. S. Garcia *et al.*, “Multiobjective geometry optimization of microchannel heat exchanger using real-coded genetic algorithm,” *Appl Therm Eng*, vol. 202, p. 117821, Feb. 2022, doi: 10.1016/j.applthermaleng.2021.117821.

[59] C. Ranganayakulu and K. N. Seetharamu, *Compact Heat Exchangers - Analysis, Design and Optimization using FEM and CFD Approach*. Chichester, UK: John Wiley & Sons, Ltd, 2018. doi: 10.1002/9781119424369.

[60] L. Zhang, Z. Qian, J. Deng, and Y. Yin, “Fluid–structure interaction numerical simulation of thermal performance and mechanical property on plate-fins heat exchanger,” *Heat and Mass Transfer*, vol. 51, no. 9, pp. 1337–1353, Sep. 2015, doi: 10.1007/s00231-015-1507-5.

[61] S. Wang, J. Xiao, J. Wang, G. Jian, J. Wen, and Z. Zhang, “Configuration optimization of shell-and-tube heat exchangers with helical baffles using multi-objective genetic algorithm based on fluid-structure interaction,” *International Communications in Heat and Mass Transfer*, vol. 85, pp. 62–69, Jul. 2017, doi: 10.1016/j.icheatmasstransfer.2017.04.016.

[62] S. Wang, G. Jian, J. Xiao, J. Wen, Z. Zhang, and J. Tu, “Fluid-thermal-structural analysis and structural optimization of spiral-wound heat exchanger,” *International Communications in Heat and Mass Transfer*, vol. 95, pp. 42–52, Jul. 2018, doi: 10.1016/j.icheatmasstransfer.2018.03.027.

[63] K. Li, J. Wen, S. Wang, and Y. Li, “Multi-parameter optimization of serrated fins in plate-fin heat exchanger based on fluid-structure interaction,” *Appl Therm Eng*, vol. 176, p. 115357, Jul. 2020, doi: 10.1016/j.applthermaleng.2020.115357.

[64] A. Harhara and M. M. Faruque Hasan, “Heat exchanger network synthesis with process safety compliance under tube rupture scenarios,” *Comput Chem Eng*, vol. 162, p. 107817, Jun. 2022, doi: 10.1016/j.compchemeng.2022.107817.

[65] F. F. Kraft, “Method for Predicting and Optimizing the Strength of Extruded Multi-Void Aluminum Heat Exchanger Tube,” May 2001. doi: 10.4271/2001-01-1737.

[66] G. Vamadevan, “PROCESS-STRUCTURE-PROPERTY RELATIONSHIP OF MICRO-CHANNEL TUBE FOR CO 2 CLIMATE CONTROL SYSTEMS A thesis presented to the faculty of the,” 2004.

[67] H. S. Miller, “INSTABILITY AND FAILURE IN ALUMINUM MULTI-CHANNEL TUBING,” 2006.

[68] M. Huang, “OPTIMIZING THE STRENGTH OF A CONDENSER TUBE,” in *ASME Pressure Vessels and Piping Division Conference*, 2008. Accessed: Oct. 09, 2022. [Online]. Available: https://proceedings.asmedigitalcollection.asme.org

[69] F. F. Kraft and T. L. Jamison, “Mechanical Behavior of Internally Pressurized Copper Tube for New HVACR Applications,” *J Press Vessel Technol*, vol. 134, no. 6, Dec. 2012, doi: 10.1115/1.4007035.

[70] L. Qi, “Mechanical Behavior of Copper Multi-Channel Tube for HVACR Systems,” 2013.

[71] X. H. Fan, D. Tang, W. L. Fang, D. Y. Li, and Y. H. Peng, “Microstructure development and texture evolution of aluminum multi-port extrusion tube during the porthole die extrusion,” *Mater Charact*, vol. 118, pp. 468–480, Aug. 2016, doi: 10.1016/J.MATCHAR.2016.06.025.

[72] D. Tang, X. Fan, W. Fang, D. Li, Y. Peng, and H. Wang, “Microstructure and mechanical properties development of micro channel tubes in extrusion, rolling and brazing,” *Mater Charact*, vol. 142, pp. 449–457, Aug. 2018, doi: 10.1016/J.MATCHAR.2018.06.010.

[73] C. Qian, Z. Wu, S. Wen, S. Gao, and G. Qin, “Study of the Mechanical Properties of Highly Efficient Heat Exchange Tubes,” *Materials*, 2020, doi: 10.3390/ma13020382.

[74] Z. Wu, C. Qian, G. Liu, Z. Liu, P. Sheng, and A. Di Schino, “Mechanical Properties and Heat Transfer Performance of Conically Corrugated Tube,” *Materials*, 2021, doi: 10.3390/ma14174902.

[75] G. L. Morini, “Single-phase convective heat transfer in microchannels: a review of experimental results,” *International Journal of Thermal Sciences*, vol. 43, no. 7, pp. 631–651, Jul. 2004, doi: 10.1016/j.ijthermalsci.2004.01.003.

[76] G. P. Celata, *Heat transfer and fluid flow in microchannels*. Begell House, 2004.

[77] M. E. Steinke and S. G. Kandlikar, “Single-phase liquid friction factors in microchannels,” *International Journal of Thermal Sciences*, vol. 45, no. 11, pp. 1073–1083, Nov. 2006, doi: 10.1016/j.ijthermalsci.2006.01.016.

[78] P. Rosa, T. G. Karayiannis, and M. W. Collins, “Single-phase heat transfer in microchannels: The importance of scaling effects,” *Appl Therm Eng*, vol. 29, no. 17–18, pp. 3447–3468, Dec. 2009, doi: 10.1016/j.applthermaleng.2009.05.015.

[79] M. Asadi, G. Xie, and B. Sunden, “A review of heat transfer and pressure drop characteristics of single and two-phase microchannels,” *Int J Heat Mass Transf*, vol. 79, pp. 34–53, Dec. 2014, doi: 10.1016/j.ijheatmasstransfer.2014.07.090.

[80] M. E. Schaffer, *A practical guide to noise and vibration control for HVAC systems*, 2nd ed. Atlanta, GA, USA: American Society of Heating, Refrigerating, and Air-Conditioning Engineers, 2011.

[81] ASHRAE, *2019 ASHRAE Handbook: HVAC Applications*. American Society of Heating, Refrigerating, and Air-Conditioning Engineers, 2019.

[82] ASHRAE, *2021 ASHRAE Handbook: Fundamentals*. American Society of Heating, Refrigerating, and Air-Conditioning Engineers, 2021.

[83] C. M. Ashley, “Air-Conditioning Noise Control,” *Noise Control*, vol. 1, no. 2, pp. 37–62, Mar. 1955, doi: 10.1121/1.2369133.

[84] E. E. Mikeska, “Air-Conditioning Equipment Noise Levels in Homes,” *Noise Control*, vol. 3, no. 3, pp. 11–54, May 1957, doi: 10.1121/1.2369259.

[85] J. S. Bradley, “Disturbance caused by residential air conditioner noise,” *J Acoust Soc Am*, vol. 93, no. 4, pp. 1978–1986, Apr. 1993, doi: 10.1121/1.406858.

[86] AHRI, “AHRI Standard 270-2015: Standard for Sound Performance Rating of Outdoor Unitary Equipment,” 2015.

[87] AHRI, “Standard 370-2015: Standard for Sound Performance Rating of Large Air-Cooled Outdoor Refrigerating and Air-Conditioning Equipment,” 2015.

[88] Y. N. Chen, “Flow-Induced Vibration and Noise in Tube-Bank Heat Exchangers Due to von Karman Streets,” *Journal of Engineering for Industry*, vol. 90, no. 1, pp. 134–146, Feb. 1968, doi: 10.1115/1.3604587.

[89] Y. N. Chen and W. C. Young, “The Orbital Movement and the Damping of the Fluidelastic Vibration of Tube Banks Due to Vortex Formation: Part 3—Damping Capability of the Tube Bank Against Vortex-Excited Sonic Vibration in the Fluid Column,” *Journal of Engineering for Industry*, vol. 96, no. 3, pp. 1072–1075, Aug. 1974, doi: 10.1115/1.3438410.

[90] J. A. Fitzpatrick, “A Design Guide Proposal for Avoidance of Acoustic Resonances in In-Line Heat Exchangers,” *J Vib Acoust*, vol. 108, no. 3, pp. 296–300, Jul. 1986, doi: 10.1115/1.3269342.

[91] S. Ziada, A. Oengören, and E. T. Bühlmann, “On acoustical resonance in tube arrays part II: Damping criteria,” *J Fluids Struct*, vol. 3, no. 3, pp. 315–324, May 1989, doi: 10.1016/S0889-9746(89)90091-1.

[92] R. D. Blevins, *Flow-induced vibration*, 2nd ed. New York, New York, USA: Van Nostrand Reinhold, 1990.

[93] F. L. Eisinger, R. E. Sullivan, and J. T. Francis, “A Review of Acoustic Vibration Criteria Compared to In-Service Experience With Steam Generator In-Line Tube Banks,” *J Press Vessel Technol*, vol. 116, no. 1, pp. 17–23, Feb. 1994, doi: 10.1115/1.2929552.

[94] F. L. Eisinger, J. T. Francis, and R. E. Sullivan, “Prediction of Acoustic Vibration in Steam Generator and Heat Exchanger Tube Banks,” *J Press Vessel Technol*, vol. 118, no. 2, pp. 221–236, May 1996, doi: 10.1115/1.2842185.

[95] H. Gelbe and S. Ziada, “Vibration of tube bundles in heat exchangers,” in *VDI Heat Atlas*, 2nd ed., VDI-GVC, Ed., 2010, pp. 1553–1585.

[96] “Private communications.” 2019.

[97] M. Wong, I. Owen, and C. J. Sutcliffe, “Pressure Loss and Heat Transfer Through Heat Sinks Produced by Selective Laser Melting,” *Heat Transfer Engineering*, vol. 30, no. 13, pp. 1068–1076, Nov. 2009, doi: 10.1080/01457630902922228.

[98] M. Arie, A. Shooshtari, S. Dessiatoun, and M. Ohadi, “Performance Characterization of an Additively Manufactured Titanium (Ti64) Heat Exchanger for

an Air-water Cooling Application," in *ASME 2016 Heat Transfer Summer Conference*, 2016.

[99] Y. Huang, M. C. Leu, J. Mazumder, and A. Donmez, "Additive Manufacturing: Current State, Future Potential, Gaps and Needs, and Recommendations," *J Manuf Sci Eng*, vol. 137, no. 1, Feb. 2015, doi: 10.1115/1.4028725.

[100] S. Tsopanos, M. Wong, I. Owen, and C. J. Sutcliffe, " Manufacturing Novel Heat Transfer Devices By Selective Laser Melting," in *13th International Heat Transfer Conference*, 2006.

[101] Y. Rua, R. Muren, and S. Reckinger, "Limitations of Additive Manufacturing on Microfluidic Heat Exchanger Components," *J Manuf Sci Eng*, vol. 137, no. 3, Jun. 2015, doi: 10.1115/1.4030157.

[102] U. Scheithauer, E. Schwarzer, T. Moritz, and A. Michaelis, "Additive Manufacturing of Ceramic Heat Exchanger: Opportunities and Limits of the Lithography-Based Ceramic Manufacturing (LCM)," *J Mater Eng Perform*, vol. 27, no. 1, pp. 14–20, Jan. 2018, doi: 10.1007/s11665-017-2843-z.

[103] M. Wong, S. Tsopanos, C. J. Sutcliffe, and I. Owen, "Selective laser melting of heat transfer devices," *Rapid Prototyp J*, vol. 13, no. 5, pp. 291–297, Oct. 2007, doi: 10.1108/13552540710824797.

[104] M. Wong, I. Owen, C. J. Sutcliffe, and A. Puri, "Convective heat transfer and pressure losses across novel heat sinks fabricated by Selective Laser Melting," *Int J Heat Mass Transf*, vol. 52, no. 1–2, pp. 281–288, Jan. 2009, doi: 10.1016/j.ijheatmasstransfer.2008.06.002.

[105] C. Yan, L. Hao, A. Hussein, S. L. Bubb, P. Young, and D. Raymont, "Evaluation of light-weight AlSi10Mg periodic cellular lattice structures fabricated via direct metal laser sintering," *J Mater Process Technol*, vol. 214, no. 4, pp. 856–864, Apr. 2014, doi: 10.1016/j.jmatprotec.2013.12.004.

[106] L. Ventola *et al.*, "Rough surfaces with enhanced heat transfer for electronics cooling by direct metal laser sintering," *Int J Heat Mass Transf*, vol. 75, pp. 58–74, Aug. 2014, doi: 10.1016/j.ijheatmasstransfer.2014.03.037.

[107] J. Pakkanen *et al.*, "Study of Internal Channel Surface Roughnesses Manufactured by Selective Laser Melting in Aluminum and Titanium Alloys," *Metallurgical and Materials Transactions A*, vol. 47, no. 8, pp. 3837–3844, Aug. 2016, doi: 10.1007/s11661-016-3478-7.

[108] C. K. Stimpson, J. C. Snyder, K. A. Thole, and D. Mongillo, "Roughness Effects on Flow and Heat Transfer for Additively Manufactured Channels," *J Turbomach*, vol. 138, no. 5, May 2016, doi: 10.1115/1.4032167.

[109] K. L. Kirsch and K. A. Thole, "Heat Transfer and Pressure Loss Measurements in Additively Manufactured Wavy Microchannels," *J Turbomach*, vol. 139, no. 1, Jan. 2017, doi: 10.1115/1.4034342.

[110] J. C. Snyder, C. K. Stimpson, K. A. Thole, and D. Mongillo, "Build Direction Effects on Additively Manufactured Channels," *J Turbomach*, vol. 138, no. 5, May 2016, doi: 10.1115/1.4032168.

[111] C. K. Stimpson, J. C. Snyder, K. A. Thole, and D. Mongillo, "Scaling Roughness Effects on Pressure Loss and Heat Transfer of Additively Manufactured Channels," *J Turbomach*, vol. 139, no. 2, Feb. 2017, doi: 10.1115/1.4034555.

[112] J. Bernardin, K. Ferguson, D. Sattler, and S. Kim, “The Design, Analysis, and Fabrication of an Additively Manufactured Twisted Tube Heat Exchanger,” in *ASME 2016 Summer Heat Transfer Conference*, 2016.

[113] O. T. Ibrahim *et al.*, “An investigation of a multi-layered oscillating heat pipe additively manufactured from Ti-6Al-4V powder,” *Int J Heat Mass Transf*, vol. 108, pp. 1036–1047, May 2017, doi: 10.1016/j.ijheatmasstransfer.2016.12.063.

[114] K. Garde, “Design and Manufacture of an Oil Cooler By Additive Manufacturing,” University of Minnesota, 2017.

[115] W. D. Gerstler and D. Erno, “Introduction of an additively manufactured multi-furcating heat exchanger,” in *2017 16th IEEE Intersociety Conference on Thermal and Thermomechanical Phenomena in Electronic Systems (ITherm)*, IEEE, May 2017, pp. 624–633. doi: 10.1109/ITHERM.2017.7992545.

[116] P. S. Korinko, J. Bobbitt, H. McKee, F. List, and K. Carver, “Characterization of Additively Manufactured Heat Exchanger Tubing,” in *Volume 6A: Materials and Fabrication*, American Society of Mechanical Engineers, Jul. 2017. doi: 10.1115/PVP2017-65809.

[117] B. J. Hathaway, K. Garde, S. C. Mantell, and J. H. Davidson, “Design and characterization of an additive manufactured hydraulic oil cooler,” *Int J Heat Mass Transf*, vol. 117, pp. 188–200, Feb. 2018, doi: 10.1016/j.ijheatmasstransfer.2017.10.013.

[118] H. R. S. Jazi, J. Mostaghimi, S. Chandra, L. Pershin, and T. Coyle, “Spray-Formed, Metal-Foam Heat Exchangers for High Temperature Applications,” *J Therm Sci Eng Appl*, vol. 1, no. 3, Sep. 2009, doi: 10.1115/1.4001049.

[119] Y. Cormier, P. Dupuis, B. Jodoin, and A. Corbeil, “Pyramidal Fin Arrays Performance Using Streamwise Anisotropic Materials by Cold Spray Additive Manufacturing,” *Journal of Thermal Spray Technology*, vol. 25, no. 1–2, pp. 170–182, Jan. 2016, doi: 10.1007/s11666-015-0267-6.

[120] Y. Cormier, P. Dupuis, B. Jodoin, and A. Corbeil, “Net Shape Fins for Compact Heat Exchanger Produced by Cold Spray,” *Journal of Thermal Spray Technology*, vol. 22, no. 7, pp. 1210–1221, Oct. 2013, doi: 10.1007/s11666-013-9968-x.

[121] P. Dupuis, Y. Cormier, A. Farjam, B. Jodoin, and A. Corbeil, “Performance evaluation of near-net pyramidal shaped fin arrays manufactured by cold spray,” *Int J Heat Mass Transf*, vol. 69, pp. 34–43, Feb. 2014, doi: 10.1016/j.ijheatmasstransfer.2013.09.072.

[122] A. Farjam, Y. Cormier, P. Dupuis, B. Jodoin, and A. Corbeil, “Influence of Alumina Addition to Aluminum Fins for Compact Heat Exchangers Produced by Cold Spray Additive Manufacturing,” *Journal of Thermal Spray Technology*, vol. 24, no. 7, pp. 1256–1268, Oct. 2015, doi: 10.1007/s11666-015-0305-4.

[123] P. Dupuis, Y. Cormier, M. Fenech, A. Corbeil, and B. Jodoin, “Flow structure identification and analysis in fin arrays produced by cold spray additive manufacturing,” *Int J Heat Mass Transf*, vol. 93, pp. 301–313, Feb. 2016, doi: 10.1016/j.ijheatmasstransfer.2015.10.019.

[124] P. Dupuis, Y. Cormier, M. Fenech, and B. Jodoin, “Heat transfer and flow structure characterization for pin fins produced by cold spray additive manufacturing,” *Int J Heat Mass Transf*, vol. 98, pp. 650–661, Jul. 2016, doi: 10.1016/j.ijheatmasstransfer.2016.03.069.

[125] C. Harris, M. Despa, and K. Kelly, “Design and fabrication of a cross flow micro heat exchanger,” *Journal of Microelectromechanical Systems*, vol. 9, no. 4, pp. 502–508, Dec. 2000, doi: 10.1109/84.896772.

[126] D. C. Deisenroth, M. A. Arie, S. Dessiatoun, A. Shooshtari, M. Ohadi, and A. Bar-Cohen, “Review of Most Recent Progress on Development of Polymer Heat Exchangers for Thermal Management Applications,” in *Volume 3: Advanced Fabrication and Manufacturing; Emerging Technology Frontiers; Energy, Health and Water- Applications of Nano-, Micro- and Mini-Scale Devices; MEMS and NEMS; Technology Update Talks; Thermal Management Using Micro Channels, Jets, Sprays*, American Society of Mechanical Engineers, Jul. 2015. doi: 10.1115/IPACK2015-48637.

[127] J. Cevallos, “Thermal and Manufacturing Design of Polymer Composite Heat Exchangers,” University of Maryland, College Park, 2014.

[128] X. Liu, J. Yu, and G. Yan, “An experimental study on the air side heat transfer performance of the perforated fin-tube heat exchangers under the frosting conditions,” *Appl Therm Eng*, vol. 166, p. 114634, Feb. 2020, doi: 10.1016/j.applthermaleng.2019.114634.

[129] H. Shulman and N. Ross, “Additive Manufacturing for Cost Efficient Production of Compact Ceramic Heat Exchangers and Recuperators,” Pittsburgh, PA, and Morgantown, WV (United States), Oct. 2015. doi: 10.2172/1234436.

[130] E. Schwarzer, M. Götz, D. Markova, D. Stafford, U. Scheithauer, and T. Moritz, “Lithography-based ceramic manufacturing (LCM) – Viscosity and cleaning as two quality influencing steps in the process chain of printing green parts,” *J Eur Ceram Soc*, vol. 37, no. 16, pp. 5329–5338, Dec. 2017, doi: 10.1016/j.jeurceramsoc.2017.05.046.

[131] N. Hopkinson and P. Dicknes, “Analysis of rapid manufacturing—using layer manufacturing processes for production,” *Proc Inst Mech Eng C J Mech Eng Sci*, vol. 217, no. 1, pp. 31–39, Jan. 2003, doi: 10.1243/095440603762554596.

[132] E. Atzeni and A. Salmi, “Economics of additive manufacturing for end-usable metal parts,” *The International Journal of Advanced Manufacturing Technology*, vol. 62, no. 9–12, pp. 1147–1155, Oct. 2012, doi: 10.1007/s00170-011-3878-1.

[133] R. E. Laureijs, J. B. Roca, S. P. Narra, C. Montgomery, J. L. Beuth, and E. R. H. Fuchs, “Metal Additive Manufacturing: Cost Competitive Beyond Low Volumes,” *J Manuf Sci Eng*, vol. 139, no. 8, Aug. 2017, doi: 10.1115/1.4035420.

[134] D. S. Thomas and S. W. Gilbert, “Costs and Cost Effectiveness of Additive Manufacturing,” Gaithersburg, MD, Dec. 2014. doi: 10.6028/NIST.SP.1176.

[135] M. Fera, R. Macchiaroli, F. Fruggiero, and A. Lambiase, “A new perspective for production process analysis using additive manufacturing—complexity vs production volume,” *The International Journal of Advanced Manufacturing Technology*, vol. 95, no. 1–4, pp. 673–685, Mar. 2018, doi: 10.1007/s00170-017-1221-1.

[136] J. Tancabel, V. Aute, and J. Ling, “Aeroacoustics Noise Characterization of Shape-Optimized Non-Round Tube Bundles in Cross-Flow Configuration,” in *19th International Refrigeration and Air Conditioning Conference*, 2022.

[137] J. Tancabel, V. Aute, and D. Bacellar, “CFD-Based Dehumidification Performance Modeling of Shape-Optimized, Non-Round Tube Bundles in Air-to-Refrigerant Heat Exchangers,” in *17th International Heat Transfer Conference*, 2023.

[138] L. Piegl and W. Tiller, “The NURBS book,” *Springer*, 1996.

[139] N. Cressie, *Statistics for spatial data*. New York: John Wiley & Sons, 1993.

[140] Ansys Inc., “Ansys® GAMBIT, Release 2.4.6.” 2018.

[141] Ansys Inc., “Ansys® Academic Research Fluent, Release 19.3.” 2019.

[142] T.-H. Shih, J. Zhu, and J. L. Lumley, “A new Reynolds stress algebraic equation model,” *Comput Methods Appl Mech Eng*, vol. 125, no. 1–4, pp. 287–302, Sep. 1995, doi: 10.1016/0045-7825(95)00796-4.

[143] T. L. Bergman, F. P. Incropera, D. P. Dewitt, and A. S. Lavine, *Fundamentals of heat and mass transfer*, 7th ed. Hoboken, New Jersey, USA: John Wiley & Sons, 2011.

[144] P. J. Roache, “QUANTIFICATION OF UNCERTAINTY IN COMPUTATIONAL FLUID DYNAMICS,” *Annu Rev Fluid Mech*, vol. 29, no. 1, pp. 123–160, Jan. 1997, doi: 10.1146/annurev.fluid.29.1.123.

[145] ASME PTC Committee, “Standard for verification and validation in computational fluid dynamics and heat transfer (ASME V&V 20-2009),” *The American Society of Mechanical Engineers (ASME)*, 2009.

[146] W. L. Oberkampf and C. J. Roy, *Verification and Validation in Scientific Computing*. Cambridge University Press, 2010. doi: 10.1017/CBO9780511760396.

[147] C. J. Roy and W. L. Oberkampf, “A comprehensive framework for verification, validation, and uncertainty quantification in scientific computing,” *Comput Methods Appl Mech Eng*, vol. 200, no. 25–28, pp. 2131–2144, Jun. 2011, doi: 10.1016/j.cma.2011.03.016.

[148] M. Armstrong, *Basic Linear Geostatistics*. Berlin, Heidelberg: Springer Berlin Heidelberg, 1998. doi: 10.1007/978-3-642-58727-6.

[149] T. M. D. Bakker, *Design optimization with Kriging models*. Delft University Press, 2000.

[150] D. R. Jones, “A taxonomy of global optimization methods based on response surfaces,” *Journal of Global Optimization*, vol. 21, no. 4, 2001, doi: 10.1023/A:1012771025575.

[151] M. D. Mckay, R. J. Beckman, and W. J. Conover, “A Comparison of Three Methods for Selecting Values of Input Variables in the Analysis of Output From a Computer Code,” *Technometrics*, vol. 42, no. 1, pp. 55–61, Feb. 1979, doi: 10.1080/00401706.2000.10485979.

[152] H. Hamad, “A New Metric for Measuring Metamodels Quality-of-Fit for Deterministic Simulations,” in *Proceedings of the 2006 Winter Simulation Conference*, IEEE, Dec. 2006, pp. 882–888. doi: 10.1109/WSC.2006.323171.

[153] Ansys Inc., “Ansys® Fluent Theory Guide, Release 19,” 2019.

[154] I. Proudman, “The generation of noise by isotropic turbulence,” *Proc R Soc Lond A Math Phys Sci*, vol. 214, no. 1116, pp. 119–132, Aug. 1952, doi: 10.1098/rspa.1952.0154.

[155] G. M. Lilley, “The radiated noise from isotropic turbulence revisited,” Hampton, VA, USA, 1993.

[156] R. G. Budynas, *Advanced strength and applied stress analysis*, 2nd ed. New York: McGraw-Hill, 1999.

[157] R. G. Budynas and A. M. Sadegh, *Roark's formulas for stress and strain*, 9th ed., no. C. New York: McGraw-Hill, 2020.

[158] Ansys Inc., "Ansys® Academic Research Fluent, Release 21.2." 2021.

[159] "Matlab." The MathWorks Inc, Natick, Massachusetts, USA, 2021.

[160] F. K. Dittus and L. M. K. Boelter, "Heat transfer in automobile radiators of the tubular type," *University of California Publications in Engineering*, vol. 2, no. 13, pp. 443–461, 1930.

[161] E. N. Sieder and G. E. Tate, "Heat Transfer and Pressure Drop of Liquids in Tubes," *Ind Eng Chem*, vol. 28, no. 12, pp. 1429–1435, Dec. 1936, doi: 10.1021/ie50324a027.

[162] H. Jiang, V. Aute, and R. Radermacher, "CoilDesigner: a general-purpose simulation and design tool for air-to-refrigerant heat exchangers," *International Journal of Refrigeration*, vol. 29, no. 4, pp. 601–610, Jun. 2006, doi: 10.1016/j.ijrefrig.2005.09.019.

[163] D. M. Admirral and C. W. Bullard, "Experimental Validation of Heat Exchanger Models for Refrigerator/Freezers," *ASHRAE Trans*, vol. 101, no. 1, pp. 34–43, 1995.

[164] A. M. JACOBI and R. K. SHAH, "Air-Side Flow and Heat Transfer in Compact Heat Exchangers: A Discussion of Enhancement Mechanisms," *Heat Transfer Engineering*, vol. 19, no. 4, pp. 29–41, Jan. 1998, doi: 10.1080/01457639808939934.

[165] F. C. McQuiston, J. D. Parker, and J. D. Spitler, *Heating, ventilation, and air conditioning: analysis and design*, 6th ed. John Wiley & Sons Inc., 1982.

[166] S. A. IDEM and V. W. GOLDSCHMIDT, "Sensible and Latent Heat Transfer to a Baffled Finned-Tube Heat Exchanger," *Heat Transfer Engineering*, vol. 14, no. 3, pp. 26–35, Jan. 1993, doi: 10.1080/01457639308939804.

[167] Y. Seshimo, K. Ogawa, M. Marumoto, and M. Fujii, "Heat and mass transfer performances on plate fin and tube heat exchangers with dehumidication," *JSME Transactions*, vol. 54, no. 466, pp. 716–721, 1998.

[168] C.-C. Wang and C.-T. Chang, "Heat and mass transfer for plate fin-and-tube heat exchangers, with and without hydrophilic coating," *Int J Heat Mass Transf*, vol. 41, no. 20, pp. 3109–3120, Oct. 1998, doi: 10.1016/S0017-9310(98)00060-X.

[169] Y. Xia and A. M. Jacobi, "Air-side data interpretation and performance analysis for heat exchangers with simultaneous heat and mass transfer: Wet and frosted surfaces," *Int J Heat Mass Transf*, vol. 48, no. 25–26, pp. 5089–5102, Dec. 2005, doi: 10.1016/j.ijheatmasstransfer.2005.08.008.

[170] W. Pirompugd, S. Wongwises, and C.-C. Wang, "A tube-by-tube reduction method for simultaneous heat and mass transfer characteristics for plain fin-and-tube heat exchangers in dehumidifying conditions," *Heat and Mass Transfer*, vol. 41, no. 8, pp. 756–765, Jun. 2005, doi: 10.1007/s00231-004-0581-x.

[171] W. Pirompugd, C.-C. Wang, and S. Wongwises, "A Fully Wet and Fully Dry Tiny Circular Fin Method for Heat and Mass Transfer Characteristics for Plain Fin-and-Tube Heat Exchangers Under Dehumidifying Conditions," *J Heat Transfer*, vol. 129, no. 9, pp. 1256–1267, Sep. 2007, doi: 10.1115/1.2739589.

[172] W. Pirompugd, C.-C. Wang, and S. Wongwises, “Finite circular fin method for heat and mass transfer characteristics for plain fin-and-tube heat exchangers under fully and partially wet surface conditions,” *Int J Heat Mass Transf*, vol. 50, no. 3–4, pp. 552–565, Feb. 2007, doi: 10.1016/j.ijheatmasstransfer.2006.07.017.

[173] C.-C. Wang, “On the heat and mass analogy of fin-and-tube heat exchanger,” *Int J Heat Mass Transf*, vol. 51, no. 7–8, pp. 2055–2059, Apr. 2008, doi: 10.1016/j.ijheatmasstransfer.2007.06.007.

[174] K. Hong, “Fundamental characteristics of dehumidifying heat exchangers with and without wetting coatings,” PhD, Pennsylvania State University, 1996.

[175] K. Hong and R. L. Webb, “Performance of Dehumidifying Heat Exchangers With and Without Wetting Coatings,” *J Heat Transfer*, vol. 121, no. 4, pp. 1018–1026, Nov. 1999, doi: 10.1115/1.2826052.

[176] W. Pirompugd, S. Wongwises, and C.-C. Wang, “Simultaneous heat and mass transfer characteristics for wavy fin-and-tube heat exchangers under dehumidifying conditions,” *Int J Heat Mass Transf*, vol. 49, no. 1–2, pp. 132–143, Jan. 2006, doi: 10.1016/j.ijheatmasstransfer.2005.05.043.

[177] W. Pirompugd, C.-C. Wang, and S. Wongwises, “Heat and Mass Transfer Characteristics for Finned Tube Heat Exchangers with Humidification,” *J Thermophys Heat Trans*, vol. 21, no. 2, pp. 361–371, Apr. 2007, doi: 10.2514/1.24170.

[178] T. Howongsakun, S. Theerakulpisut, P. Sujumnongtokul, and P. Palasan, “The Behavior of Lewis Number in Finned Tube Cooling Coils under Highly Moist Inlet Air Conditions,” *International Journal of Technology*, vol. 7, no. 7, p. 1253, Dec. 2016, doi: 10.14716/ijtech.v7i7.4654.

[179] C.-C. Wang, Y.-T. Lin, and C.-J. Lee, “Heat and momentum transfer for compact louvered fin-and-tube heat exchangers in wet conditions,” *Int J Heat Mass Transf*, vol. 43, no. 18, pp. 3443–3452, Sep. 2000, doi: 10.1016/S0017-9310(99)00375-0.

[180] Ansys Inc., “Ansys® Academic Research FENSAP-ICE, Release 21.2.” 2021.

[181] AHRI, “AHRI Standard 210/240 - 2017: Standard for performance rating of unitary air-conditioning & air-source heat pump equipment,” Arlington, Virginia, USA, 2017.

[182] W. Pirompugd, C.-C. Wang, and S. Wongwises, “Finite circular fin method for wavy fin-and-tube heat exchangers under fully and partially wet surface conditions,” *Int J Heat Mass Transf*, vol. 51, no. 15–16, pp. 4002–4017, Jul. 2008, doi: 10.1016/j.ijheatmasstransfer.2007.11.049.

[183] E. W. Lemmon, M. L. Huber, and M. O. McLinden, “NIST standard reference database 23: reference fluid thermodynamic and transport properties - REFPROP, Version 9.1.” National Institute of Standards and Technology, Standard Reference Data Program, 2013.

[184] V. Aute, R. Radermacher, Standardized Polynomials for Fast Evaluation of Refrigerant Thermophysical Properties. in *15th International Refrigeration & Air Conditioning Conference*, West Lafayette, Indiana, USA, 2014.

[185] V. Gnielinski, “On heat transfer in tubes,” *Int J Heat Mass Transf*, vol. 63, pp. 134–140, Aug. 2013, doi: 10.1016/j.ijheatmasstransfer.2013.04.015.

[186] S. W. Churchill, “Friction-factor equation spans all fluid-flow regimes,” *Chemical Engineering*, vol. 45, pp. 91–92, 1977

[187] M.M. Shah, A correlation for heat transfer during condensation in horizontal mini/micro channels, *International Journal of Refrigeration*. 64 (2016) 187–202. https://doi.org/10.1016/j.ijrefrig.2015.12.008.

[188] L. Sun, K. Mishima, Evaluation analysis of prediction methods for two-phase flow pressure drop in mini-channels, *International Journal of Multiphase Flow*. 35 (2009) 47–54. https://doi.org/10.1016/j.ijmultiphaseflow.2008.08.003.

[189] J. Tancabel, J. Ling, & V. Aute, "Optimization of novel air-to-refrigerant heat exchangers for lower-GWP refrigerants in air-conditioning systems", in *14th REHVA HVAC World Congress* (*CLIMA 2022*), Rotterdam, The Netherlands, 2022.

[190] J. Tancabel, V. Aute, & J. Ling, "Optimization of R290 heat exchangers utilizing high performance, non-round tubes", in *14th IIR-Gustav Lorentzen Conference on Natural Refrigerants*, Virtual Conference, 2020.

[191] J. Tancabel, V. Aute, and J. Ling, "Investigation of Shape Optimized Non-Round Tubes for CO2 Gas Coolers," in *15th IIR-Gustav Lorentzen Conference on Natural Refrigerants*, 2022.

[192] M. Zhang, P. Geoghegan, Y. Shabtay, J. Tancabel, J. Ling, & V. Aute, "Fatigue analysis of a high-performance heat exchanger", in *18th International Refrigeration & Air Conditioning Conference*, Virtual Conference, 2021.

[193] BIOVIA. 2019. "SOLIDWORKS."

[194] BIOVIA. 2020a. "Abaqus FEA."

[195] BIOVIA. 2020b. "Fe-Safe."

[196] A Bäumel, T. Seeger, & C. Boller. *Materials Data for Cyclic Loading: Supplement 1*. Elsevier. 1990.

[197] M. Zhang, Y. Shabtay, J. Tancabel, Z. Shen, D. Bacellar, & V. Aute. "STRESS AND FATIGUE ANALYSIS OF AIR-TO-REFRIGERANT HEAT EXCHANGERS WITH NON-ROUND TUBE SHAPES", in *8th Thermal and Fluids Engineering Conference (TFEC)*, College Park, MD, USA, 2023.

[198] ASHRAE, "ASHRAE Standard 33 - 2000: Method of testing forced circulation air cooling and air heating coil," Atlanta, Georgia, USA, 2000.

[199] ASHRAE, "ANSI/ASHRAE Standard 41.1 - 1987: Standard methods for temperature measurement," Atlanta, Georgia, USA, 1987.

[200] ASHRAE, "ANSI/ASHRAE Standard 41.2 - 1987: Standard methods for laboratory airflow measurement," Atlanta, Georgia, USA, 1987.

[201] ASHRAE, "ANSI/ASHRAE Standard 41.3 - 1987: Standard method for pressure measurement," Atlanta, Georgia, USA, 1987.

[202] ASHRAE, "ANSI/ASHRAE Standard 41.6 - 1987: Method for measurement of moist air properties," Atlanta, Georgia, USA, 1987

[203] ASME PTC Committee, "ASME Performance Test Codes 19.1 - 2013," The American Society of Mechanical Engineers (ASME), 2013.

[204] R.J. Moffat, "Describing the uncertainties in experimental results," *Exp Therm Fluid Sci*, vol. 1, no. 1, pp. 3–17, Jan. 1988, doi: 10.1016/0894-1777(88)90043-X.

[205] J. Winkler, V. Aute, R. Radermacher, Comprehensive investigation of numerical methods in simulating a steady-state vapor compression system, *International Journal of Refrigeration.* 31 (2008) 930–942. https://doi.org/10.1016/j.ijrefrig.2007.08.008